Inaugural dissertation

for

obtaining the doctoral degree

of the

Combined Faculty of Mathematics, Engineering and Natural Sciences

of the

Ruprecht - Karls - University

Heidelberg

Presented by

Katia Dittus (née Günther), M.Sc.

born in: Tübingen, Germany

Oral examination: 17.12.2025

Radiovirotherapy

for the treatment of refractory tumors

Referees: Prof. Dr. Stefan Wiemann

Prof Dr. Dr. Guy Ungerechts

Abstract

Cancer remains a major public health challenge and entities such as glioblastoma (GBM) and pancreatic ductal adenocarcinoma (PDAC) are particularly difficult to treat with the currently available therapeutics: Immune privileged locations, a challenging tumor microenvironment and often-occurring treatment resistances underline the need for novel therapeutic strategies. Radiotherapy is a cornerstone of cancer management and has benefited immensely from technological advances. Nevertheless, dose-limiting toxicities and relapse due to treatment resistance are frequent. A promising approach to increase treatment efficacy is the combination with immunotherapies. Oncolytic viruses, such as the vaccine strain of measles virus (MeV), are one such immunotherapeutic approach: MeV has a natural cancer tropism, lyses tumor cells and induces an anti-tumor immune response. However, MeV monotherapies have shown limited therapeutic efficacy in solid tumors. Preclinical data indicates that combining MeV with radiotherapy can produce synergistic effects and a favorable (innate) immune activation, although interferon (IFN)-mediated antiviral responses can also restrict MeV replication. I thus hypothesized that the addition of a second oncolytic vector, parvovirus, known to suppress the IFN response, could further enhance treatment efficacy. Through RNA sequencing, I characterized the combination of MeV and radiotherapy and observed distinct immune induction patterns in the combination. I then identified candidate cell lines from a panel of GBM and PDAC cell lines with the desired intact IFN signaling capacity, showing attenuation of MeV replication. In these models, I assessed cytotoxicity, synergy and the potential mechanisms of dual (PV + MeV) and triple (radiation + PV + MeV) therapy. Dual virotherapy produced additive cytotoxic effects alongside PV-mediated IFN suppression. While MeV replication was unaffected, its transgene expression was markedly reduced during co-infection. Triple radiovirotherapy demonstrated enhanced cytotoxicity and synergy in GBM cells at specific dose combinations, accompanied by modest IFN dampening and an increase in the immunogenic cell death (ICD) marker calreticulin. I additionally employed a heterotypic spheroid model, where the MeV-mediated IFN response was reduced when combined with certain PV doses, but cytotoxicity was not enhanced. On the contrary, triple combinations showed an antagonistic pattern. Finally, I generated and characterized murine cell lines expressing the MeV entry receptor for future in vivo evaluation.

Overall, I performed a comprehensive analysis of (triple) radiovirotherapy. The variable treatment efficacy reflects the complexity of analyzing advanced combination approaches *in vitro*. Nevertheless, synergistic combinations were identified, suggesting a potential therapeutic benefit for selected cancer patients suffering from refractory cancers such as PDAC and GBM.

Zusammenfassung

Krebs ist nach wie vor eine große Herausforderung für die öffentliche Gesundheit, insbesondere Erkrankungen wie Glioblastom (GBM) und duktales Adenokarzinom des Pankreas (PDAC) sind mit den derzeit verfügbaren Therapeutika schwer zu behandeln: Immunprivilegierte Lokalisationen, ein schwieriges Tumormikromilieu und häufig auftretende Therapieresistenzen belegen die Notwendigkeit neuer therapeutischer Strategien. Strahlentherapie ist ein Eckpfeiler der Krebsbehandlung und hat von technologischen Fortschritten enorm profitiert. Dennoch treten häufig dosislimitierende Nebenwirkungen und Rückfälle aufgrund von Therapieresistenzen auf. Ein vielversprechender Ansatz zur Steigerung der therapeutischen Wirksamkeit ist die Kombination mit Immuntherapien. Onkolytische Viren, wie beispielsweise der Impfstamm des Masernvirus (MeV), sind ein solcher immuntherapeutischer Ansatz: MeV hat einen natürlichen Tropismus für Krebszellen, lysiert sie und induziert eine Antitumor-Immunantwort. Allerdings haben MeV-Monotherapien bei soliden Tumoren nur eine begrenzte therapeutische Wirksamkeit gezeigt. Präklinische Daten deuten darauf hin, dass die Kombination von MeV mit Strahlentherapie synergistische Effekte und eine erhöhte (angeborene) Immunaktivierung hervorrufen kann, obwohl Interferon (IFN)-vermittelte antivirale Reaktionen auch die MeV-Replikation einschränken können. Ich stellte daher die Hypothese auf, dass die Zugabe eines zweiten onkolytischen Vektors, des Parvovirus, von dem bekannt ist, dass es die IFN-Reaktion unterdrückt, die Wirksamkeit der Behandlung verbessern kann. Mittels RNA Sequenzierung charakterisierte ich die Kombination aus MeV und Strahlentherapie und beobachtete dabei Unterschiede der Immuninduktionsmuster zwischen MeV und der Kombinationstherapie. Anschließend identifizierte ich aus einer Reihe von GBM- und PDAC-Zelllinien Kandidaten mit der gewünschten intakten IFN-Signalkapazität, in denen die MeV-Replikation attenuiert war. In diesen Modellen bewertete ich die Zytotoxizität, Synergie und potenziellen Mechanismen einer dualen (PV + MeV) oder dreifachen (Bestrahlung + PV + MeV) Therapie. Die duale Virotherapie führte neben der PV-vermittelten IFN-Suppression zu additiven zytotoxischen Effekten. Während die MeV-Replikation nicht beeinträchtigt war, war die Transgenexpression während der Koinfektion deutlich reduziert. Die dreifache Radiovirotherapie zeigte bei bestimmten Dosiskombinationen eine verstärkte Zytotoxizität und Synergie in GBM-Zellen, begleitet von einer moderaten IFN-Dämpfung und einem Anstieg des Markers für immunogenen Zelltod (ICD), Calreticulin. Zusätzlich verwendete ich ein heterotypisches Sphäroidmodell, bei dem die MeV-vermittelte IFN-Reaktion in Kombination mit bestimmten PV-Dosen reduziert war, die Zytotoxizität jedoch nicht verstärkt wurde. Im Gegensatz dazu zeigten Dreifachkombinationen ein antagonistisches Muster. Schließlich generierte und charakterisierte

ich murine Zelllinien der beiden Entitäten, die den MeV-Eintrittsrezeptor exprimieren, für zukünftige *in-vivo* Versuche.

Insgesamt habe ich eine umfassende Analyse der (dreifachen) Radio-Virotherapie durchgeführt. Die variable Wirksamkeit der Behandlung zeigt die Komplexität der Analyse fortgeschrittener Kombinationsansätze *in vitro*. Dennoch wurden synergistische Kombinationen identifiziert, die auf einen potenziellen therapeutischen Nutzen für ausgewählte Krebspatienten mit refraktären Krebsarten wie PDAC und GBM hindeuten.

Inhalt

1. Introduction

1.1. Cancer is a global public health crisis

In an aging society, cancer is becoming an increasing public health concern. Already among the leading causes of death worldwide, estimates suggest that cancer incidences will rise by 77 % until 2050.[1] While implementation of prevention and screening programs as well as advances in medical oncology have led to a reduction of cancer-related deaths in high-income countries, certain cancer entities are still expected to increase in both incidence and mortality.[2,3] These include malignancies with less well-defined etiologies, those requiring more invasive screening procedures, lacking reliable diagnostic biomarkers, and those resistant to current treatment modalities or without targeted therapeutic options.

Two of these difficult-to-treat cancer entities were the focus of my PhD project: Glioblastoma (GBM) and pancreatic ductal adenocarcinoma (PDAC).

1.1.1. Glioblastoma

Malignant tumors of the brain have an incidence of about seven newly diagnosed cases yearly among 100,000 persons worldwide.[1,4] 80 % of these are subsumed as “gliomas” and originate from neural stem or glial progenitor cells. Following the 2021 WHO classification, the heterogeneous group of gliomas is further subdivided according to histological features and molecular biomarkers. The largest subgroup is “adult-type diffuse gliomas” and comprises 90 % of cases. Within this subgroup, glioblastoma (GBM) is a grade IV occurrence and differentiated from a grade IV astrocytoma by its non-mutated (wildtype) isocitrate dehydrogenase (IDH) status.[5,6]

GBM has no clear etiology. Exposure to ionizing radiation is the only well-defined risk factor. Otherwise, only age clearly correlates with incidence with a median age of diagnosis at 65.[4,7] Patients can be asymptomatic or present with focal or generalized symptoms that include headaches, seizures, sensory loss or aphasia. GBM progresses rapidly and symptoms may thus develop accordingly within days to weeks. Due to the aggressive nature of GBM, high occurrence of resistance to therapy and the immune-privileged location, prognosis is poor with median survival of approximately 1.5 years and 5-year survival of only less than 5 %.[8,9] The latter has not significantly improved in the last decades.[8]

For glioblastoma, standard of care is a multimodal treatment approach: When possible, patients initially undergo surgery with maximal tumor resection. However, this is not an option for all patients since a patient’s general condition and/or the tumor localization/extend may not allow for surgery with an acceptable risk and/or the preservation of sufficient neurological function. Independent of surgery,

patients receive radiochemotherapy in accordance with the Stupp protocol: This most recent major advancement in GBM therapy was the addition of temozolomide (TMZ) to the treatment regimen after a landmark study by Stupp *et al* in 2005.[10] Now, patients receive daily TMZ concurrently to radiotherapy with 5 weekly doses of 2 Gy over 6 weeks, adding to a total of 60 Gy. After conclusion of radiotherapy, adjuvant chemotherapy continues for 6 months. In the aforementioned study, this resulted in an increase in 5-year survival from 1.9 % (radiotherapy alone) to 9.8 % (Stupp protocol).[11] TMZ is an alkylating chemotherapeutic agent and thus benefit is greatest for patients with methylation of *MGMT* promoter and resulting impairs of DNA repair. Accordingly, patients with unmethylated *MGMT* promotor and those with recurrent GBM after first line therapy have limited therapeutic options and are encouraged to participate in clinical trials.[12]

Although novel classes of drugs have transformed medical oncology over the past decade, none have yet been approved for glioblastoma or demonstrated a substantial clinical benefit: Antiangiogenic agents, such as bevacizumab, showed some benefit in progression-free survival, but this was accompanied by an increased toxicity and overall survival remained unchanged.[13,14] Clinical phase III trials of immunotherapies such as immune checkpoint inhibitors (ICI) or CAR T cell therapy have not shown improvement in overall survival. Notably, trials with oncolytic viruses (OVs) including Herpes Simplex Virus (HSV)[15], Parvovirus[16] and Poliovirus[17] have shown promising results in terms of safety as well as survival and/or immune activation.

All in all, the limited improvement in the clinical management of GBM shows the need to investigate novel treatment and combination regimens.

1.1.2. Pancreatic ductal adenocarcinoma

The most common cancer of the pancreas is pancreatic ductal adenocarcinoma (PDAC), constituting more than 90% of all cases.[18] 510,566 cases of pancreatic cancers were diagnosed worldwide in 2022 and there is a 0.89 % global lifetime risk of developing PDAC with a near-equal risk (0.85 %) of dying from the disease.[1,19] Incidence is rising and PDAC is estimated to be the most common cause of cancer-related death after lung cancer by 2030.[20]

Tumorigenesis is well characterized and usually somatic: Glandular epithelial cells of the pancreas acquire a mutation of the *KRAS* oncogene and subsequent mutations of tumor suppressor genes (TP53, CDKN2A and SMAD4A) accumulate, driving progression from precursor lesions such as pancreatic intraepithelial neoplasia to invasive carcinoma. Beyond its genetic hallmarks, PDAC develops a uniquely challenging tumor microenvironment (TME). The TME is characterized by pronounced fibrosis, with pancreatic stellate

cells (PSCs) transitioning from quiescence to activity, producing excessive extracellular matrix (ECM) and increasing tissue stiffness and interstitial pressure. These changes confer resistance to drug delivery and further complicate treatment outcomes. The PDAC TME is also notoriously immune-excluded, populated with immunosuppressive cells—most notably tumor-associated macrophages (TAMs) and regulatory T cells—that hinder anti-tumor immune responses.[21]

Risk factors for developing PDAC are well-described. Estimations indicate that up to 21-36 % of PDAC cases could be inherited, making family history of PDAC a strong risk factor.[22] Modifiable risk factors include smoking, obesity and alcohol consumption. Despite these known risk factors and well-defined tumorigenesis, early diagnosis remains rare: Current imaging modalities (including CT/MRI-scans of the abdomen or (endoscopic) ultrasound) and known tumor markers (CA19-9 and CEA[23]) are not suitable for screening of asymptomatic patients due to inaccuracy, lacking specificity and overall low incidence.[24] In addition, patients usually present with non-specific symptoms such as abdominal pain, jaundice, indigestion, or weight loss. Consequently, PDAC is often only diagnosed at advanced-stage disease, which leads to the dismal prognosis of only 4 months median survival overall and a 5-year survival rate of 13 %.[22] The latter group of long-term survivors comprises those that present with a resectable tumor and undergo surgery without residual disease (R0).[25]

Standard of care depends on the stage of disease and varies between countries. In patients with localized disease, surgery is indicated either after or before (neo-)adjuvant chemotherapy, depending on respectability. 57 % of patients present with metastasized disease. These are currently not recommended to undergo surgery nor be treated with curable intend. Then, palliative chemotherapy is usually advised. Chemotherapy regimens usually include (m)FOLFIRINOX (5-fluorouracil with leucovorin, irinotecan, and oxaliplatin) or gemcitabine-based therapies (gemcitabine/nab-paclitaxel or gemcitabine mono), based on the general condition of the patient.[22] Radiotherapy is not included as standard of care but may be added in addition to chemotherapy for both localized or metastatic disease. However, there is limited evidence of benefits: While a higher R0 resection rate was described when chemotherapy was followed by preoperative radiotherapy, a randomized phase 2 trial found chemotherapy alone to be more favorable for overall survial.[26,27]

Novel treatment strategies include targeted therapies. A promising target is *KRAS* as it is mutated in 88 % of PDAC cases.[22] Long deemed an undruggable target, recent advances have changed this perspective.[28] Now, several mutation-specific RAS inhibitors are evaluated preclinically and clinically, but none have been approved for application in PDAC thus far. Other immunotherapies, including cellular therapies and ICIs,

are evaluated in clinical trials, but PDAC is a particular difficult target entity due to the challenging TME described above. So far, only a subset of patients with deficiencies in the DNA repair machinery have benefitted from ICI application.[29,30] Certain OVs have shown promising data in clinical trials. Among them parvovirus[31], HSV-1[22] and reovirus[32]. Of note, the latter has shown substantial therapeutic benefit in a phase I/II trial in combination with chemotherapy and ICI, which led to FDA fast-track designation.[33]

In summary, PDAC remains a clinical challenge. The disease's aggressive biology, complex tumor microenvironment, and lack of early diagnostic tools contribute to its dismal prognosis, underscoring an urgent need for improved risk stratification and novel therapeutic interventions.

1.2. Conventional therapeutic strategies and their limitations

Surgery, chemotherapy and radiotherapy have been the cornerstones of cancer management for decades. Surgery has the longest-standing historical background in cancer therapy. It remains the treatment-of choice for localized, solid tumors, offering the highest likelihood of complete remission in early-stage disease.[34] However, for disseminated or advanced disease, surgical intervention is often not feasible. For these cases, the introduction of chemotherapy in the mid-20th century has transformed cancer treatment and enabled systemic therapy. Its use, whether as adjuvant (after complete resection to reduce recurrence), additive (after non-complete resection), neoadjuvant (to enable surgery or increase the likelihood of complete resection), or palliative therapy, may eradicate micrometastasis and enhance survival in many tumor types.[35] However, chemotherapy is toxic and not only affects tumor cells; its side effects may severely reduce the quality of life of cancer patients or lead to the necessity to discontinue the chemotherapy. In addition, resistance to chemotherapies occurs frequently and is the reason for 90 % of tumor relapses.[36,37]

Radiotherapy as the third pillar of conventional cancer therapies complements these therapeutic approaches.

1.2.1. Radiotherapy

The accidental discovery of "X-Strahlen" by Wilhelm Conrad Röntgen in the late 19th century[38] was a breakthrough for medicine as a therapeutic as well as diagnostic tool. Awarded with the very first Nobel Prize in physics in 1901, the impact of his discovery was clear to contemporary colleagues. Since then, the use of X-rays and other forms of ionizing radiation and has evolved and advanced technically. Today, it benefits 50 % of cancer patients that receive radiotherapy at least once during the course of their disease.[39,40]

Radiotherapy utilizes high-energy radiation beams (including photons or charged particles) to elicit DNA damage. The photon or charged particle carries enough energy to eject electrons from atoms in their path, leaving them ionized. This energy deposition is described as “linear energy transfer” (LET). When this occurs in biological tissues, the effects may be direct or indirect: Direct effects occur when the released electrons directly ionize DNA, inducing strand breaks. Indirect effects arise when the electron interacts with the abundantly present water molecules in the tissue, generating reactive oxygen species (ROS). ROS damage cellular components, including DNA, proteins, and lipids. The relative contribution of these mechanisms depends largely on the radiation beam: low-LET radiation such as X-rays and gamma rays primarily induces indirect effects, whereas high-LET modalities such as proton or carbon-ions produce a greater proportion of direct DNA damage due to their denser ionization tracks. Eventually, both effects result in accumulation of DNA double strand breaks, accumulation of cells in G2/M cell cycle phase with subsequent G1 arrest and senescence, apoptosis or immunogenic cell death (ICD).[41-44]

In addition to this well-described direct cytotoxic effect, a second mechanism of action has emerged more recently: Described as the “abscopal effect” radiotherapy can induce a systemic anti-tumor (immune)response. Preclinical and clinical data of various entities report on remission of metastasized tumors after application of localized radiotherapy.[45] One proposed mechanism is the IFN-mediated immune induction through the cytoplasmic DNA sensor cGAS and as such a secondary effect of the DNA damage.[46] In general, the mode of cell death associated with irradiation is considered immunogenic and can thus elicit a “in-situ vaccination” effect.[47] Currently, studies focus on optimal dosing and fractionation regimens to maximize the immune induction by radiotherapy.

Radiotherapy is not inherently cancer-specific. However, certain properties of a cancer cell render them more susceptible to the radiation-induced damage than the adjacent healthy tissue: Cancer cells divide faster, resulting in a higher ratio of cells in the G2/M phase, which is characterized by reduced DNA repair activity. Secondly, cancer cells often harbour defects in their DNA repair pathways or in proteins regulating cell cycle checkpoints, compromising their ability to maintain genomic integrity following irradiation.[48] Additionally, technological advances have further improved precision and therefore safety of radiotherapy delivery: Precise, computed tomography (CT)-guided treatment planning, adjusted to the individual patient and treatment response foreshadowed personalized therapeutic approaches and reduced side effects.[49] The introduction of intensity-modulated radiotherapy (IMRT), where the radiation beam is segmented and differentially modulated for maximal dose delivery to the tumor, has expanded the application of radiotherapy to tumors adjacent to radiosensitive organs. [50,51]

A diverse set of radiotherapeutic treatment modalities are in clinical practice. Broadly, these can be categorized into external beam radiotherapy (EBRT) and internally delivered radiation. Brachytherapy is an example of the latter, where a sealed radioactive source is positioned inside or in close proximity to a tumor. Clinically, it is most frequently applied in small gynecologic and prostate tumors.[52] EBRT remains the most widely used form of radiotherapy and is further subdivided in dependence on the radiation source. Most common and cost-effective is the use of photons (X-rays). In addition, the use of protons or heavy ions is available to an increasing number of patients. Their primary advantage over photon-based techniques is the superior dose distribution within a tissue. X-rays deliver their maximal dose in close proximity to their entry point into tissue and exponentially loose energy thereafter. Protons and heavy ions increase in dose release after entry up to a specified depth ("bragg peak") and subsequently suddenly drop in energy deposition. This property results in minimal exit dose and allows for precise tumor irradiation while sparing surrounding normal tissues. However, less than 1 % of radiotherapy patients receive particle radiotherapy since only limited centers worldwide offer the required technique.[53]

Even with technical advances and a variety of radiation types to choose from, limitations of radiotherapy remain. Certain cancer entities (such as PDAC) are characterized by a hypoxic TME. In these entities, the indirect effect of radiation through ROS production is less efficient. Additionally, tumors may upregulate DNA repair mechanisms to build radioresistance during the course of treatment. And, thirdly, although advanced technologies has improved safe radiotherapy delivery, its effect on healthy tissue and occurrence of secondary malignancies because of previous radiotherapy, remain major limitations.[40,54]

All conventional therapeutic approaches have major limitations. The untargeted approach of going for the fast-dividing cells causes severe side effects due to toxicities on physiologically fast-dividing cells and limitations when certain cancer (stem) cells are not rapidly dividing and causing treatment resistances instead. Other therapeutic modalities were desired, that can attack the cancer more elegantly

1.3. Immunotherapies

Development of cells with aberrant signaling and tumorigenic potential occurs constantly in the human body. Usually, immune cells can clear these, recognizing tumor-associated antigens (TAA) and prevent tumor formation. This concept was experimentally confirmed when lymphocyte-deficient mice were shown to be markedly more susceptible to chemically induced tumor formation.[55] In 2011, Hanahan and Weinberg declared "avoiding immune destruction" as an emerging hallmark of cancer, underscoring the pivotal role in tumor development.[56] This avoidance can occur via a variety of mechanism, including the release of immunosuppressive cytokines, regulation of immune checkpoints, downregulation of major

histocompatibility complex (MHC) molecules and recruitment of immunomodulatory cell populations. [57] Counteracting these evasion strategies is the goal of immunotherapeutic approaches.

Accordingly, the field of immunotherapies is diverse. Clinically, the most advanced strategy is the use of immune checkpoint inhibitors (ICI). This antibody-mediated inhibition of upregulated immune checkpoints to enhance T cell response against cancer was awarded the Nobel Prize in 2018[58] and has transformed clinical oncology. In certain cancer entities, long-term survival can be achieved, even in patients with recurrent disease, and ICIs have been incorporated into standard of care as first-line therapies.[59-61] To date, 10 ICIs are approved in by the Food and Drug Administration (FDA) and many more are assessed in clinical trials.[57]. Another promising approach is adoptive cell therapy (ACT). ACT aims to activate, enrich or modify patient-derived immune effector *ex vivo* and reinfuse them to enhance tumor cell killing. One ACT strategy is to engineer a patient's T cells with an artificial chimeric antigen receptor (CAR) to target TAAs and has been FDA approved for hematological malignancies, but remains of limited success in solid tumors.[57] Of note, while several immunotherapeutic approaches have been assessed clinically for PDAC and GBM, none have shown a therapeutic benefit over standard-of-care.[9,30]

One interesting immunotherapeutic approach is the use oncolytic viruses (OVs) to target tumor cells.

1.3.1. Virotherapy

The first observations of (viral) infections that induce cancer remissions date back to the late 19th centrury[62] long before the instrinsic connection of the immune system and cancer was unraveled and immunotherapeutics were envisioned. Viruses were not (well) understood, but case reports continued to describe remission of cancer (often hematologic variants) occurring concurrently with infections.[63] With increasing knowledge of viral biology, interest in virotherapy surged in the 1950s with multiple "clinical trials" evaluating the anti-tumor effect of viruses.[64,65] However, durable tumor responses were rare and frequently accompanied by severe adverse effects due to the uncontrolled pathogenicity of the viral agents. The field fundamentally changed in the 1990s, when advances in cell culture techniques and DNA engineering allowed the attenuation, production and rational modification of OVs. [63] Since then, an expanding array of viruses has been tested preclinically and clinically, covering the whole spectrum of virology.[66] A milestone in the field was the FDA- and European Medicines Agency (EMA) approval of the herpes simplex virus type 1 (HSV-1)-derived talimogene laherparepevec (T-VEC) for recurrent malignant melanoma in 2015.[67]

Virotherapy offers an intriguing dual mechanism of action (**Figure 1-1**, adapted from Dittus *et al*[68]**):** OVs selectively infect cancer cells, replicate and, as part of the viral life cycle, induce cell lysis. Initially this

"oncolytic" property was the only described mechanism. With increasing knowledge of the role the immune system plays in tumor clearance, a second mechanism became clear:[69] OV-mediated tumor cell lysis can alert the immune system through release of cytokines, pathogen- or danger-associated molecular patterns (PAMPs and DAMPs) and TAAs. This will in turn recruit immune cells formerly excluded from the tumor to the tumor microenvironment and can elicit an anti-tumor immune response. This may also be referred to as "*in situ* vaccination" when OVs act as the adjuvant to prime immune cells to recognize the tumor and induce immunological memory.[70]

For clinical application, the tumor-selectivity is a major determinant of safety. The mechanism by which this is conferred differs between OVs. Selectivity can be mediated at the entry level, when viral entry receptors are overexpressed on tumor cells (e.g. junctional adhesion molecule A's(JAM-A), overexpressed

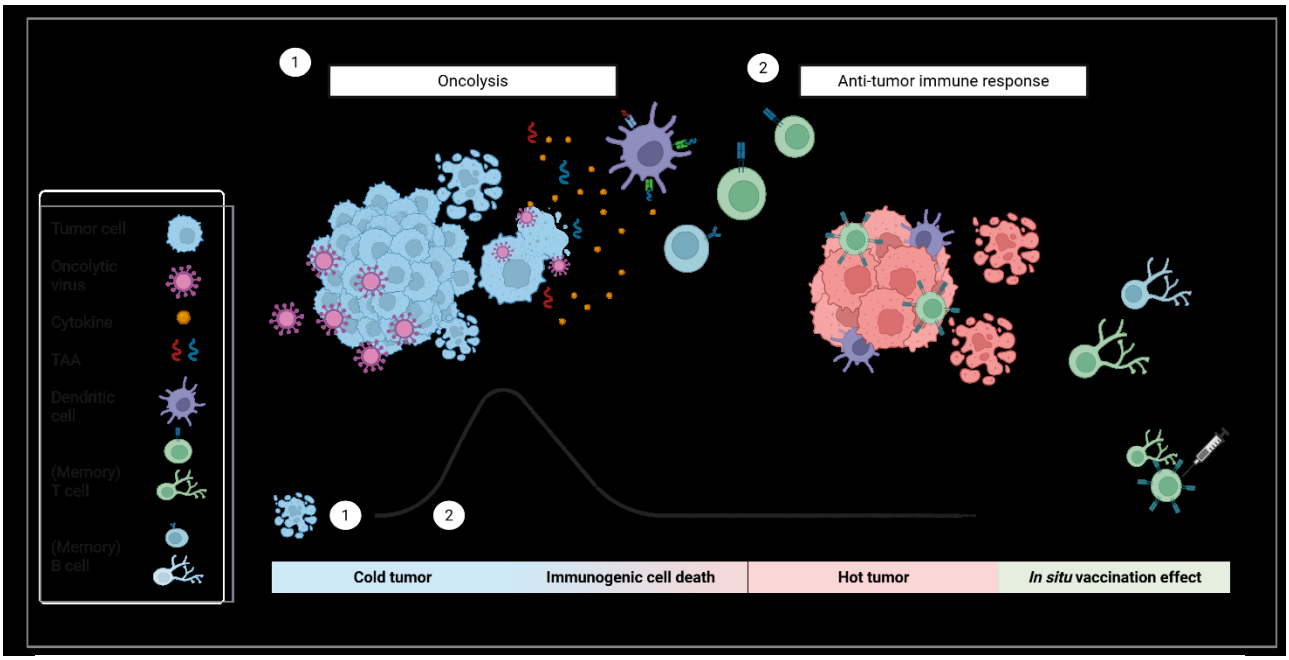

Figure 1-1: Dual mechanism of oncolytic virotherapy

The oncolytic viruses selectively infects tumor cells, inducing their lysis. In addiaion, the immunogenic nature of the induced cell death results in release of cytokines and tumor associated antigens (TAA), attracting immune cells to the previously "cold" tumor microenvironment. Then, an anti-tumor immune response is induced and the tumor can be cleared by the immune system. An in situ vaccination effect is induced, eliciting a immunological memory. Graph created in biorender, adapted from Dittus *et al.*[68]

and conferring poor prognosis for a variety of cancer types[71] is the entry receptor of reovirus[72]). Post-entry selectivity may occur through viral dependence on cell replication, thus targeting fast-dividing cells[73] or by exploiting deficits in antiviral signaling cascades that tumor cells often acquire.[74] Certain OVs possess these properties naturally (such as reovirus[75] and parvovirus[73]), others are engineered for enhanced tumor-selectivity (like HSV-1[76]).

Beyond conferring oncotropism, viruses can be engineered for different purposes. A common approach is to encode therapeutic transgene to enhance immune induction or overall efficacy.[70] Transgene may include cytokines[77], bispecific antibodies to attract immune cells[78], ICIs[79] or prodrug convertases[80]. The transgene capacity varies widely across viral backbones from a few hundred nucleotides (for small OVs such as parvovirus[81]) to 40 kilobases (vaccinica virus [82]). This underlines the versatility of OVs that can and should be selected depending on the entity and the envisioned therapeutic strategy.

1.3.1.1. Oncolytic Measles Virus

One promising candidate in the OV toolbox is the oncolytic measles virus (MeV). Just like other OVs, the potential of MeV as an anti-cancer agent was first observed when a natural measles infection coincided with a cancer case. The most famous case study is one of a young boy in Kampala, Uganda, who suffered from Burkitt's Lymphoma and experienced a complete tumor remission when he also had a systemic measles infection.[83] For virotherapeutic purposes, attenuated vaccine-derivatives of the wild-type measles virus are used.

Wild-type measles virus is a highly contagious strictly human pathogen that causes a severe systemic disease. A highly effective vaccine was introduced in the 1960s and has prevented an estimated 60 million deaths just in the 21st century. Nevertheless, more than 100,000 annual deaths worldwide are still caused by the virus.[84,85]

MeV is a member of the *Paramyxoviridae* family of the *Morbilivirus* genus. It has non-segmented single stranded (ss) RNA genome of negative polarity (**Figure 1-2B,** figure equally printed in [86]). The 15,894 nucleotides encode for six structural and two regulatory proteins. In addition, regulatory elements on the 3' leader (ld) and 5' trailer (tr) end of the genome play an important role in viral genome replication and transcription.[87]

The assembled virion (**Figure 1-2A**) has a size of 100-300 nm in diameter and is enveloped by the lipid membrane of the cell it budded from. Inside, the RNA genome is packed by nucleoproteins (N) binding six nucleotides each. Additionally, the large protein (L) and its accessory phosphoprotein (P) are bound to the packaged genome, forming the ribonucleoprotein complex (RNP). L, P and N together form the viral RNA-dependent RNA polymerase. The polymerase transcribes the genome from the 3' end. Stop signals are located at the 5' end of each open reading frame (ORF), where transcription halts and polyadenylation occurs. The stop signal is followed by three nucleotides forming an intergenic region. At each intergenic region, the polymerase has a certain chance of falling off, which leads to a transcription gradient from the 3' to 5' end of the viral genome. When enough N protein is expressed in the cell, it may bind nascent 3' RNA immediately, which leads the polymerase to skip all stop signals and transcribe through intergenic sequences giving rise to full-length antigenomes for replication.[88] A single virion can contain multiple RNPs, making it a polyploid virus.[89] When an RNP is fully assembled, it binds the matrix protein (M) and attaches to the membrane, which inhibits viral transcription and initiates viral budding.[90] Hemagglutinin (H) and fusion protein (F) are transmembrane gylcoproteins and exposed on the enveloped viral particle. They are responsible for attachment and entry into cells. To this end, H binds to its target receptor CD150 (signaling lymphocytic activation molecule (SLAM), expressed on macrophages, dendritic, B and T cells) or Nectin-4 (expressed on epithelial cells) and a transformational change of F enables entry. This fusion occurs between viral particles and host cells for viral entry and equally between infected host cells that express

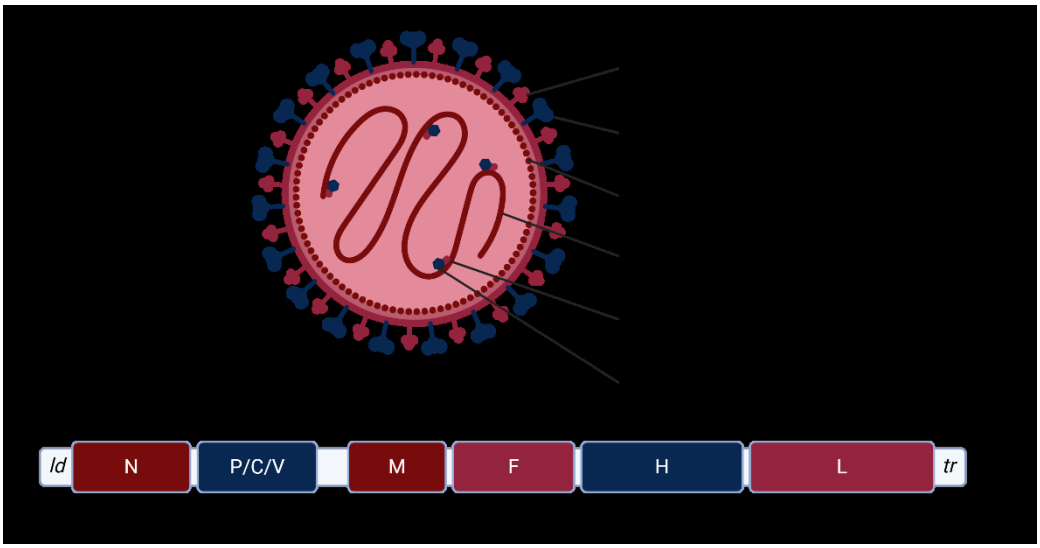

Figure 1-2: Graphical representation of measles virus particle and genome

(A) The assembled MeV particle with the six structural proteins: The fusion protein (F) and hemagglutinin (H) are exposed on the surface of the host- derived lipid membrane, that constitutes the viral envelope. The matrix protein (M) is attached on the inside. The ssRNA genome is packaged by the nucleoprotein N and the viral polymerase complex of the large protein (L) and poshoprotein (P) is associated, together forming the ribonuceleoprotein (RNP) complex. (B) The genomic structure of MeV with leader (ld) at the 3' and trailer (tr) at the 5' end. In addition to the 6 structural proteins, the open reading frame (ORF) of P also encodes for the C and V protein. Graph created in biorender.com and equally used in[86].

the viral proteins and their neighboring cells expressing CD150 or Nectin-4. This leads to the formation of large multinucleated cellular complexes, syncytia, which are a hallmark of MeV infection.[91] The two non-structural proteins, V and C, are involved in immune evasion and counteract the cellular IFN response.[92] MeV's life cycle is strictly cytoplasmic.[88]

The vaccine strains that are employed as oncolytic vectors have distinct differences to their wild-type counterpart. These are a result of the attenuation process of serial passaging on non-human cells. This makes it a feasible and safe vaccine as well as OV candidate.[93] Most notably, MeV vaccine strains have an additional entry receptor, CD46, which is expressed on all nucleated cells and found to be overexpressed across a multitude of cancer entities.[94,95] A second important difference between wild-type and vaccine strains are mutations in the C and V proteins that counteract antiviral signaling. These mutations render MeV highly IFN-sensitive and lead to attenuation in cells that have intact IFN signaling.[96]

MeV has been tested extensively in preclinical settings. A variety of cancer entities are permissive to MeV infection and MeV can elicit a strong cytotoxic effect. Various approaches of retargeting, arming and combining MeV have been undertaken *in vitro* and *in vivo.* Those strategies were recently reviewed in [94] and [97]. Equally, MeV is currently under clinical investigation for several entities. Very promising case reports in regard to therapeutic efficacy have been published[98,99] accompanied by an excellent safety profile[100]

1.3.1.2. Oncolytic Protoparvovirus

Protoparvoviruses are very different, yet promising OV candidates. First isolated from transplanted human tumors, they were briefly believed to be oncogenic.[101] This was quickly dismissed[102] and it was discovered that those viruses had a natural affinity for human cancer cells and, in fact, elicited an oncosuppressive effect.[73,103]

Protoparvovirus is a genus within the large *parvovirdiae* family, more specifically the *parvovirinae* subfamily. Two viruses of the *rodent protoparvovirus* have been studied most extensively in an oncolytic context: H-1 parvovirus (H-1PV) and minute viruses of mice (MVM). They are pathogenic, even lethal, for rodent embryos and neonates, but do not cause symptoms in adult animals or humans.[81] H-1PV's natural host is the rat, while MVM preferentially infects murine cells. Both have a strong oncotropism and infect human cancer cells.[104] The virus employed in all experiments involving human cancer cell lines in this thesis was H-1PV and will be referred to as "PV" in the following sections. When MVM was used for experiments in murine cell lines, it is referred as MVM.

PV has a single-stranded DNA genome of approximately 5.1 kilobases. The viral genome is organized in two transcription units for non-structural (NS) and structural (VP) viral proteins under the control of the P4 or P38 promoter, respectively. The NS unit encodes for NS1 and NS2, the VP unit encodes for VP1 and VP2 as well as the small alternatively translated (SAT) protein. The coding sequence is flanked by terminal palindromes that have a role in genome replication.[105] (**Figure 1-3**, adapted from [106] and viralzone.expasy.org/199).[81]

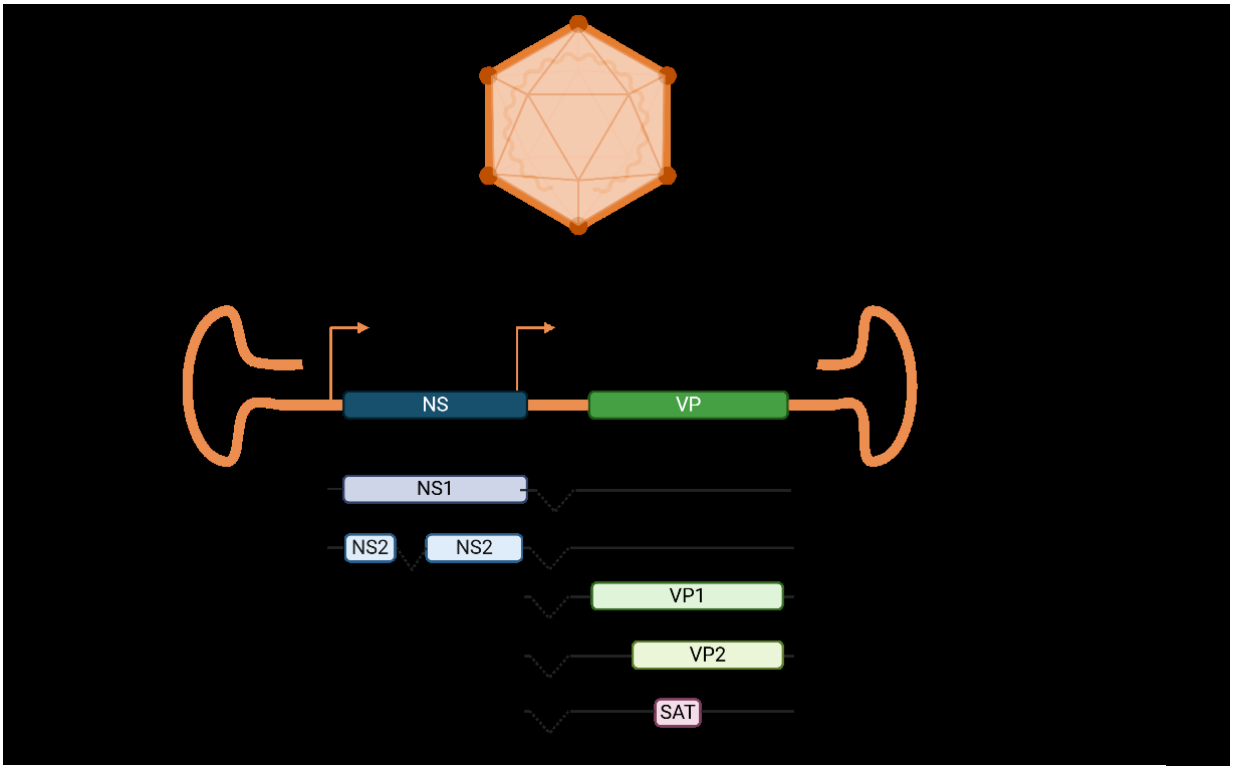

Figure 1-3: Graphical representation of parvovirus (PV) particle and genome

(A) The assembled PV particle is non-enveloped and icosadhedral and contains the ssDNA genome (B) The PV genome structure is flanked by palindromic sequences. It has two transcriptional units for non-strucutrual (NS) and structural proteins (VP) under the control of distinct promoters, p4 and p38. The NS ORF encodes for NS1 and NS2 protein, the VP ORF encodes for VP1, VP2 and SAT. Figure was generated in biorender, adapted from [106] and viralzone.expasy.org/199, last visited on 19th October 2025; SAT – small alternatively translated

Specific entry receptors for H-1PV and MVM have not been characterized, but the binding of the virus particles to the cell surface is dependent on sialic acid.[107] After entering the cell, viral particles are transported into the cell nucleus. Replication is dependent on the expression of S-phase proteins. Until the host cell enters S-phase, the virions are silent and do not integrate into the host DNA. Then, exploiting the cellular replication and transcription machinery, viral genomes are replicated via doublestranded DNA (dsDNA) intermediates and transcription of the P4-promoter controlled genes is initiated. NS1 is expressed and interacts with several cellular factors to transactivate the P38 promoter and induce transcription of VP1 and VP2. Once proteins are translated, they are shuttled back into the nucleus, where progeny virus

particles are assembled and actively released into the cytoplasm. The SAT protein has only recently been discovered and is not yet well-characterized. The interaction of the viral NS1 protein with the cellular replication machinery is complex and not yet fully elucidated. Ultimately, it leads to cell cycle arrest and the induction of a DNA damage response, which results in cell lysis.[81]

The oncotropism of PV is mainly driven by the S phase dependency on the post entry level. A second mechanism that drives tumor selectivity is its interaction with the cellular antiviral response. PV elicits and IFN response in untransformed cells, but can prevent induction of IFN stimulated genes (ISG) in tumor cells. The mechanism by which PV achieves this is not fully understood yet. Interestingly, preinfection with PV is sufficient to prevent IFN signaling in response to common triggers. [108]

Preclinical studies in immortalized cell lines, patient-derived tumor models, and mouse (MVM) and rat (H-1PV) models have demonstrated therapeutic efficacy in a variety of tumor entities, such as melanoma, breast cancer, glioblastoma, and pancreatic carcinoma.[73] The safety of the application in humans has also been demonstrated in two clinical studies conducted at Heidelberg University Hospital, in which patients with recurrent glioblastoma (ParvOryx01, Phase I/II) or inoperable metastatic pancreatic carcinoma (ParvOryx02, Phase II) were treated with H-1PV. In addition to the promising safety data, signs of an induced immune response were also observed.[16,31]

1.3.1.3. IFNs and oncolytic virotherapy

The interplay of type-I interferons (IFN) and oncolytic virotherapy is complex. As the first line of defense against virus infections, active IFN signaling can prevent susceptibility to OVs and limit their therapeutic efficacy. On the contrary, for OV-mediated immune induction of an adaptive immune response, IFN signaling is vital. Additionally, restricted intrinsic IFN signaling in cancer cells conveys a safety aspect, when applying IFN-sensitive viruses. Thus, the modulation of the IFN response has been an active area of research in the virotherapy field.[109-111]

Viral infections in IFN-competent tumor cells are sensed by pattern recognition receptors (PRR). Depending on the viral genome, these include retinoicacid-inducible gene-1 (RIG-I) or melanoma differentiation associated protein 5 (MDA-5) to sense foreign RNA or cyclic GMP-AMP synthase (cGAS) to sense damaged or foreign DNA. Activation of PRRs triggers downstream signaling cascades leading to nuclear translocation of the transcription factors nuclear factor kappa B (NFκB) and IFN regulatory factors (IRF) 3 and 7.[112] In the nucleus, they induce transcription of IFNB1 and members of the IFNA family. Once translated, these IFNs are released from the cell and induce autocrine and paracrine signaling by binding their receptor, a heterodimer of IFN-α receptor 1 and 2. Ligand binding induces activation of the receptor-

associated kinases tyrosine kinase (TYK) 2 and janus kinase (JAK) 1, which in turn leads to phosphorylation of signal transducer and activator of transcription (STAT) 1 and 2. Phosphorylated STAT1 and STAT2 bind IRF9, forming the interferon-stimulated gene factor 3 (ISGF3). ISGF3 translocates to the nucleus and binds IFN-stimulated response elements (ISREs). ISREs are consensus sequences in the promoter regions of IFN stimulated genes (ISGs). When the complex binds an ISRE, transcription of the ISG is induced. Now, a broad range of ISGs is transcribed, including classical antiviral effectors like the interferone-induced transmembrane protein family (IFITM) and protein kinase R (PKR), chemokines such as C-X-C motif chemokine 10 (CXCL10) or multifunctional proteins like ISG15. Notably, several components of the signaling cascade, such as STAT1, are themselves ISGs, forming a positive feedback loop that amplifies the response. The coordinated expression of these ISGs establishes an antiviral state and can severely limit viral replication.[113,114]

Different strategies have explored the modulation of the IFN response to increase OV efficacy or safety. One approach involved engineering the IFN-sensitive Newcastle disease virus (NDV) to encode the influenza A NS1 protein, a known antagonist of the IFN response. This enhanced virus replication and cytotoxicity and elicited a stronger T cell mediated immune response *in vivo*. [115] On the contrary, another strategy aims to increase IFN signaling to improve viral safety. For instance, vesicular stomatitis virus (VSV) has been engineered to express IFN-β, thereby restricting viral spread in normal tissues and reducing systemic toxicity in preclinical models and clinical trials.[116,117] Together, these examples illustrate the complex, context-dependent interplay between IFN signaling and virotherapy, emphasizing the need for rational, spatiotemporally controlled modulation of this pathway.

1.4. Radioviroherapy

Virotherapy offers many advantaged, including an excellent safety profile observed in clinical studies to date.[118] However, only isolated cases of long-term remissions have been reported[119] and substantial therapeutic benefit and objective response rates are often limited, when OVs are applied as monotherapies.[120] In addition to encoding transgene to enhance therapeutic outcomes, combination therapies are investigated. Among these, radiotherapy is a promising combination partner.[121]

The rational to investigate radiovirotherapy as a promising combination approach is multifaceted: Practical reasons include the comparatively low cost, the widespread availability of centers technically equipped to deliver radiotherapy and the high number of patients that receive radiotherapy during the course of their disease.[39] Additionally, the distinct and non-overlapping spectra of adverse events between radio- and virotherapy reduces the likelihood of dose-limiting toxicities in the combination.[122,123]

Beyond practical considerations, the combination also has the potential to synergize mechanistically OVs may enhance the radiosensitivity of tumor cells, while radiotherapy can facilitate viral spread by disrupting tumor architecture and modulating the tumor microenvironment.[124] Both therapies elicit immunogenic cell death and could induce enhanced immune activation.[47] Multiple preclinical and clinical trials have thus investigated radiovirotherapy.

Oncolytic adenoviruses have been assessed in combination with radiotherapy for two decades.[125] An adenovirus engineered to express wild-type p53 conferred a radiosensitizing effect on NSCSL tumor cells, but not untransformed lung fibroblasts[126] Goerger *et al.* showed that the combination led to a delayed tumor growth of patient-derived xenografts of human glioma *in vivo.*[127] For PDAC, Dai *et al.* showed synergy of vaccinia virus and radiation. They observed increased levels of apoptosis *in vitro* and a prolonged survival of mice bearing human pancreatic tumor xenografts[128]

Promising preclinical data has led to several clinical studies investigating radiovirotherapy. While safety was shown for the combination of radiotherapy and T-VEC[129], HSV-1[130] and Vaccinia virus[131], no study showed a therapeutic benefit. Notably, a study employing an adenovirus and radiotherapy in pediatric patients with diffuse intrinsic pontine glioma did see induction of T cell activity and tumor response to the treatment, but this was also associated with adverse events.[132] This underlines the needs to rationally modify such treatment regimens to enhance therapeutic efficacy while maintaining safety.

No clinical studies have evaluated the combination of MeV or PV with radiation, but there is promising preclinical data: Radiovirotherapy with PV elicited enhanced cytotoxicity in radioresistant and radiosensitive glioma cultures.[16] MeV has been investigated in combination with radiotherapy in glioma[133,134], PDAC[135], prostate cancer[136] and head and neck squamous cell carcinoma (HNSCC)[135]. Previous work within our group and of my Master's thesis showed synergy in PDAC and HNSCC, accompanied by enhanced levels of immunogenic cell death and innate immune activation.[86,135] However, the assessment of the combination in an immunocompetent syngeneic murine model of HNSCC showed no therapeutic benefit compared to monotherapy with radiation. Albeit enhanced TILs and anti-viral immune induction was observed, this did not confer enhanced survival.[135] Building on these findings, I aimed to rationally modify the combination regimen to further improve its efficacy. The investigation of this modified triple radiovirotherapy approach constituted the central objective of this thesis.

2. Aim of the Study

Promising preclinical data indicates the benefits of combining radiotherapy and immunotherapeutic approaches, specifically oncolytic virotherapy. While we and others have observed enhanced cytotoxicity and favorable immune induction patterns, in-depth and transcriptome-wide analysis of the combination of MeV and radiotherapy has not yet been undertaken. In addition, we hypothesize that the induction of innate immune signaling at early time points of MeV infection might hamper the replication of the oncolytic virus and ultimately decrease immune induction and therapeutic efficacy. I thus want to assess if modulation of the early IFN response can boost radiovirotherapy. Since the onco-selectivity is a key advantage of oncolytic viruses in general and MeV specifically and is demonstrated by an excellent safety profile in clinical studies, I aim to transiently and tumor-selectively dampen the IFN response by applying a second oncolytic virus with that property, namely parvovirus.

The following aims are thus addressed in this thesis:

1. Analysis of the transcriptional alterations induced by the combination of MeV and radiotherapy
2. Identification of candidate tumor cell lines with intact intrinsic capacity to induce IFN signaling
3. Assessing cytotoxic effects and potential synergy of dual virotherapy of PV and MeV
4. Assessing cytotoxic effects, potential synergy and underlying mechanism of triple radiovirotherapy

By comprehensively analyzing the rationally modified radiovirotherapy in terms of cytotoxicity, synergy and mechanism of action, we hope to provide preclinical data to underline the potential of radiovirotherapy in translational efforts.

3. Materials & Methods

3.1. Materials

3.1.1. Cell lines

Table 1: Cell lines, media and seeding density

	Origin & Tissue	Medium	96-well	12-well	6-well	Supplier
U87	Human GBM	DMEM	$1*10^4$	$1*10^5$	-	R. Cattaneo, Mayo Clinic, Rochester, MN
U251	Human GBM	DMEM	$1*10^4$	$1*10^5$	$3*10^5$	Christiane Opitz, DKFZ, Heidelberg
U373	Human GBM	DMEM	$1*10^4$	$1*10^5$	-	Laurent Daeffler, IPHC, Strasbourg, France
BxPC-3	Human PDAC	RPMI	$2*10^4$	$1.5*10^5$	$4.5*10^5$	ATCC, Manassas, VA
T3M4	Human PDAC	RPMI	$1*10^4$	$1*10^5$	-	Zahari Raykov, DKFZ, Heidelberg
GL261	Murine GBM	DMEM	$1*10^4$	$1*10^5$	-	Laurent Daeffler, IPHC, Strasbourg, France
PDA30364	Murine PDAC	DMEM 1 % Sodium Pyruvate	$1*10^4$	$1*10^5$	-	Rienk Offringa, DKFZ, Heidelberg[137]
m24192	Murine PDAC	DMEM	$1*10^4$	$1*10^5$	-	Rienk Offringa, DKFZ, Heidelberg
Vero	African Green Monkey Kidney Epethial	DMEM	$2*10^4$	-	-	ATCC, Manassas, VA
ASAN-PaCa	Human PDAC (patient-derived)	-	-	-	-	Used in spheroid experiments, provided by Assia Angelova[138]
HUVEC	Primary human endothelial cells (not malignant)	-	-	-	-	Used in spheroid experiments, provided by Assia Angelova
MRC-5	Human fibroblasts (not malignant)	-	-	-	-	Used in spheroid experiments, provided by Assia Angelova
	Volume for culture		100 µl	1 ml	2 ml	
	Volume for infection		50 µl	200 µl	500 µl	

3.1.2. Chemicals and reagents

Table 2: Chemicals and reagents

Material	Catalog No / Manufactrure
4’,6-diamidino-2-phenylindole (DAPI)	4’,6-diamidino-2-phenylindole (DAPI)
4-20% Mini-PROTEAN TGX stainfree protein Gels	4568093, Bio-Rad Laboratories
Acetic Acid	3738.4, Carl Roth GmbH
Antibiotic antimycotic solution (ABAM)	A5955, Sigma-Aldrich
Bacillol	973380, Hartmann
Bovine serum albumin (BSA)	A9418, Sigma-Aldrich
Clarity Max™ Western ECL Substrate	1705062, Bio-Rad
Crystal violet (powder)	C6158, Sigma-Aldrich, Saint Louis, MO/USA
Dako fluorescence mounting medium	S3023, Agilent, Santa Clara, CA/USA
Dimethyl sulfoxide (DMSO)	D2438-5X, Sigma-Aldrich
Dulbecco’s Modified Eagle’s medium (DMEM)	31966, Gibco Life Technologies
Dulbeccos’s phosphate-buffered solution (D-PBS)	14190-144, Gibco Life Technologies
ELISA Stopsolution	SS04, Thermo Scientific
Elution buffer (EB)	19086, Qiagen, Hilden, Germany
ERDRP-0519	HY-102074, MedChem Express
Ethanol (for experiments)	32221, Sigma-Aldrich
Ethanol, denatured (for cleaning)	1.00974, Sigma-Aldrich
Fetal calf serum (FCS)	P40-37500, PAN-Biotech GmbH, Aidenbach, Germany
Fugene® HD transfection reagent	E231A, Promega, Madison, WI/USA
Halt™ Protease and Phosphatase Inhibitor Cocktail (100X)	78440, Thermo Scientific
Hoechst 33342	H1399, Invitrogen Life Technologies
IFN-β, recombinant	#AF-300-02B, Peprotech
Incidin Rapid	3025510, Ecolab
Methanol, purity above 99.9%	4627.2, Carl Roth GmbH
Opti-MEM™	51985, Gibco Life Technologies
Oxywipes	PZN 18703096, Dr. Schumacher
Paraformaldehyde (PFA) solution, 4%	19943, Affymetrix, Santa Clara, CA/USA
Polybrene (Hexadimethrene bromide)	TR-1003, Sigma-Aldrich
Power SYBR™ Green PCR Master Mix	4367659, Applied Biosystems
Precision Plus™ protein all blue standards	1610373, Bio-Rad Laboratories
Protease Inhibitor Cocktail cOmplete™ Ultra tablets	5892970001, Roche, Basel, Switzerland
Puromycin dihydrochloride	A11138-03, Gibco Life Technologies
RIPA Buffer	R0278, Sigma-Aldrich
RNAlater	1017980, Qiagen
RNAse H	M0297L, New England Biolabs
Roswell Park Memorial Institute (RPMI) 1640	61870, Gibco Life Technologies
ROTI®-Stock, 10× tris-buffered saline-tween (TBST)	1061.1, Carl Roth GmbH
Rotiphorese® SDS-PAGE	3060.1, Carl Roth GmbH
Skim milk powder, blotting grade	T145.2, Carl Roth GmbH
Sodium pyruvate	11360, Gibco Life Technologies

TMB substrate solution	N301, Thermo Scientific
Triton™ X-100	X100, Sigma-Aldrich
Trypan Blue solution, 0.4%	T8154, Sigma-Aldrich
Trypsin-ethylenediaminetetraacetic acid (EDTA) solution, 0.05%	25300, Gibco Life Technologies
Tween 20	655204, EMD Milipore Corp
β-mercapoethanol, purity above 99%	M7522, Sigma-Aldrich

3.1.3. Kits

Table 3: Kits

KMaterial	Catalog No / Manufactrure
BCA Protein Assay Kit	71285-3, Merck Millipore
CellTiter-Glo® 3D Cell viability Assay	G9681, Promega
Human CXCL10/IP-10 DuoSet ELISA	DY266, R&D
Human IFN-beta DuoSet ELISA	DY814, R&D
Qubit RNA IQ Assay	Q33221, Thermo Fisher Scientific
RNAse free DNAse	79254, Qiagen
RNeasy Plus Mini	74136, Qiagen
Trans-Blot Turbo RTA Midi 0.2 µm PVDF Transfer Kit	1704273, Bio-Rad Laboratories
XTT Zell Proliferation assay	Biotium, 30007

3.1.4. Machines

Table 4: Machines

Material	Catalog Number
Cell sorter	BD FACSAria™ II
Chemi-Doc Imaging System	12003154, Bio-Rad Laboratories
Flow cytometer	BD CANTO II
IncuCyte	SX5, Sartorius
qPCR cycler	CFX96, Bio-Rad Laboratories, Inc.
Spectrophotometer (Plate Reader)	M200, Tecan Trading AG, Switzerland

3.1.5. Software

Table 5: Software

Software	Version	Supplier
ChatGPT	GPT-5	Open AI
FACS Diva software	Version 8.0.1	BD Bioscience
FIJI	Version 2.1.0	Open Source
FlowJo	V10	BD Bioscience
GraphPad Prism	10.5.0	Graph Pad, San Diego, CA/USA

iControl Software	Version 3.9.1.0	Tecan Austria GmbH
Rstudio	2025.05.1 Build 513	Posit Software

3.1.6. Antibodies

Table 6: Antibodies

Antibody	Description	Application and dilution	Manufacturer
Anti pEIF2a	detects Ser51-phophorylation; rabbit polycloncal antibody	WB, 1:500	#9721, Cell signaling
Anti Puromycin	mouse, monoclonal IgG2aκ, clone 12D10	WB, 1:10,000	MABE343, Sigma-Aldrich
Anti-human calreticulin	Rabbit IgG, clone D3E6	IF 1:100	12238, Cell Signaling Technology
Anti-human ISG15	mouse monoclonal IgG1 κ, clone F-9	WB, 1:1000	sc-166755, Santa Cruz Biotechnology Inc.
Anti-human STAT1	mouse monoclonal IgG1 κ, clone C-136	WB, 1:1000	sc-464, Santa Cruz Biotechnology Inc.
Anti-mouse CD16/CD32	Rat (SD) IgG2b, clone 2.4G2 (murine FC block)	FC 1:100	553142, BD biosciences
anti-mouse IgG HRP antibody	Horse, secondary antibody, HRP-coupled for WB	WB, 1:20000	7076, Cell Signaling
Anti-NS1	SP8, rabbit polyclonal serum	1:20000	provided by Jörg Nüesch
Anti-rabbit IgG (H+L)-Alexa Fluor® 594	Goat, secondary antibody	IF 1:200	A11012, Invitrogen Life Technologies
anti-rabbit IgG HRP antibody	Goat, secondary antibody, HRP-coupled for WB	WB, 1:2000	#7074, Cell Signaling
APC anti-human CD46	Mouse IgG1, κ	FC 1:100	352405, Biologend
APC Mouse IgG1, κ Isotype Ctrl Antibody (0.2 mg/mL)		FC 1:100	400120, Biolegend
mAB anti-beta-actin POD	mouse monoclonal IgG1, clone AC-15	WB, 1:20000	A3854, Sigma-Aldrich

3.1.7. Oligonucleotides

Table 7: Oligonucleotides

Target	Direction	Sequence	Annealing temperature [°C]
ACTB	for	TCATTGCTCCTCCTGAGCGCA	54
	rev	CTAGAAGCATTTGCGGTGGAC	
CXCL10	for	GCTTCCAAGGATGGACCACA	60
	rev	GCAGGGTCAGAACATCCACT	
DDX58	for	TGCGAATCAGATCCCAGTGTA	60
	rev	TGCCTGTAACTCTATACCCATGT	
ISG15	for	CGCAGATCACCCAGAAGATCG	52

	rev	TTCGTCGCATTTGTCCACCA	
IFITM1	for	TCGCCTACTCCGTGAAGTCT	52
	rev	TGTCACAGAGCCGAATACCA	
IFNB1	for	gacgccgcattgaccatcta	60
	rev	ccttaggatttccactctgact	
MeV	for	GGCCCAGCAGAGCAAGTGATG	60
	rev	TTCCCAAAGTTTCAGCGTCAT	
PKR	for	ACGCTTTGGGGCTAATTCTTG	52
	rev	CCCGTAGGTCTGTGAAAAACTT	
TLR3	for	TTGCCTTGTATCTACTTTTGGGG	60
	rev	GCAGGGTCAGAACATCCACT	

3.1.8. Plasmids

Table 8: Plasmids

Name	**Description**
pcDI-DsRed2	Eukaryotic expression vector encoding a variant of the Discosoma red fluorescent protein
pCG-L	Eukaryotic expression vector encoding MeV L protein
pCG-N	Eukaryotic expression vector encoding MeV N protein
pCG-P	Eukaryotic expression vector encoding MeV P protein
pcMeVac ld-EGFP	Eukaryotic expression vector encoding for antigenome of MeV Schwarz vaccine strain

3.1.9. Viruses

Table 9: Viruses

Virus	**Description**
LV-105 hCD46 BC1	Replication-deficient lentivirus encoding human CD46 isoform BC1, kindly provided by Johannes Heidbüchel
MeVac ld-EGFP	Measles Schwarz vaccine strain virus encoding for eGFP in ATU downstream of leader
Parvovirus	H-1PV parvovirus, generated and provided by Barabara Leuchs

3.2. Methods

3.2.1. Cell Culture

3.2.1.1. General handling

For routine cell culture, I cultured cells in tissue culture flasks (T-75) at 37°C with 5% CO_2 in a humidified incubator with 12 ml of cell culture medium. Cell lines and matched media are summarized in (**Table 1**). I performed all cell culture under sterile conditions (laminar flow hood) and in accordance to biosafety level 1 or 2 (BSL1/2) regulations, depending on the requirements of the experiment. Bacillol AF was used as standard disinfectant, Incidin Plus or Oxywipes were used after use of non-enveloped viruses. I changed the medium regularly and subcultured cells at a ratio of 1:2 to 1:100, depending on the cell lines growths kinetics and experimental needs when cells reached a conflucency of ca. 90 %. For subculture, I washed the cells once with D-PBS and added 3 ml of Trypsin. Once cells detached, I inactivated the trypsin by addition of 7 ml serum-containing medium. I returned the resulting cell suspension to the flask at the indicated ratio. To count cells, I mixed 10 µl of cell suspension with Trypan-Blue for live dead discrimination at a 1:2 ratio. I added 10 µl to a Neubauer hemocytometer and averaged the count across the four corner grids. Since each grid holds 0.1 mm^3, I multiplied the resulting number with 10^4 to calculate the cell number per ml.

For long-term preservation, I froze 10^6 cells in 1 ml culture medium additionally supplemented with 5 % dimethyl sulfoxide (DMSO) slowly cooling them at a rate 1°C per minute by using a CellCamper® freezer box (Neolab) at -80°C. After 1-4 days, I transferred the frozen cell suspensions to liquid nitrogen for long-term storage. To thaw cryopreserved cells, I placed the vials in a waterbath at 37°C until fully thawed and added the cell suspension dropwise to prewarmed medium in a culture flask. After 24 h, I changed the medium.

The cell lines were routinely tested for *Mycoplasma* contamination. To facilitate this, I harvested supernatant of cultured cells at least 24 h after a medium change and inactivated it at 95°C for 10 min. Mycoplasma detection by PCR was performed by lab technicians. For additional quality control, the cell lines were authenticated and tested for contaminations in services provided by Multiplexion (Heidelberg, Germany). [139,140]

3.2.1.2. Treatment and virus infection

If not stated otherwise, all treatments followed the following schedule (**Figure 3-1**): I initiated the treatment ca. 24 h after cell seeding. When I performed X-ray irradiations, I used the MultiRad 225 system (Faxitron Bioptics, LLC., Tucson, AZ/USA), placed the culture dishes inside the cabinet using shelf position

4 and irradiated at a dose rate of 2.151 Gy/min. I used a 0.5 mm copper filter and a fixed voltage of 200 kV and current at 17.8A. For drug or virus treatments, I removed the culture medium, washed cells once with D-PBS and added the respective treatment in OptiMEM: For viral infections, I adjusted the virus concentration (plaque forming units (PFU)/ml for PV stocks and cell infectious units (ciu)/ml for MeV) to the correct multiplicity of infection (MOI). After 1 h (PV) or 2 h (MeV) of incubation at 37°C with 5% CO, I removed the inoculant and replaced it with culture medium. For treatment with Poly(IC), I diluted stock solution in OptiMEM to the indicated concentration and added it directly to the cells. For 12- and 96-well formats, technical triplicates were prepared and averaged (96-well) or pooled (12-well) for measurements or harvests, respectively.

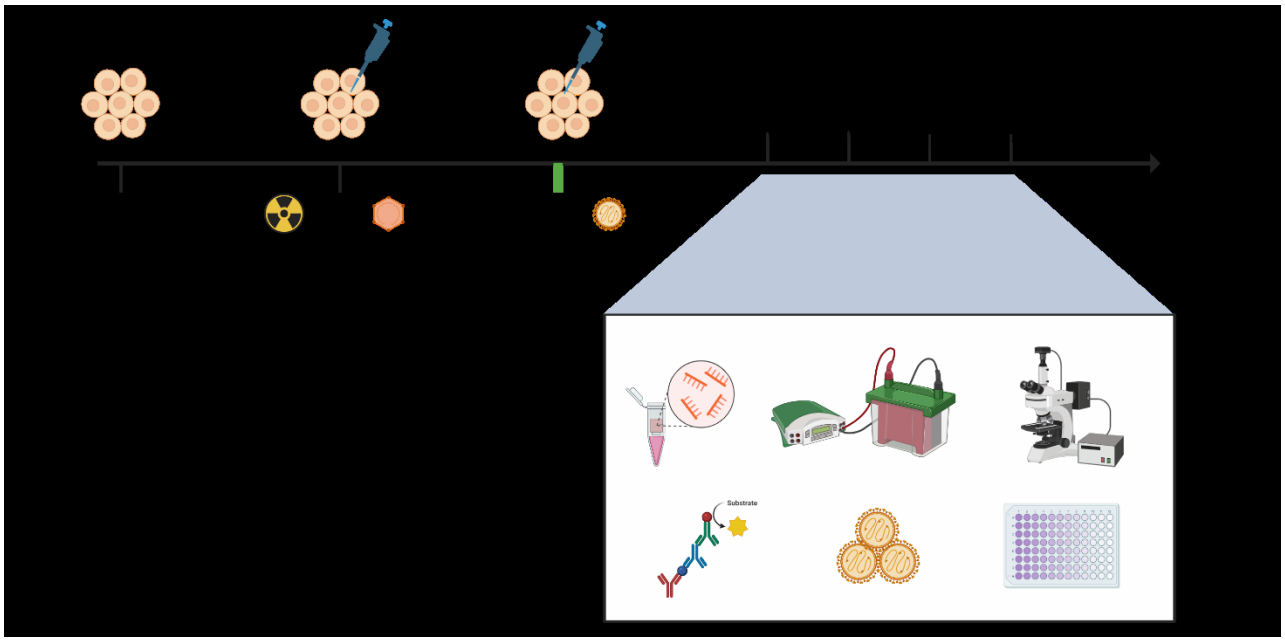

Figure 3-1: Schedule for (R)VTx treatments

I performed combination treatments with the following schedule: I seeded cells and initiated treatment 24 h later. Radiation was applied first, directly followed by infection with Parvovirus. 24 h thereafter, I applied MeV. I harvested and performed readouts at various timepoints within the treatment window ("post radiation" (p.r.)) and after completion of the treatment ("post treatment" (p.tr.))

3.2.1.3. Cytotoxicity assays for monolayer cultures

To determine cytotoxic effects of the treatment applied in monolayer cultures, I performed either XTT or crystal violet assays. For either assay, I seeded and treated cells in 96-well plates as described above and incubated them thereafter for the time indicated.

XTT assay exploits the ability of dehydrogenases in metabolically active cells to reduce tetrazolium salts to orange-colored formazans. In contrast to the classical MTT, the tetrazolium salt XTT (2,3-bis(2-methoxy-4-

nitro-5-sulfophenyl)-5-[(phenylamino)carbonyl]-2H-tetrazolium hydroxide) yields a water-soluble formazan upon reduction. Then, by measuring the optical density using a spectrophotometer, the colored product can be quantified without the need for a solubilization step.[141] To perform the XTT assay, I added activation reagent to XTT solution at a ratio of 1:200. Subsequently, I added 50 µl of the solution to the 100 µl medium in each well and included controls with medium only for background subtraction. Approximately 2 h after addition of XTT solution, I read the optical density at 450 nm with 640 nm as reference wavelength.

To perform crystal violet assays, I washed the cells once with PBS and fixed them with 4 % Paraformaldehyde (PFA) for 30 minutes. After removal of PFA, I stained the cell layer with crystal violet solution (0.5 % crystal violet powder in 1:1 H_2O and Methanol) and incubated for 15 minutes at room temperature. After removal of the staining solution, I washed twice with water and dried the plates overnight. I took images for qualitative assessment and subsequently dissolved the stain in with 10 % acetic acid in H_2O. I measured OD at 590 nm with a spectrophotometer.

3.2.1.4. (Fluorescent) microscopy and live cell imaging

For routine observation of cells in culture and experiments, I used a Zeiss Axiovert 40. For image acquisition, I used a Zeiss Axiovert 200 microscope. Since the virus construct I routinely used encoded for eGFP, I could visualize viral spread through fluorescent microscopy. As fluorescence source, I used either a mercury short-arc based Zeiss HBO 100 or LED-based X-Cite Xylis II. Images were acquired with Zeiss AxioVision Software.

For real-time imaging over longer periods of time, I used a SX 5 IncuCyte. I plated cells in 96-well plates and treated them as described above. I acquired 4 images per well with the 10x objective every 2-3 hours over 3-7 days. For data analysis, I used the IncuCyte software, keeping parameters constant for each cell line and experiment performed. I analyzed phase and eGFP area as measures for cytotoxicity and viral transgene expression, respectively. To quantify and compare viral transgene expression between treatment groups, I calculated the area under the curve (AUC) using GraphPad Prism.

3.2.1.5. PDAC spheroids

To better model the complex interaction of dual viro- or triple radiovirotherapy, I used heteregenous PDAC spheroids. Spheroids were provided by Assia Angelova and her team. They generated the spheroids with $1*10^4$ PDAC cells (ASAN-PaCa cell line[138]), $2*10^4$ endothelial cells (HUVEC) and $3*10^4$ fibroblasts (MRC-5) using the hanging drop method.[142] 24 h later, they transferred the spheroids in a U-Bottom 96-well plates. On the day of the transfer, I initiated the treatment following the same schedule as described for the

monolayer experiments (**Figure 3-1**). For virus infection, I diluted the required amount of virus in OptiMEM and directly added 10 µl of virus suspension to the spheroids which were cultured 70 µl medium. I calculated the MOI to the total cell number ($6*10^4$ cells) not just PDAC cells. I performed all experiments with technical triplicates.

I conducted sampling for RNA and ELISA in parallel: At the indicated timepoints, I pooled the technical replicates in 1.5 ml cups and centrifuged for 5 min at 300 g. I transferred the supernatant to PCR stripes for ELISA and directly froze at -80°C. I washed the remaining pellet with PBS and finally resuspended in 200 µl RNAlater. I continued as described in the respective sections with RNA isolation and ELISA (**3.2.3.1** and **3.2.3.4**).

To analyze cytotoxic effect of the treatment, I performed CellTiterGlo® 3D assays. The reagent used in this assay is lytic and quantifies cellular ATP through a luciferase reaction. After equilibrating the reagent and plate to room temperature, I added the reagent to each well in an amount equal to the amount of culture medium. I mixed by orbital shaking for 5 mins using the plate reader. Subsequently, I let the plate rest for 25 mins and then transferred the mix to white 96-well plates. I recorded the luminescence with the Tecan plate reader set to an integreation of 4 seconds per well

3.2.1.6. Generation and characterization of murine PDAC and GBM cell lines stably expressing human CD46

For assessment of MeV treatment in syngeneic murine tumor models, murine cell lines are required that stably expressed MeV entry receptor human CD46. To this end, I performed lentiviral transduction of murine cell lines, followed by (single) cell sorting and characterization of the resulting clones.

As murine PDAC models, I used the PDA30364 cell line and m24192, both generated in the lab of Rienk Offringa and generously provided. Both cell lines are generated from primary pancreastic tumors of genetically engineered C57BL/6-Ly5.1 mice.[137] For GBM, I used the GL261 cell line, equally of a C57BL/6 background, which was acquired and provided by Laurent Daeffler.

To stably transfect the cell lines with human CD46, I used lentiviruses previously generated in the lab by Johannes Heidbüchel. These replication-deficient lentiviruses encode the BC1 isoform of human CD46. For lentiviral transduction, I seeded the cell lines in 12-well plates. When cells reached 70 % confluence, I washed the wells with D-PBS and added 800 µl cell-specific medium containing 8 µg/ml polybrene and lentivirus stock at a dilution of 1:100. One day later, I changed the medium. Once cells reached confluence, I transferred them to T25 and subsequently to T75 cell culture flasks. Once cell reached confluence in T75 flasks, I performed fluorescence-activated cell sorting (FACS). I harvested cells and counted cells, as

described above. I used $6*10^6$ cells as input for cells to be sorted. I centrifuged the cell suspension at 300g for 5 minutes and washed once with D-PBS. I suspended in 100 µl D-PBS/10^6 cells and added murine FC block at a dilution of 1:100. After 5 minutes of incubation, I stained cells with anti-CD46 antibody or isotype control for 30 minutes at RT in the dark. Subsequently, I added 500 µl D-PBS and spun the cells down at 300g for 5 minutes. I removed the supernatant and resuspended in 500 µl D-PBS containing 0.1 µg DAPI/ml. I incubated samples for 5 minutes in the dark and finally added 1 ml D-PBS. I then centrifuged the cells again at 300g for 5 minutes, removed the supernatant and resuspended in 500 µl D-PBS. I transferred the samples into FACS tubes. I used a BD FACSAria to sort cells and performed single cell as well as bulk sorting into 96-well plates containing cell-specific medium, 30 % FCS and 1 % antibiotic antimycotic solution (ABAM). I incubated the plates and observed the growth of single cell clones or bulk populations daily. I let cells outgrow from 96- to 48-, 12-, 6-well formats and finally into T25 and T75 culture flasks, when the clones or bulk-sorted populations reached sufficient confluence. To characterize the generated cell lines for CD46 expression, I performed flow cytometry by staining the cells with CD46 antibodies as described above and analyzing the samples on a FACS Canto II.

3.2.1.7. SUnSET assay

To assess treatment-induced changes in the protein synthesis rate, I performed "surface sensing of translation" (SUnSET) assays following the published protocol.[143] The assays exploits the structural analogy of puromycin to aminoacyl-tRNAs. This results in the incorporation of puromycin into nascent proteins through non-hydrolysable peptide binding during translational elongation. This terminated elongation and puromycin-labeled proteins are released from the ribosome. Low concentration of puromycin do not alter the overall protein synthesis rate, which can thus be assessed by quantifying puromycin-labeled proteins. To perform the assay, I seeded and treated cells as described above. 48 h after completion of treatment, I added puromycin directly to each well at a final concentration of 5 µg/ml. After exactly 15 minutes of incubation, I removed the medium, washed cells with cold PBS and continued with cell lysis by RIPA buffer, SDS-PAGE and Western Blot and quantification, as described in **3.2.3.5**.

3.2.2. Virological methods

3.2.2.1. Rescue of recombinant measles virus

To generate recombinant measles virus particles, I followed the previously published protocols.[144] Briefly, I seeded $5*10^5$ Vero cells per well of a 6-well plate. Once attached, I prepared the following transfection mix:

Table 10: MeV rescue transfection mix

Reagent	**Volume [amount]**
NPL Mix	11 µl [containing 500 ng each pcDIMER N and P and 100 ng pcDIMER L]
Mev antigenome	X µl [containing 5 µg]
pcDI-dsRed	1 µl [containing 100 ng]
DMEM	200 µl
FuGene HD	18.6 µl

First, I added plasmid components to DMEM, mixed and centrifuged briefly. I then added the transfection reagent. After mixing and brief centrifugation, I incubated the transfection mix for 25 minutes at RT. In the meantime, I changed the mediium of seeded Vero cells to 1.8 ml DMEM per well containing 2 % FCS and 50 µg/ml Kanamycin (transfection medium). I then added the transfection mix dropwise, rocked the plate gently and incubated at 37°C. I changed medium on the next day to 2 ml of fresh transfection medium. I observed the cells daily for syncytia formation or eGFP expression, when the MeV construct containing eGFP was rescued. When a sufficient amount of syncitia was present (usually 4-6 days after transfection), I scraped the cells into the medium, resuspended the mixture and either directly transferred for a first viral passage (VP1) or frozen at -80°C.

3.2.2.2. Propagation of virus constructs

For the VP1, I seeded $2.5*10^6$ Vero cells on a 10 cm dish. 24 h thereafter, I removed the medium and thawed or directly added the rescue suspension mixed with OptiMEM in a total volume of 4 ml. Two hours after the inoculation, I added 6 ml of DMEM containing 10 % FCS. I again incubated the VP1 at 37°C until the cell layer was completely infected. Then, I removed the medium completely, added 500 µl of OptiMEM, scraped the cells, transferred them to a 1.5 ml Eppendorf cup, vortexted and froze the suspension rapidly in liquid nitrogen. After at least 24 h at -80°C, I thawed the suspension in a 37°C water bath, vortexed and centrifuged at 5000 g for 10 minutes at 4°C. I aliquoted the supernatant and determined the viral titer (see **3.2.2.3**). To propagate viruses, I performed up to three additional viral passages. To generate VP2 and subsequent passages, I seeded $5*10^6$ Vero cells in 15 cm dishes. 24 h after seeding, I added the previous at an MOI of 0.03 in 8 ml OptiMEM. After ca. 7-8 h, I added 8 ml DMEM 10 % FCS. I observed the infection progression daily and harvested, when 90 % of Vero cells were in syncytia with a tense membrane structure. Then, I completely removed the media and scraped the cells. I collected the virus suspension from all plates and snap froze the pooled suspension in liquid nitrogen. Once thoroughly frozen, I transferred it to -80°C. Later, I aliquoted the suspension in cryotubes for storage at -80°C. I determined

the titer of each aliquot size and determined titer stability after storage of the suspension at 4°C for 72 h. I only used passages of stable titer and minimal vial-variability for experiments.

3.2.2.3. *Virus quantification (serial dilution titration)*

I determined viral titers (colony-infecting units per ml) by serial dilution titration assay: Vero cells were harvested and concentration adjusted to $2*10^5$ cells/ml. For each virus suspension to be quantified, I prepared a 96-well plate containing 90 µl of DMEM wit 10 % FCS per well. I vortexed the virus suspension briefly and added 10 µl virus solution to each well of the first column. I mixed thoroughly and transferred 10 µl to the wells of the next column. I repeated this until the final column. I then directly added 100 µl of the prepared Vero cell suspension to each well and incubated the plate at 37°C for 72 h.

After 72 h, I read the titers by counting the number of syncytia formed in each well of the column showing a countable amount of syncytia. By averaging the counted number across the 8 replicates in the column, the titer can be determined (**Figure 3-2**).

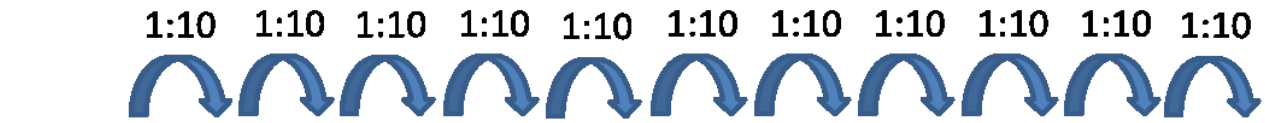

	10 µl	1µl	0,1µl	0,01µl	1nl	0,1nl	0,01nl	1pl	0,1pl	0,01pl	1fl	0,1fl
	10^{-2}_{ml}	10^{-3}	10^{-4}	10^{-5}	10^{-6}	10^{-7}	10^{-8}	10^{-9}	10^{-10}	10^{-11}	10^{-12}	10^{-13}
	$= 10^2$ ciu/ml	$= 10^3$ ciu/ml	$= 10^4$ ciu/ml	$= 10^5$ ciu/ml	$= 10^6$ ciu/ml	$= 10^7$ ciu/ml	$= 10^8$ ciu/ml	$= 10^9$ ciu/ml	$= 10^{10}$ ciu/ml	$= 10^{11}$ ciu/ml	$= 10^{12}$ ciu/ml	$= 10^{13}$ ciu/ml
A												
B												
C												
D												
E												
F												
G												
H												

Figure 3-2: Plate Layout for virus quantification and titer determination

3.2.2.4. *Multi-step growth curves*

To test permissiveness of different cell lines to virus infection and replication, I performed multi-step growth curves. Here, cells are infected at a low MOI to allow for multiple rounds of infection. I seeded $2*10^5$ cells per well of a 6-well plate and infected the cells 24 h later at an MOI of 0.03 with MeV ldeGFP.

When I removed the inoculum after the infection, I added only 1 ml of culture medium to maximize the viral particle concentration. At 24, 36, 48, 72 and 96 h p.i., I observed the cells and infection progress under the fluorescent microscope and harvested cells by scraping and resuspending them in the culture medium. I transferred cells to 1.5 ml Eppendorf cups and snap froze them in liquid nitrogen. I then stored them at -80°C. Once all time points were collected, I quantified the viral particles by serial dilution titration following the previously described protocol, in principle (**3.2.2.3**). I only used 5 dilution steps and thus titrated two samples per 96-well plate.

3.2.3. Molecular Biology Techniques

3.2.3.1. RNA isolation

To harvest cells for RNA isolation, I washed cells once with D-PBS and added Trypsin. Once cells detached, I pooled replicate wells (usually 3 wells of a 12-well plate) and spun the suspension down at 300 g for 5 mins. After washing the cell pellet once with D-PBS, I resuspended the pellet in 200 µl RNAlater and stored the samples at -20°C until RNA isolation. For RNA isolation, I thawed the samples on ice and spun them down at 5,000g for 5 minutes. I removed the supernatant and resuspended the pellet in the RLT plus buffer of the RNeasy Plus kit, containing 10 µl β-Mercaptoethanol per 1 ml buffer. I homogenized the resulting lysate through a QIAshredder column by centrifugation at 16,000 g for 2 minutes. All subsequent steps were performed with the RNeasy Mini kit in accordance to the manufacturers instructions. For all sampes, an additional on-column DNAse digest was performed with the RNAse free DNase Kit (Qiagen) as described in Appendix D of the manufacturers handbook. I eluted twice with 30-50 µl RNAse free water, reusing the eluate. I determined the RNA concentration with a Nano-Drop ND-1000 spectrophotometer at 260 nm wavelength.

3.2.3.2. cDNA Synthesis and qPCR

For synthesis of complementary DNA (cDNA), I used the Maxima H Minus First Strand cDNA Synthesis Kit in accordance to the manufacturers instructions. I used 500 ng of RNA as input, whenever sample concentration permitted. Otherwise, I adjusted the input amount to match the lowest sample and used a minimum of 200 ng. When priming for a RT-qPCR of cellular targets or Protoparvovirus, I used random hexamer and oligo(dt) Primers. For Measles-specific priming, I used the primers as described **Table 7: Oligonucleotides**. After completion of cDNA synthesis, I treated the samples with RNAse H for 30 minutes at 37°C for digestion of RNA. For qPCR, I prepared a 20 µl reaction in triplicates per sample, containing 10 µl Power SYBR Green PCR Master Mix, 1 µl each of forward and reverse primer and 6 µl of sterile water. I then added 2 µl of the template cDNA. For the qPCR reaction, I used the Bio-Rad CFX96 Real-Time system at the indicated condition (**Table 11**). I extracted cycle threshold values (Ct) using the automated baseline

correction and threshold setting of the CFX Maestro software. I calculated $2^{-\Delta Ct}$ and $2^{-\Delta\Delta Ct}$, where applicable, using *ACTB* as reference gene.

Table 11: qPCR cycling conditions

	Temperature [°C]	**Time [s]**	**Ramp rate [°C/s]**	
Preincubation	95	15 mins	4.4	
Denaturation	95	15	1	40
Annealing	Ta	30	1	
Elongation	70	30	1	
Melting Curve Analysis	65-95		0.5	

3.2.3.3. Bulk RNA sequencing

For bulk RNA sequencing, I treated U251 cells as described above with 5 Gy irradiation and subsequent infection with MeV at MOI 0.1. Samples were harvested 48 h after completion of treatment. Three biological replicates were prepared and RNA was isolated as described above. I confirmed RNA quality and integrity using Qubit RNA IQ Assay. I diluted samples to 70 or 80 ng/µl, and handed them over to the DKFZ Next Generation Sequencing Core Facility (NGS CF) for library preparation and sequencing. Library preparation was performed following the TruSeq Stranded mRNA protocol (Illumina) and a NovaSeq 6000 on a S4 flow cell in a 100 bp paired-end mode. At least 100 Million reads were obtained per sample.

3.2.3.4. ELISA

To detect released CXCL10 and IFN-β in the supernatant of treated cells and spheroids, I performed enzyme-linked immunosorbent assays (ELISAs). I collected the medium of cells 48 h p.tr. and spheroids 72 h p.tr. and centrifuged it at 5000 g for 5 minutes at 4°C. I then aliquoted sample and froze them at -80°C until analysis. Each sample only underwent one freeze-thaw cycle.

ELISAs were performed in accordance with the manufacturer's protocol using half-well plates. Briefly, I coated plates by diluting the capture antibody in PBS at a ratio of 1:120 and added 50 µl of the solution to each well. I sealed the plate and incubated at room temperature over night. On the next day, I aspirated the coating solution and washed plates three times with 0.05 % Tween20 in PBS (wash step).I then blocked plates with 1 % BSA in PBS (sterile-filtered; reagent diluent) for at least one hour at room temperature. After three washes with washing buffer, I added 50 µl of standards and samples (supernatant of cells was diluted 1:20 or 1:100 for CXCL10 ELISA), sealed the plates and incubated over night at 4°C. On the next

day, I removed samples and standards, washed plates and added the detection antibody, diluted 1:60 in reagent diluent. After 2 hours of incubation at room temperature, I repeated the wash step and added 50 µl streptavidin-HRP diluted 1:40 in reagent diluent to each well. I incubated plates 20 minutes and performed a thorough wash step. I then added 60 µl TMB substrate solution and observed plates until a color reaction was visible in the lowest standard condition. I then added 30 µl stop solution and read the OD at 450 nm with reference reading at 570 nm using a spectrophotometer. To analyze data, I generated a standard curve from the OD measurements using a 4-parameter logistic curve fit with GraphPad Prism and then calculated the inferred concentration of the samples, taking the dilution factor into account.

3.2.3.5. Protein extraction, SDS-PAGE and Western Blot

When analyzing protein expression, I treated cells in accordance to the experimental setup as described above and harvested the cells at the specified time-point. I removed the supernatant and washed the wells once with cold PBS. I lysed the cells directly in the wells by adding RIPA buffer containing either Protease Inhibitor Cocktail cOmplete™ Ultra tablets or Halt™ Protease and Phosphatase Inhibitor Cocktail. The latter was used when protein extraction for analysis of phosphorylated EIF2α. I let the plates incubate on ice for 10 minutes and subsequently scraped the cells from the bottom of the well. I transferred the lysates to 1.5 ml Eppendorf cups and centrifuged them in a precooled centrifuge at 13.000 rpm for 10 minutes at 4°C. I stored them at -20°C until further analysis.

I quantified the protein content of each sample in 1:10 dilution using a bicinchoninic acid (BCA) protein assay, following the manufacturer's instruction. I measured the absorbance at 562 nm using a spectrophotometer and calculated the protein concentration for each sample. Then, I prepared equal amounts of protein by diluting the lysate in PBS as required and added 4x Laemmli Buffer. I boiled the samples at 95 °C for 5 minutes and loaded the denatured proteins onto a precast 4-20 % polyacrylamide gel. I separated the proteins by sodium dodecyl sulphate-polyacrylamide gel electrophoresis (SDS-PAGE) at 300 V for 35 minutes. I used the Precision Plus™ protein all blue standards as size marker. Once the separation was complete, I activated the gel in accordance to the manufacturer's instruction to allow for total protein quantification later on. To blot the proteins onto a polyvinylidene fluoride (PVDF), I used the Bio-Rad Trans-Blot turbo system as per manufacturer's protocol. Blotting was done with the preset mixed molecular weight settings. Once blotted, I visualized total protein using the ChemiDoc Imaging System and subsequently blocked the membrane for 1 h in blocking buffer (5 % milk powder in tris-buffered saline-tween (TBS-T)). I diluted primary antibodies in blocking buffer at the indicated dilution (**Table 6: Antibodies**) and incubated the membrane with the antibody overnight on an orbital shaker at 4°C. After washing the membrane 3x with 1x TBS-T for 10 minutes each, I added secondary horseradish-peroxiade

(HRP)-linked antibody diluted in blocking buffer for 1 h at room temperature, again placing the membrane on an orbital shaker. After three additional washes with 1x TBS-T for 10 minutes each, I performed chemiluminescent imaging by adding ECL substrate onto the membrane and recording the signal with the ChemiDoc Imaging System. In addition to the total protein quantification, I also reprobed the membrane for β-Actin: I washed the membrane again 3x 10 minutes with TBS-T and added the anti-β-Actin antibody conjugated to peroxidase in 5 % milk TBS-T. I incubated the membrane for 90 minutes at RT and performed three wash steps for 10 minutes with TBS-T thereafter. I again detected the chemiluminescent signal as described before. I quantified the Western Blot band intensities with FIJI software by measuring the mean band intensity of the target protein band against their background and normalizing to the respective measurement of the β-Actin band and background.

3.2.3.6. Immunofluorescence

As a marker of immunogenic cell death (ICD), I analyzed extracellular (ectopic) expression of calreticulin (CALR) via immunofluorescence staining. I seeded cells on cover slips (631-0125, VWR, Radnor, PA/USA) in 6-well plates. Twenty-four hours later, I initiated treatment as described above. I incubated plates for 48 h at 37°C with 5% CO_2. After the incubation period, I removed the medium from each well, washed twice with 1 ml D-PBS and fixed cells with 4 % PFA in D-PBS for 15 minutes. When the staining was not continued immediately, I added 3 ml D-PBS to each well and the space inbetween wells on the 6-well plate and sealed the plate with parafilm. I kept the plate in the fridge untl staining for a maximum of 2 days. I then washed three times and blocked cells with blocking buffer, containing 2 % BSA and 0.1 % Triton X-100 in D-PBS. I incubated plates for 60 minutes at RT. To stain cells, I diluted the primary antibody in antibody dilution buffer (0.1 % Triton X-100 and 1 % BSA in D-PBS) at the indicated dilution (**Table 6: Antibodies**). After another three wash steps with D-PBS, I added 30 µl of primary antibody to each well. I included a control without primary antibody to control for unspecific binding of the secondary antibody. I placed parafilm cut-outs of 2x2 cm on top of the cover slips to allow for optimal spread of the antibody solution across the cover slip. I then added D-PBS to the space between wells and elevated the lid with toothpicks to prevent draining during the incubation time. I incubated the cells with primary antibody solution over night at 4°C. I then removed the parafilm cut outs, washed the wells with D-PBS three times and added secondary antibody, again diluted in antibody dilution buffer, containing Hoechst at a 1:500 dilution. Again placing parafilm cut outs on top of cover slips, I incubated the plates for 90 minutes at RT in the dark. Subsequently, I removed the cut outs, washed three times with D-PBS and prepared the slides: Well by well, I added one drop of mouting media on top of a microscope slide and used forceps to place

the cover slip on the mounting media “face-down”. I removed air bubble by carefully shifting the cover slip. I let the media harden for ca. 2 h at RT and stored the slides in the fridge.

To acquire images, I used a Zeiss cell observer microscope of the core facility for light microscopy with a LED module Colibri.2 as a fluorescence source. To quantify the signal, I analyzed the images in FIJI. To this end, I performed grey scale transformation of the single-channel fluorescent images of the Hoechst and CALR channel. I measured CALR fluorescent intensity and counted nuclei in the Hoechst channel with the “Analyze Particles” function. I then normalized CALR intensity to nuclei count.

3.2.1. Use of large language models

I used ChatGPT (GPT-5, OpenAI) for text refinement. No conceptualization, experimental design, data analysis (except for R code trouble shooting, see section below) or figure generation was performed with artificial intelligence. I wrote all text passages of this thesis myself. If ChatGPT was employed, I used them as input for minor text refinement and rephrasing. No text passages of this thesis were generated *de novo* by ChatGPT or other large language models.

3.2.2. Statistical Analysis

I visualized and analyzed data using GraphPad Prism 10.5.0. Depending on the experimental setting, I used one-way or two-way ANOVA, adjusted for multiple comparison testing using Tukey’s.multiple comparison post-hoc test. I set alpha to 0.05 and report on multiplicity-adjusted p-values. For visual clarity, I only depict the most relevant comparisons in the graphs using one star for all p-values indicating significance (*). Additional significances may be reported either in the text or supplementary figures, where indicated.

3.2.3. Analysis of RNA sequencing data

Initial data processing was performed by the Omics-IT and Data Management CF following their One Touch Pipeline.[145] Reads were aligned to the human genome (build 37, version hs37d5) and feature count data was provided. I performed subsequent analysis using R with RStudio using the EdgeR package and following the suggested workflow.[146,147] Marie Szczeponik contributed to the R script. I visualized the results of MDS, GO analysis and DEGs in volcano plots with the R package ggplot2 (v3.3.3).[148] Pheatmap was used to generate heatmaps (version 1.0.13). I performed gene set enrichment analysis with GSEA v4.4.0 with the Molecular Signature Databases (MSigDB) “Hallmark” gene set collection.[149,150] I used ChatGPT (GPT-5, OpenAI)to troubleshoot code errors and refine graph aesthetics.

4. Results

Previous work conducted in our group showed synergy when combing radio- and virotherapy. While combination treatment did not alter radiosensitivity or virus replication, it did enhance cytotoxicity *in vitro* and showed increased immune induction *in vitro* and *in vivo*.[135] Building on this, I aimed to modify the combination regimen to further boost the observed synergy.

4.1. Transcriptomic analysis reveals enhanced immune induction of radiovirotherapy

To comprehensively analyze the combination of measles virus (MeV) and radiotherapy and deduct mechanisms of action that could be exploited to rationally modify and improve it, I conducted a bulk RNA sequencing experiment: I isolated RNA from combination-, mono-, and untreated cells. Library preparation and RNA sequencing was performed by the NGS core facility of the DKFZ. The Omics IT and Data Management Core Facility performed initial data processing, providing feature counts data for each sample. I conducted further analysis using the edgeR package in R with Rstudio.

For quality control of the data and to assess similarity of replicates or treatment groups, I conducted a multidimensional scaling (MDS) analysis (**Figure 4-1 A**). The replicates of each treatment group clustered together, while untreated and combination-treated samples, as well as mono therapy groups showed maximal distance in dimension 1 or 2, respectively. Thus, the global transcriptional patterns induced by each treatment seem to be distinct and reproducible.

Next, I assessed differentially expressed genes (DEGs) in pairwise comparisons. The volcano plots (**Figure 4-1 B**) show up- or downregulated genes between all treatment groups individually. While all treatments and comparisons show altered transcript levels to some degree, the number of differentially expressed genes varies. Virus treatment predominantly induced gene expression: The number of downregulated genes is comparatively low with 6 when comparing combination to radiotherapy (reflecting the changes attributable to the addition of virotherapy) and 36 in the comparison to mock. Irradiation on the other hand not only induces the expression of more genes (377 vs. 232 in the mock-comparisons), but also leads to the downregulation of a higher number of genes (221 in radio versus mock and 154 in combi versus virus). In line with the MDS analysis, the genes influenced by the respective treatment seem to be distinct between radio- and virotherapy: The combination shows the highest number of DEGs (683 upregulated and 295 downregulated in the mock comparison), even exceeding the addition of virus- or radiotherapy influenced genes. This indicates minimal overlap between the DEGs in either monotherapy group.

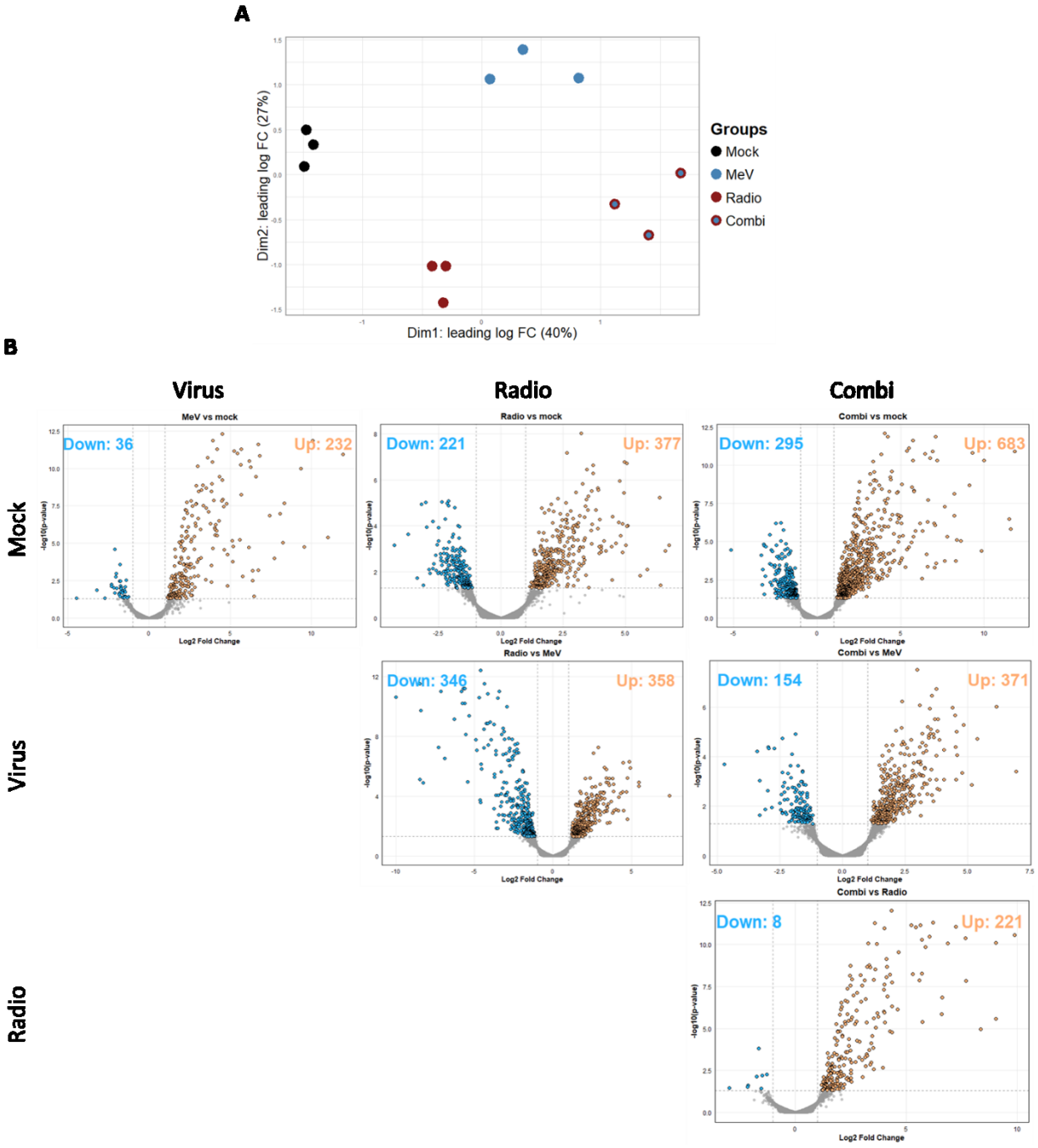

Figure 4-1: RNA sequencing of RVTx-treated cells reveals altered transcriptional patterns

I irradiated U251 cells at 5 Gy and infected 24 h thereafter with MeV (MOI 0.1). I harvested cell pellets 48 h p.tr. and isolated total RNA. Bulk RNA sequencing was performed using NovaSeq 6000 S4 (paired end; 100bp reads). (A) MDS analysis was performed for the individual replicates of each treatment group (B) Volcano plots show DEGs comparing all treatment groups. Significantly up- (orange) and down- (blue) regulated genes are marked and their number given. Thresholds: logFC -1 or 1; p-value 0.05

After this analysis of global transcript patterns, I investigated which transcripts specifically show the most differential expression in the combination treatment. To this end, I focused on the top 50 DEGs in the comparison of RVTx- to mock-treated samples and analyzed their expression across all treatment groups

(**Figure 4-2**). Euclidian clustering was applied for both sample groups (columns) and genes (rows). For the top 50 DEGs, I saw a pattern aligning with the conclusions of the MDS and volcano plot analysis: Replicates clustered together and both radiotherapy and virotherapy contributed to the gene expression of the combination-treated group, thus clustering between the two monotherapy groups. Only one transcript (RP11-496D24.2) among the 50 was downregulated in the combination, the other 49 showed increased transcript levels. Among the upregulated genes in the combination-treated samples, three distinct subgroups were defined: One driven by virus treatment (33 genes), one driven by irradiation (9 genes) and a third where gene expression was comparably low in both monotherapies (7 genes). A majority of the genes upregulated in the combination in a virus-driven manner were ISGs (members of OAS and IFIT family as well as *ISG15, MX2, DDX58, ZBP1* etc). Among the upregulated genes influenced by irradiation were also immune-related genes such as cytokines (*IL8* and *CCL20*), but also a more diverse set of genes including some related to ECM architecture (*COL5A3*), tissue remodeling (*KRT75*) and the complement system (*F13A1*). Lastly, the third subgroup entails genes associated with inflammation (*SAA1* and *SAA2*), cytokines (*CCL8* and *CSF2*) and immune suppression (*IL1RN, NT5E*). Notably, when I sorted the list by FDR, most DEGs had a MeV-driven differential expression (**Figure 7-1**).

Overall, analysis of the top 50 DEGs reveals strong immune induction in the combination treatment, influenced by both treatment modalities individually. Possibly, this enhanced immune induction in turn induces negative feedback loops and upregulation of immune suppressors specifically in the combination treated condition.

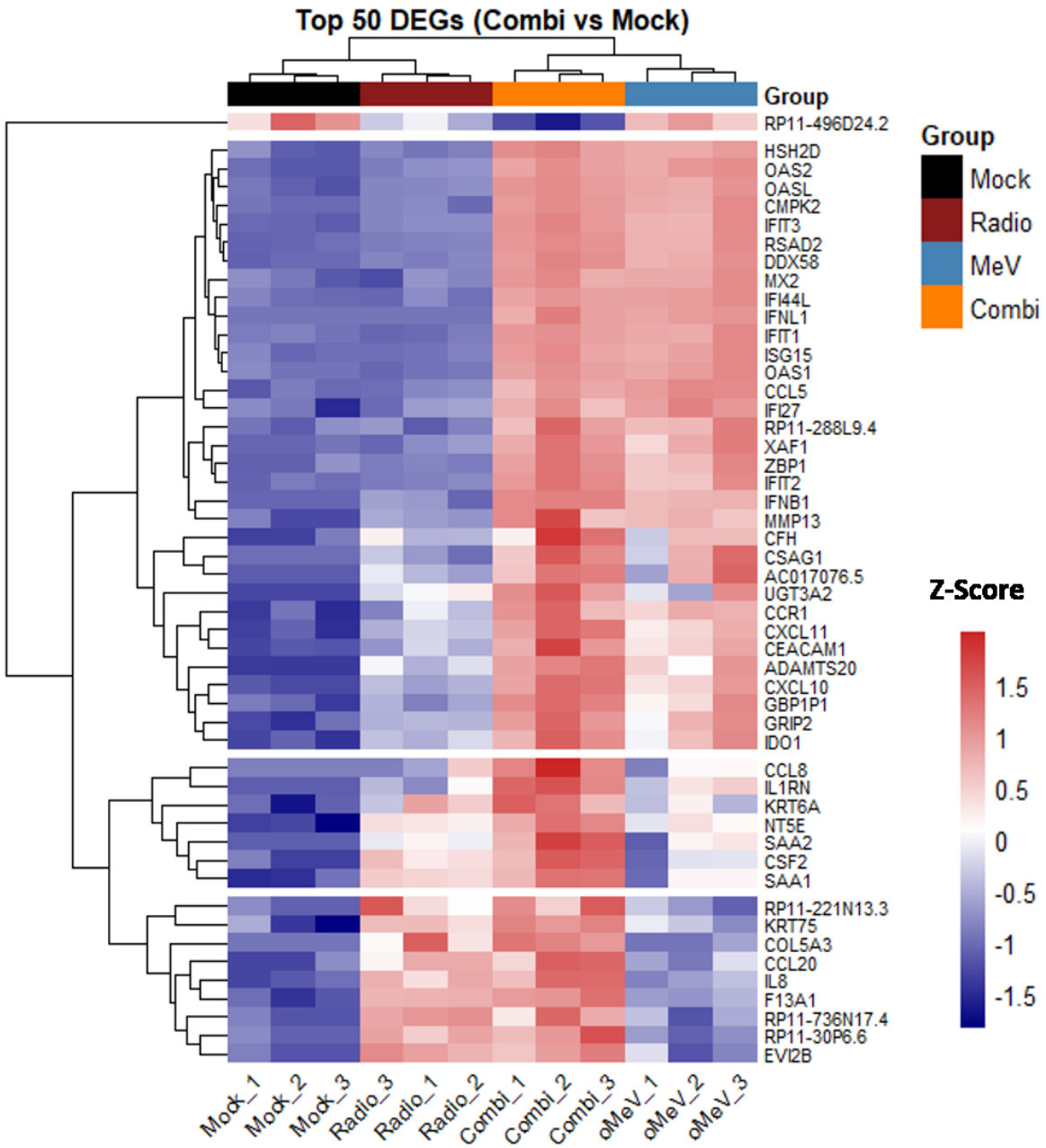

Figure 4-2: Top 50 DEGs of the RVTx-treated sample are mostly immune-related

I treated and prepared samples as described in the legend to Figure 4-1. The heatmap shows Z-Score normalized expression of the top 50 DEGs of the combination versus mock comparison for all samples. I selected the top 50 DEGs based on logFC values among significant (FDR < 0.05) differentially expressed |logFC| > 1) genes. I applied Euclidian clustering across rows (genes) and columns (samples).

For a comprehensive analysis of the functional consequence of the observed transcriptional changes, I performed Gene Ontology (GO) term and gene set enrichment (GSE) analysis (**Figure 4-3**).

GO term analysis among the DEGs in combination versus mock-treatment, exclusively found terms related to viral infection and innate immunity among the top 20 (**Figure 7-3**). To get a broader understanding of the underlying mechanisms, I additionally compared combination to the MeV-treated condition to deduct the impact of the addition of irradiation (**Figure 4-3 A and B**). Still, the majority of enriched GO terms remains related to immune signaling in this comparison. The terms are not directly entailing antiviral

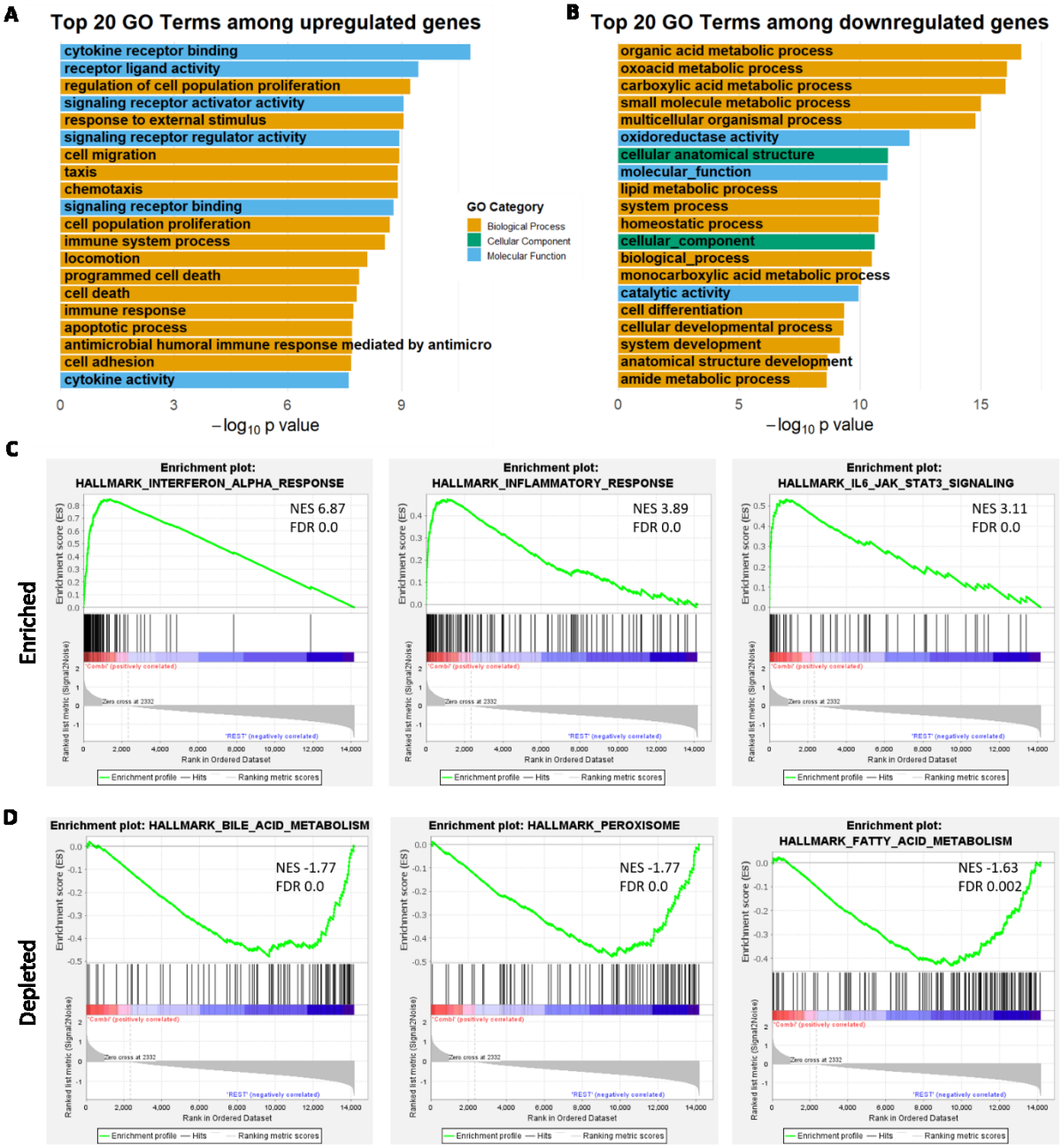

Figure 4-3: Immune pathways are strongly upregulated in RVTx treated cells

I treated and prepared samples as described in the legend to Figure 4-1. Top 20 GO terms by p value that are (A) up- or (B) downregulated in combination vs. versus virus comparison. Top (C) and bottom (D) three hallmark gene sets of of the GSEA analysis comparing the combination to the three other treatment groups. GO - Gene ontology; NES - Normalized Enrichement Score; FDR - False Discovery Rate (q value)

response, but broad categories such as “cytokine receptor binding” or “immune system response”. Additionally, more general cell signaling and proliferation processes as well as GO terms related to cell death were enriched in this DEG comparison (“cell migration”, “regulation of cell population proliferation”, “programmed cell death”, “cell death”, “apoptotic process”). Of the GO terms that were enriched among the downregulated genes, the majority were related to metabolic processes and pathways (“organic metabolic pathways”, “carboxylic acid metabolic process”). This could indicate a stress response and resulting metabolic shutdown.

For GSEA, I compared the gene expression of combination-treated samples to all other groups and tested the enrichment of the “Hallmark” gene sets provided in the MSigDB (**Figure 4-3 C** and **D**). I found three hallmark pathways to be highly enriched and sharing a FDR of 0.0. All three were indicative of activation of the innate immune system: “Interferon alpha response” (NES 6.87), “inflammatory response” (NES 3.89) and “IL6 JAK STAT3 pathway” (NES 3.11). The three most enriched hallmark gene sets in the other treatment groups (and therefore depleted in the combination) were metabolic pathways (“bile acid metabolism” (NES -1.77, FDR 0.0), “peroxisome” (NES -1.77, FDR 0.0) and “fatty acid metabolism” (NES -1.63, FDR 0.002)).

Thus, both GO term analysis and GSEA revealed a very similar pattern: The combination treatment induced innate immune signaling to a greater extent than either monotherapy and metabolic processes were reduced, possibly due to stress response and apoptotic signaling.

All in all, both monotherapies seem to contribute to the transcriptional alterations that are apparent in the combination treatment. The RNA sequencing results are in line with the previously established mechanism of action of RVTx: Increased (innate) immune induction and higher levels (immunogenic) cell death occur in combination-treated cells. Especially the enhanced induction of innate immunity might be a double edged sword in the RVTx setting: While IFN-signaling is known to enhance induction of the adaptive immune system and is necessary to drive the tumor microenvironment to a more immunonogenic phenotype, it also interferes with viral replication and might hamper replication and spread of the highly IFN sensitive MeV. This underlines the potential of modifying the combination regimen to control the timing of the IFN response for optimized efficacy.

This solidified our hypothesis: Transient, tumor-cell specific reduction of IFN signaling through *Protoparvovirus* might increase MeV replication and spread and ultimately yield higher treatment efficacy. To study this hypothesis *in vitro*, cell lines capable of mounting an IFN response were required.

4.2. Identification of candidate cell lines for the assessment of triple radiovirotherapy

To choose candidate cell lines for testing our hypothesis of the triple radiovirotherapy approach, I performed an initial screen in a panel of GBM (U87, U251, U373) and PDAC (BxPC-3, T3M4) cell lines with the goal to identify one cell line per entity. To this end, I analyzed baseline and induced levels of *IFNB1* on transcript level. Additionally, I analyzed a selection of ISGs on transcript and protein level to confirm intact downstream signaling. Finally, I investigated variation in MeV permissiveness of the cell lines through multi-step growth curves and assessed the effect of IFN-β pretreatment on MeV replication by quantification of genomes through RT-qPCR

4.2.1. Levels of intrinsic IFN signaling vary between cell lines

4.2.1.1. Baseline and induced levels of IFNB1 and ISGs on transcript level

To compare cell lines in their intrinsic ability to mount an IFN response, I treated cells with MeV and the known IFN-inducer Poly(IC), a synthetic double-stranded RNA.[151,152] I performed RT-qPCRs for *IFNB1* and selected ISGs (**Figure 4-4**)

Baseline, non-induced, levels of *IFNB1* transcripts differed in a 200-fold range between U87 (lowest) and T3M4 (highest), but the differences did not reach statistical significance (**Figure 4-4 A**). Induced levels of *IFNB1* varied in regard to stimulus and intensity: At the time point investigated, Poly(IC) treatment resulted in an 30-fold increased IFNB1 expression only for U251 cells. All other cell lines showed a limited induction of no more than 4-fold. This was independent of the concentration of Poly(IC) applied and the differences between cell lines were not statistically significant. On the other hand, all cell lines showed an increase in *IFNB1* transcripts in response to MeV infection. This ranged from 80-fold for U87 to 6000-fold for U251.

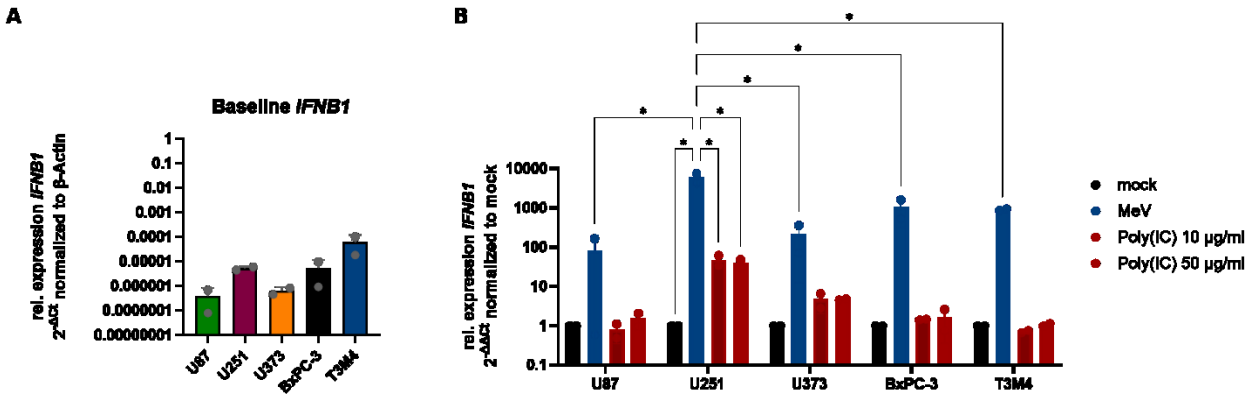

Figure 4-4: Cell lines vary in their intrinsic capacity to induce IFNB1transcript levels.

I isolated RNA 48 h after treating cells with either 10 or 50 µg/ml Poly(IC) or MeV. RT-qPCR analysis compared levels of *IFNB1* transcripts. (A) $2^{-\Delta CT}$, normalized to *ACTB*, values are depicted for untreated samples of the cell line panel to show baseline *IFNB1* levels. (B) Fold changes of *IFNB1* levels compared to untreated samples in response to the respective treatment. Mean and standard deviation of two independent experiments are shown * - p< <0.000001

However, the increase compared to mock- or Poly(IC)-treatment only reached significance in U251 cells. Equally, the induction of *IFNB1* in response to MeV was significantly increased in U251, compared to all other cell lines (**Figure 4-4 B**).

Since the concentration of Poly(IC) did not affect induction levels, I used 10 µg/ml in all subsequent experiments.

Next, I analyzed transcript levels of a selection of ISGs to observe whether the cell lines were able to induce downstream signaling upon the IFN stimulus. Targets included *EIF2AK2* (PKR), *IFITM1* and *ISG15* and were analyzed by RT-qPCR (**Figure 4-5**).

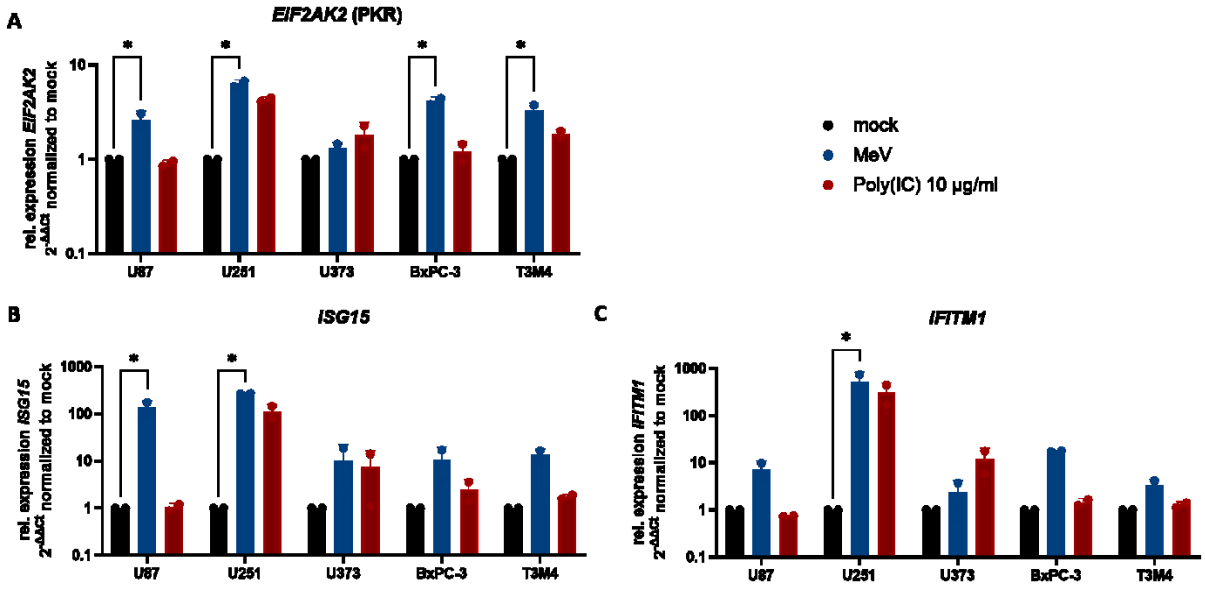

Figure 4-5: Cell lines vary in their intrinsic capacity to induce ISG signaling

I isolated RNA 48 h after treating cells with either 10 µg/ml Poly(IC) or MeV. Through RT-qPCR analysis, I compared levels of (A) *EIFAK2*, (B) *ISG15* and (C) *IFITM1* transcripts. $2^{-\Delta\Delta CT}$ values, normalized to *ACTB* and mock-treated controls, in response to the respective treatment are depicted. Mean and standard deviation of two independent experiments is shown. * - $p<0.05$; Statistical significance was assessed for all group comparisons; only selected combinations are shown in the figure for clarity.

All cell lines showed a trend towards increased levels of the target transcripts upon MeV infection. The range of induction was different for each target: *IFITM1* showed highest induction levels ranging from 2- to 530-fold, *ISG 15* showed a 10- to 270-fold increase and *EIF2AK2* levels were 1.5 to 6-fold induced. While MeV-mediated induction of *EIFAK2* was significant for 4 out of 5 cell lines, induction of *ISG15* and *IFITM1* was significant for two and one cell line only, respectively. The only cell line that showed significant induction for all ISG targets assessed was U251. Equally, the relative expression after MeV infection was

highest in U251 for all targets, when compared to the other cell lines (all significances are shown in **Figure 7-2**).

Similar to *IFNB1*, ISG transcript levels were less elevated in response to Poly(IC). Compared to mock, only U251 cells had significantly higher expression levels. Interestingly, U373 showed a different (albeit non-significant) pattern: Here, Poly(IC) treatment induced a similar or higher fold change of target transcripts compared to MeV infection.

In summary, the tested cell lines showed different induction patterns of the transcript levels of *IFNB1* and selected ISGs: While all cell lines showed at least 80-fold induction of *IFNB1,* induction of ISGs was more variable. Only U251 cells showed robust and significant induction of IFN signaling in response to the applied stimuli, especially MeV.

Finally, I wanted to compare the induction pattern of IFNB1 and ISGs side by side for each cell line. Since MeV is the IFN stimulus in the RVTx setting, I focused on the transcript levels in response to MeV. I log-transformed and normalized the expression levels of each target and generated a heat map (**Figure 4-6**). Clearly, U251 has the highest expression level across all targets in response to MeV, making it a good candidate for GBM to evaluate intact IFN signaling in the RVTx setting. For PDAC, the difference between cell lines was less pronounced. Both cell line showed similar, intermediate induction of *IFNB1*. BxPC-3 had slightly higher induction levels of EIF2AK2 and IFITM1.

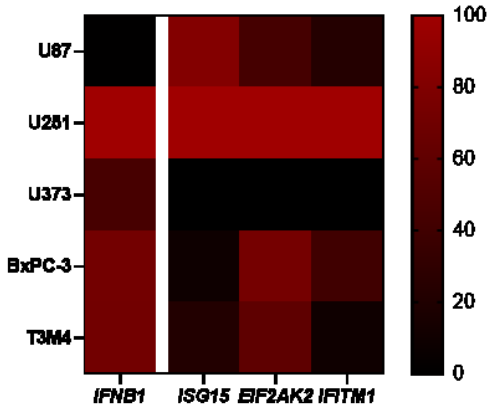

Figure 4-6: Overview of MeV-mediated signaling induction on transcript level

To integrate the data gathered on the transcript level, I log-transformed and normalized the expression levels of each target in response to MeV across the cell lines tested. The highest fold change for each target is set to 100 %, the lowest to 0 %. The heat map depicts the percentages for IFNB1, ISG15 EIF2AK2 and IFITM1 across the five cell lines.

4.2.1.1. Baseline and induced levels of ISGs on protein level

Next, I tested whether these pattern were also present on the protein level. To this end, I performed SDS-PAGE and Western Blot analysis of two ISGs, STAT1 and ISG15 (**Figure 4-7)**.

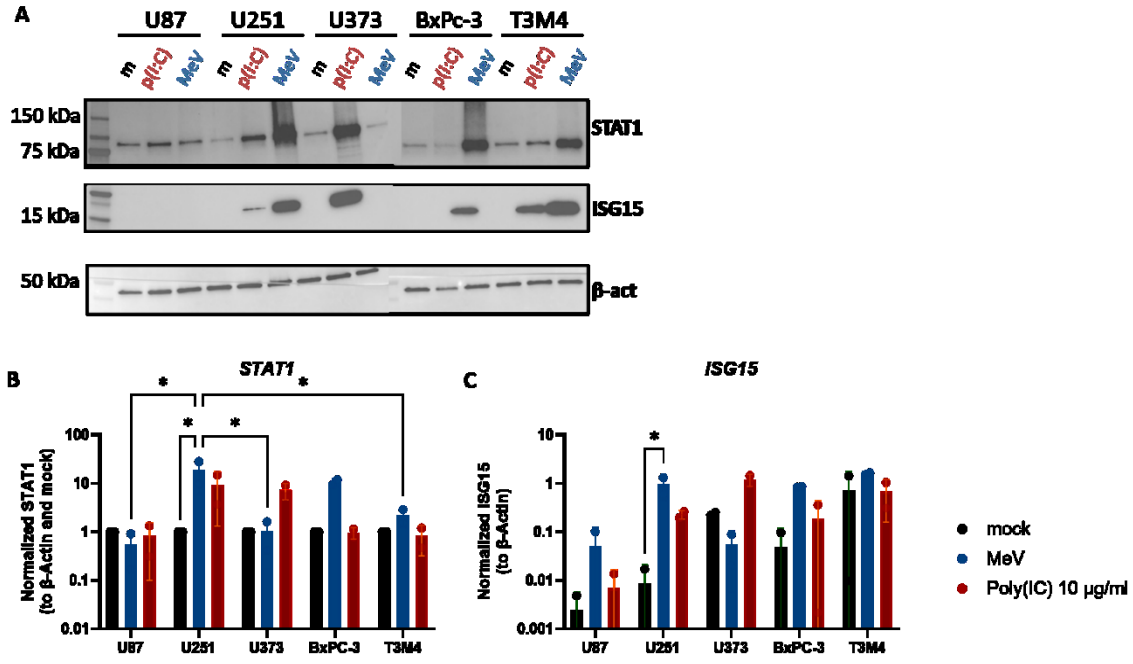

Figure 4-7 Western Blot analysis confirms differences in ISG induction between cell lines

I treated cell lines with MeV at MOI 0.1 or 10 µg/ml poly(I:C) and collected cell lysates 48 h p.tr.. I performed SDS-PAGE and Western Blot of and detected STAT1 and ISG15 on the membrane. β-Actin served as loading control. One representative Western Blot is shown (A). I quantified band intensities for STAT1 (B) and ISG15 (C), normalizing to β-Actin and mock-treated cells, where possible. Mean and standard deviation of two replicates are shown. Two-way ANOVA with Tukey's multiple comparisons test was used; * - $p < 0.05$

Both STAT1 and ISG15 showed similar induction patterns: I observed an increase of both targets in U251, BxPc-3 and T3M4 cells in response to MeV. U251 and T3M4 cells also showed increased levels of the targets in response to poly(IC). U87 showed no induction of either ISG in response to either stimulus and, similar to the transcript level, U373 showed a stronger induction in response to poly(IC) than MeV treatment.

To quantify the protein levels, I analyzed the band intensities using FIJI software. I measured mean grey intensities of bands versus background and normalized the data: STAT1 is also detected in mock-treated samples, so I normalized to both loading control and the uninduced state. Non-induced levels of ISG15 were not reproducibly detectable for any of the targets. Thus, I could only normalize protein levels to the loading control β-Actin. (**Figure 4-7 B and C**). Overall, the quantification was in line with the previous observations. Again, only MeV-driven induction in U251 cells was statistically significant for both targets.

For STAT1, this increase was significantly higher in U251 cells than in all others, except BxPC-3, where the difference did not reach significance.

All in all, the induction of ISG on the protein level was comparable to what I had observed on the transcript level. All cell lines showed some intrinsic IFN signaling in response to either poly(IC) or MeV. Nevertheless, U251 clearly showed highest levels of IFN signaling on both transcript and protein level.

Markedly, U373 showed a different pattern than all other cell lines and reproducibly mainly induced ISGs in response to poly(IC). Poly(IC) and MeV are sensed by different nucleic acid sensors inside the cell, which led me to the hypothesis that U373 might have different levels of certain pattern recognition receptors (PRR). Thus, I compared baseline and induced levels of TLR3 (sensing poly(IC)) and RIG-I (sensing MeV) between U373 and BxPc-3 cells (**Figure 7-4**). In contrast to the hypothesis, BxPC-3 showed higher levels of both PRRs at baseline. *DDX58* levels were higher than TLR3 levels in U373 (**Figure 7-4 A**). And while, again, treatment with poly(IC) elicited a higher fold change for the targets in U373 cells, the pattern was very similar between *TLR3* and *DDX58*. I observed the strongest induction at the 12 h timepoint and subsequent reduction of the Poly(IC)-induced fold change. Equally in BxPC-3, Poly(IC) induced higher levels for both PRRs at the 12 h timepoint. However, for the other three timepoints MeV elicited the stronger induction in that cell line. All in all, no difference in the baseline or induced states of TLR3 or DDX58 can be observed between the cell lines. Transcript levels of the PRRs seem to be independent of the different response to the two stimuli.

4.2.2. Levels of intrinsic IFN signaling influence susceptibility to MeV infection

Having thoroughly analyzed the ability to induce IFN signaling, I analyzed the consequence for permissiveness to MeV. I microscopically observed differences in infection patterns and performed multi-step growth curves to observe viral replication kinetics by quantifying infectious viral (progeny) particles at certain time points after infection (**Figure 4-8**).

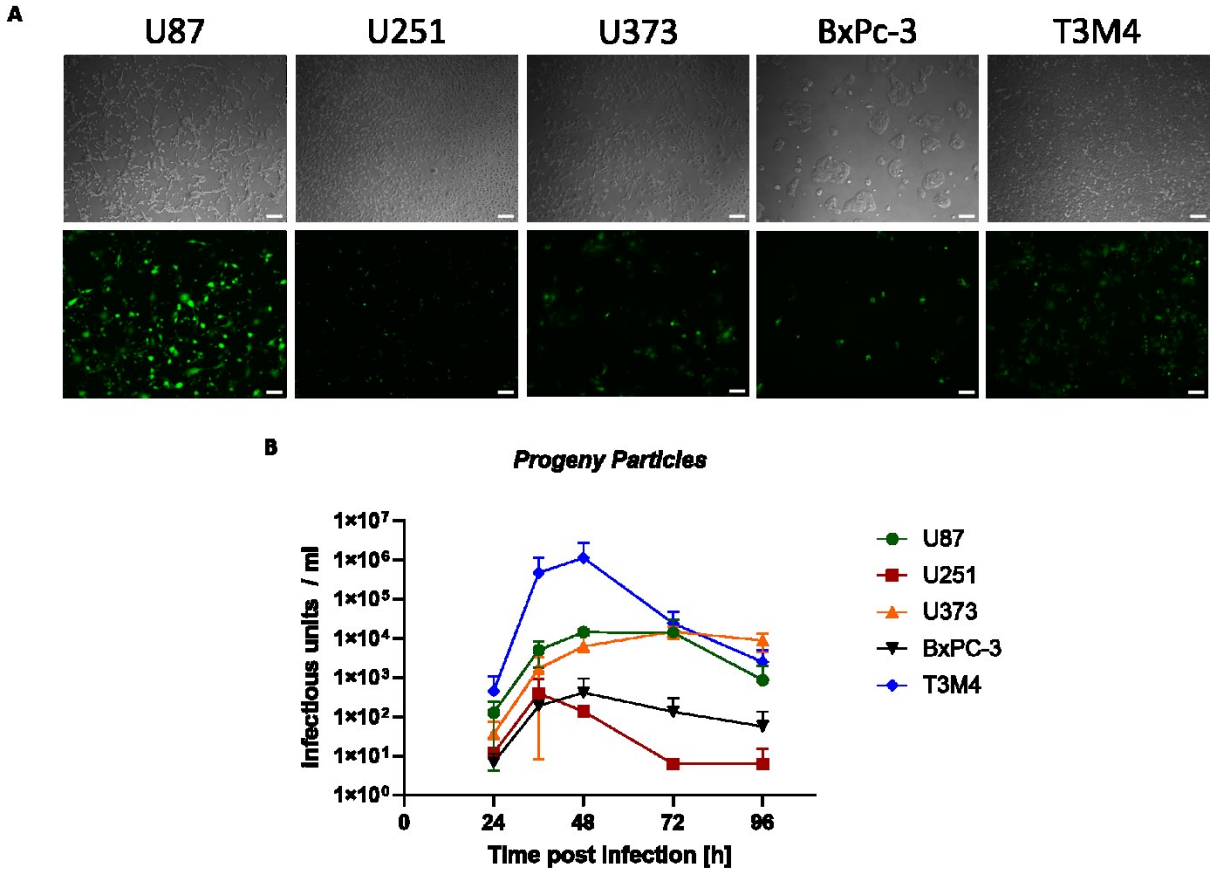

Figure 4-8: MeV permissiveness in candidate cell lines

(A) I observed cell morphology (phase contrast) and eGFP expression (fluorescence microscopy) after infection with MeV at MOI 0.03. Time point 48 h p.i. is shown. 5x objective, scale bar: 200 µm. (B) I infected candidate cell lines with MeV ld eGFP at an MOI of 0.03. 24, 36, 48, 72 and 96 h p.i,. I harvested samples and performed subsequent serial dilution titration assays

When I observed cells infected with MeV at MOI 0.03 microscopically, I saw differences in infection pattern and MeV-encoded eGFP expression: By far, infection was most widespread and eGFP signal strongest in U87 cells. eGFP signal was very weak in U251 cells, the other three cell lines showed intermediate eGFP expression. While U87 morphology does not allow for formation of large syncytia structures, the cell membrane appeared very tense and some multi-nucleated structures are observable. U373 and T3M4 cells both show formation of characteristic syncytia. In U251 and BxPC-3 cells, on the other hand, mostly single cells show eGFP expression and most cells retain their individual membrane structure.

In the multi-step growth curves, results were mostly in line with these observations: U251 gave rise to the least amount of progeny particles and the concentration dropped early at the 48 h time point. BxPC-3 also showed limited permissiveness to MeV infection, both cell lines had a maximum progeny virus titer of around 500 ciu/ml. T3M4 showed a 4-log higher peak of infectious units, possibly due to the formation of larger syncytia in that cell line (phase image T3M4 in **Figure 4-8 A**). U87 and U373 showed intermediate progeny virus titers, peaking at around 0.5-1*10^4 ciu/ml and progeny production was sustained longer compared to BxPC-3 and U251.

Additionally, I tested the effect of pretreatment with IFN-β on MeV replication. To this end, I treated cells with 10 ng/ml IFN-β and infected 16 h later with MeV at MOI 0.1. I quantified viral genomes by RT-qPCR (**Figure 4-9**).

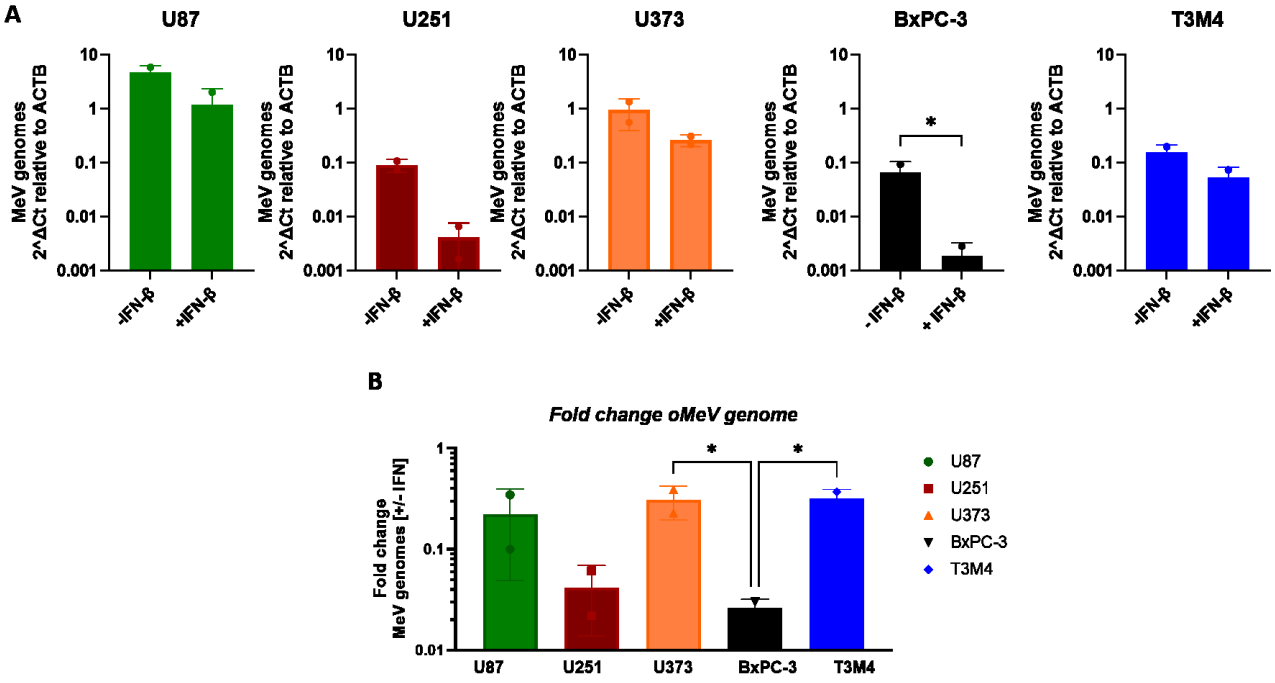

Figure 4-9: Effect of IFN-β pretreatment on MeV replication in cell line panel

I seeded cells and pretreated with 10 ng/ml recombinant IFN-β 16 h prior to infection with an MOI of 0.1. I harvested cells 48 h after and isolated RNA. MeV genomes were quantified by RT-qPCR. *: $p < 0.05$ (ratio paired t test) (A) $2^{-\Delta Ct}$ values of MeV genomes, normalized to ACTB are shown with and without pretreatment with IFN-β. (B) Foldchanges of data depicted in (A); *: $p < 0.05$ (one-way ANOVA with Tukey's multiple comparisons test)

For all cell lines, pretreatment with IFN-β resulted in a decrease of viral genomes (**Figure 4-9 A**). The difference was larger for U251 and BxPC-3 cells and only reached significance for the latter (p=0.0265). Equally, comparing the fold changes of MeV genomes in pretreated over non-pretreated cells between the cell lines showed that IFN-β had the largest effect on meV replication in U251 and BxPC-3 cells (**Figure**

4-9 B). Again, only BxPC-3 cells showed a significant reduction and only in comparison to U373 and T3M4 cells.

All in all, the comprehensive analysis of the the cell line panel revealed differences in their capacity to induce IFN signaling: Among GBM cells, U251 showed the highest increase in *IFNB1* on transcript level and ISG on transcript and protein level. The cell line was also less permissive to MeV infection and showed a strong (albeit non-significant) effect of IFN-β pretreatment on MeV replication. In terms of IFN signaling induction, the picture was less clear for the PDAC cell lines tested. Both showed an intermediate induction of the tested target transcript and proteins. However, BxPC-3 was less permissive to MeV and showed a significant reduction of MeV replication when pretreated with IFN-β. Thus, the following experiments of evaluating the effect of a transient IFN dampening on the radiovirotherapy treatment regimen was carried out in U251 and BxPC-3 cells.

Lastly, I investigated whether replication of MeV was required to elicit the strong IFN response. To this end, I used ERDRP-0519, an inhibitor of Measles Virus interfering with the viral RNA-dependent RNA polymerase. When the inhibitor is applied, the virus can enter the cells, but transcription and replication is inhibited. I measured the transcript levels of *IFNB1* after MeV infection in presence or absence of ERDRP-0519 by RT-qPCR (**Figure 7-5**). As expected, the inhibitor itself elicited no increase in *IFNB1* levels. MeV infection, on the other hand, yielded a significant increase. Strikingly, treatment with the MeV polymerase inhibitor resulted in a significant decrease of 10- (U251) or 100-fold (BxPC-3) of *IFNB1* transcripts. This clearly indicates that presence of MeV genomes is not sufficient to trigger an IFN response, but replication and/or transcription is required to drive a strong IFN response.

4.3. Dual virotherapy: Analysis of cytotoxicity and underlying signaling

To investigate the effect of the addition of Protoparvovirus (PV) to the RVTx treatment regimen, I initially tested the combination of the two viruses to optimize the dosing. Since the rational of combining these oncolytic vectors was the IFN-dampening effect of PV, I applied PV 24 h before MeV to allow for sufficient expression of viral proteins to elicit their effect.

4.3.1. Limited cytotoxic effects of dual virotherapy

To analyze the cytotoxic effect on the two cell lines, I performed XTT assays (**Figure 4-10**). I measured the metabolic activity of the cells on day 5 and day 7 p.tr..

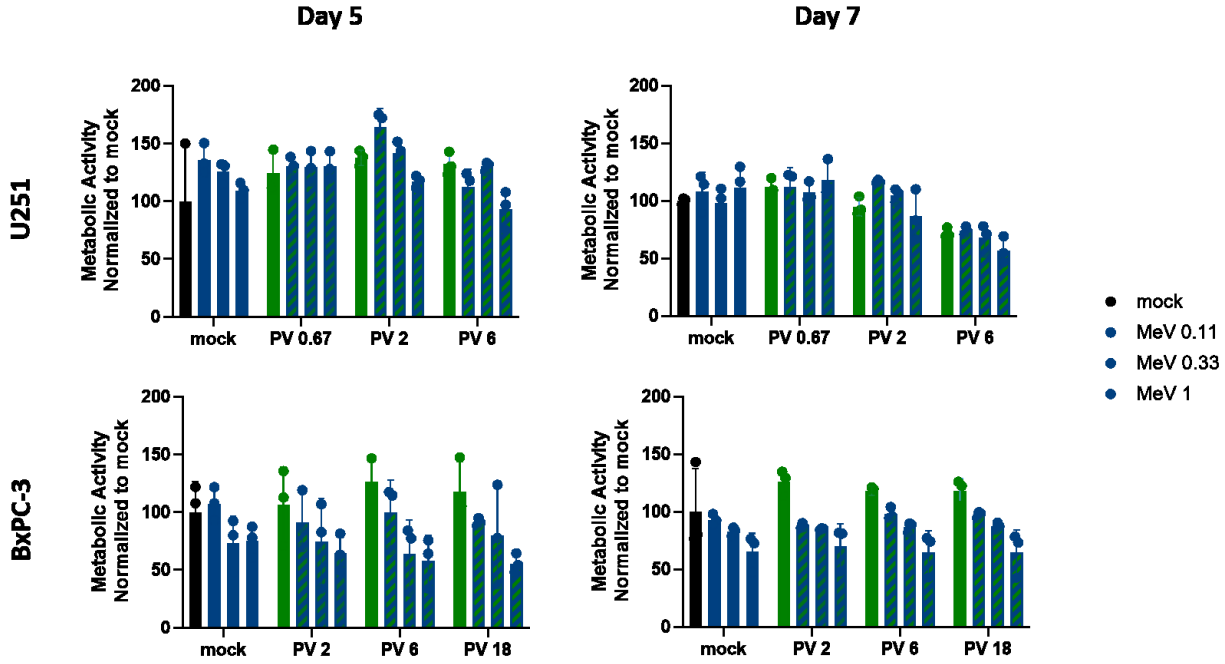

Figure 4-10: Cell viability after dual virotherapy in U251 and BxPC-3 cells

I assessed cytotoxic effects of the treatment with PV and MeV by XTT assay. I infected cells with PV and 24 h thereafter with MeV. MOIs of each virus are indicated. On day 5 and 7 p.tr., I analyzed the metabolic activity of the cells. Data is normalized to the average of the mock-treated samples for each time point. N=3 technical replicates.

The treatment effect differed between the cell lines: On day 5, cytotoxic effects were very limited in U251 cells. Only the combination of the highest PV and MeV dose (MOI of 6 and 1, respectively) showed a reduction of metabolic activity, compared to mock. On day 7, overall cytotoxicity remained low, but a PV-dependent decrease in viability was observable. An MOI of 6 for PV reduced viability to 76 %. With the highest MOI of 1 for MeV this was further reduced to 54 %. All other dose combinations only reduced viability to approximately 90 %. MeV alone had no effect on U251 cells at either time point. On the contrary, only MeV as a monotherapy elicited a cytotoxic effect on BxPC-3 cells for both time points. Here, I observed dose-dependent reduction in metabolic activity to 65 % or 75 % on day 5 and day 7, respectively, for the highest MOI of MeV. Treatment with PV did not greatly enhance the cytotoxicity. The combination of the highest doses of the viruses showed an additional 10 % reduction on both days. PV alone increased the metabolic activity of the cells for all MOIs. I tested the dual virotherapy approach with a variety of dose combinations and repeatedly saw the pattern shown and described here (data not shown)

All in all, only a limited combined effect in terms of cytotoxicity was measurable. While the highest dose-combination did yield the greatest effect for all cell lines and time points, this was only a marginal increase compared to the effect of monotherapy with one virus. Interestingly, the cell lines showed different sensitivities to the viruses: U251 was more sensitive to PV treatment, BxPC-3 to MeV treatment.

4.3.2. Transient synergy of dual virotherapy

In addition to evaluating the cytotoxic effect of the dual virotherapy, I analyzed the synergy of the two viruses in the cell lines tested. To this end, I used the web application of SynergyFinderPlus. As input, I combined the cytotoxicity data of all virus dose combinations I tested and used the ZIP model for synergy calculation (**Figure 4-11**).

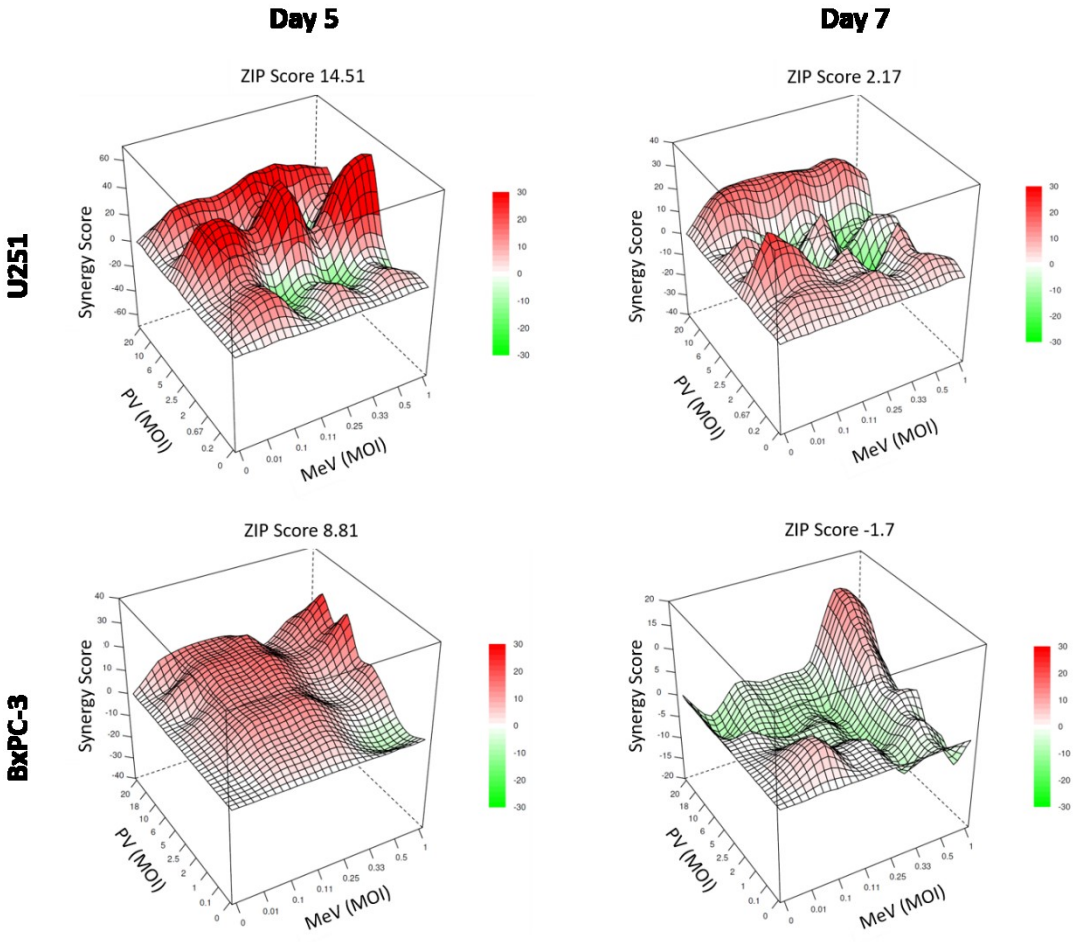

Figure 4-11: Synergy analysis of dual virotherapy in U251 and BxPC-3 cells

Using the SynergyFinderPlus web application, I analyzed the cytotoxicity data for synergy between the two viruses. 3D plots of synergy scores based on the ZIP synergy model are depicted for all dose combination of PV and MeV that I investigated. Analysis was undertaken separately for U251 and BxPC-3 and for day 5 and day 7. ZIP scores around 0 (white) indicate an additive effect, negative values (green) antagonism and positive values (red) synergy.

I observed higher synergy scores for both cell lines at day 5, with ZIP scores of 8.81 (BxPC-3) and 17.31 (U251), suggesting synergistic interaction between the viruses at this time point. By day 7, however, ZIP scores had decreased or even turned negative, indicating additive or antagonistic effects and thus a transient pattern of synergy. Given the very limited cytotoxicity observed at the earlier time point, these synergy scores should be interpreted with caution, particularly regarding their biological relevance. For a combination therapy to be considered effective, both sensitivity (cytotoxic impact) and synergy are required—a prerequisite not fulfilled in the case of the dual virotherapy tested here..

In addition to the schedule used above where I added PV 24 h prior to MeV infection, I also tested the simultaneous application of the two viruses (**Figure 7-6**). The pattern I observed was similar to the schedule used above: BxPC-3 cells were mostly sensitive to MeV, U251 to PV infection. Equally in the synergy analysis, I observed high synergy scores at the early timepoints and additive or slightly antagonistic synergy scores for the later time point.

4.3.3. Mechanistic analysis of dual virotherapy

The hypothesis underlying the dual virotherapy approach was the transient IFN dampening by PV and subsequent increase in replication of the IFN-sensitive MeV. I thus investigated the effect of dual virotherapy on *IFNB1* transcripts and ISG and effector *CXCL10* as well as MeV replication via quantification of MeV genomes, MeV-derived transgene expression and production of progeny particles.

4.3.3.1. PV-mediated dampening of IFN signaling in dual virotherapy

To observe whether the hypothesis of transient IFN-dampening by PV holds true in the dual virotherapy setting, I performed RT-qPCR of *IFNB1* and *CXCL10* transcripts (**Figure 4-12**).

As expected, PV alone elevated neither *IFNB1* nor *CXCL10* transcript levels, compared to mock-treated cells. This was true for the time-point of MeV infection (24 h p.PV) and 48 h thereafter. MeV infection, on the contrary, increased *IFNB1* levels 690- or 307-fold and *CXCL10* levels 83- or 654-fold in BxPC-3 or U251 cells, respectively. Interestingly, when both viruses were applied *IFNB1* and *CXCL10* levels remained significantly elevated compared to PV or mock treated cells. However, the addition of PV reduced the *IFNB1* induction 35 % (BxPC-3) or 48 % (U251) compared to MeV-infection. Equally, CXCL10 levels were reduced ca. 47 % in both cell lines. This PV-mediated decrease was statistically significant in U251 cells for *IFNB1* and BxPC-3 cells for *CXCL10* (all significant combinations are shown in **Figure 7-7**). Thus, PV could not abolish the IFN-induction MeV elicits, but did indeed reduce IFN signaling.

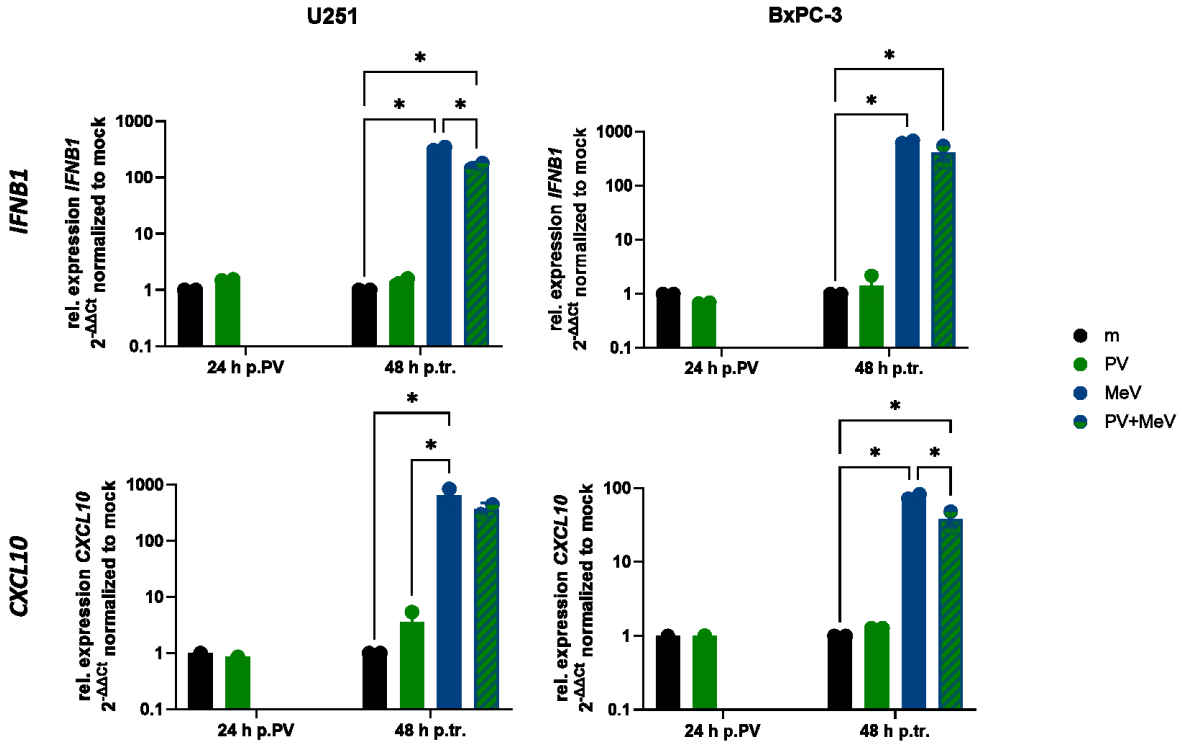

Figure 4-12: Induction of INFB1 under dual virotherapy

I infected cells with PV at MOI 2 (U251) or MOI 5 (BxPC-3) and 24 h later with MeV at an MOI of 1 (both cell lines). I harvested RNA 24 h after PV infection (time point of MeV infection) and 48 h after completion of treatment. I analyzed transcript levels of *IFNB1* and *CXCL10* via RT-qPCR for BxPC-3 and U251 cells. Average of two independent experiment is depicted, error bars indicate standard deviation. m - mock, PV - Parvovirus, MeV - Measles Virus, p.PV - post PV infection, p.tr. - post treatment; * - $p < 0.002$ in two-way ANOVA with Tukey's multiple comparisons test; significance only shown for selected combinations for clarity

4.3.3.2. Effect of dual virotherapy on MeV replication and transgene expression

Since MeV is very sensitive to IFN signaling, I next assessed whether the slight reduction of IFNB1 and downstream signaling could enhance MeV replication and spread. To this end, I performed RT-qPCR of MeV genomes in cells after dual virotherapy and observed transgene expression in time-resolved live cell microscopy.

RT-qPCR of MeV genomes showed no effect of the preinfection with PV (**Figure 4-13**). Normalized to *ACTB* transcripts, BxPC-3 cells showed slightly higher fold changes of MeV, compared to U251, which is in line with the higher sensitivity of that cell line to MeV. However, neither cell line showed an in- or decrease of MeV genomes when PV was also present. Thus, for the time point observed, the PV-mediated dampening of IFN signaling did not elicit an advance for MeV replication.

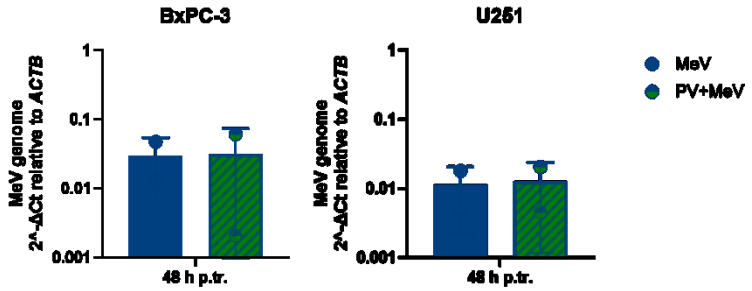

Figure 4-13: MeV genome under dual virotherapy

I infected cells with PV at MOI 2 (U251) or MOI 5 (BxPC-3) and 24 h later with MeV at an MOI of 1 (both cell lines). I harvested RNA 48 h after completion of treatment. I used a MeV-specific primer for cDNA synthesis and quantified MeV genomes via qPCR. $2^{-\Delta Ct}$ values (normalized to *ACTB*) of two independent replicates are shown with standart deviation. PV – Parvovirus; MeV – Measles virus

I additionally assessed the effect of concomitant PV infection on MeV spread through its transgene expression. The MeV construct used encodes for eGFP and I could thus observe the eGFP signal over time to assess viral spread and kinetic. To this end, I used an IncuCyte and measured phase and eGFP area every two hours over the course of 7 days. To normalize for cytotoxic effects, I divided eGFP area by the phase area for each time point. For visual clarity, I only depict treatment conditions where I infected with a MeV MOI of 1 (**Figure 4-14;** other MeV MOIs in appendix figure **Figure 7-8**).

MeV kinetics were largely comparable across treatment groups: eGFP expression became detectable around 22 h post-treatment, accompanied by a sharp increase in eGFP/phase area. This signal then plateaued and either rose only slightly (BxPC-3) or declined again (U251). Although the overall kinetics were similar, the absolute eGFP/phase values differed markedly between groups. Increasing PV doses consistently reduced MeV spread, with the effect being more pronounced in U251 than in BxPC-3 cells.

To quantify this difference, I compared the area under the curve (AUC) for each condition. Compared to MeV monotherapy, AUC values decreased dose-dependently to 86 %, 75 %, and 69 % in BxPC-3, and to 77 %, 49 %, and 28 % in U251 cells. This inhibitory effect of PV was independent of MeV dose: even at lower MOIs, where eGFP expression was already reduced, PV further suppressed MeV transgene expression in a dose-dependent manner (**Figure 7-8**)

This strong inhibition was unexpected and not consistent with qPCR data for MeV genomes or progeny particle titers. I therefore hypothesize that PV-induced cellular stress responses, including translational shutdown, may impair MeV transgene expression without equally affecting genome replication or virus production.

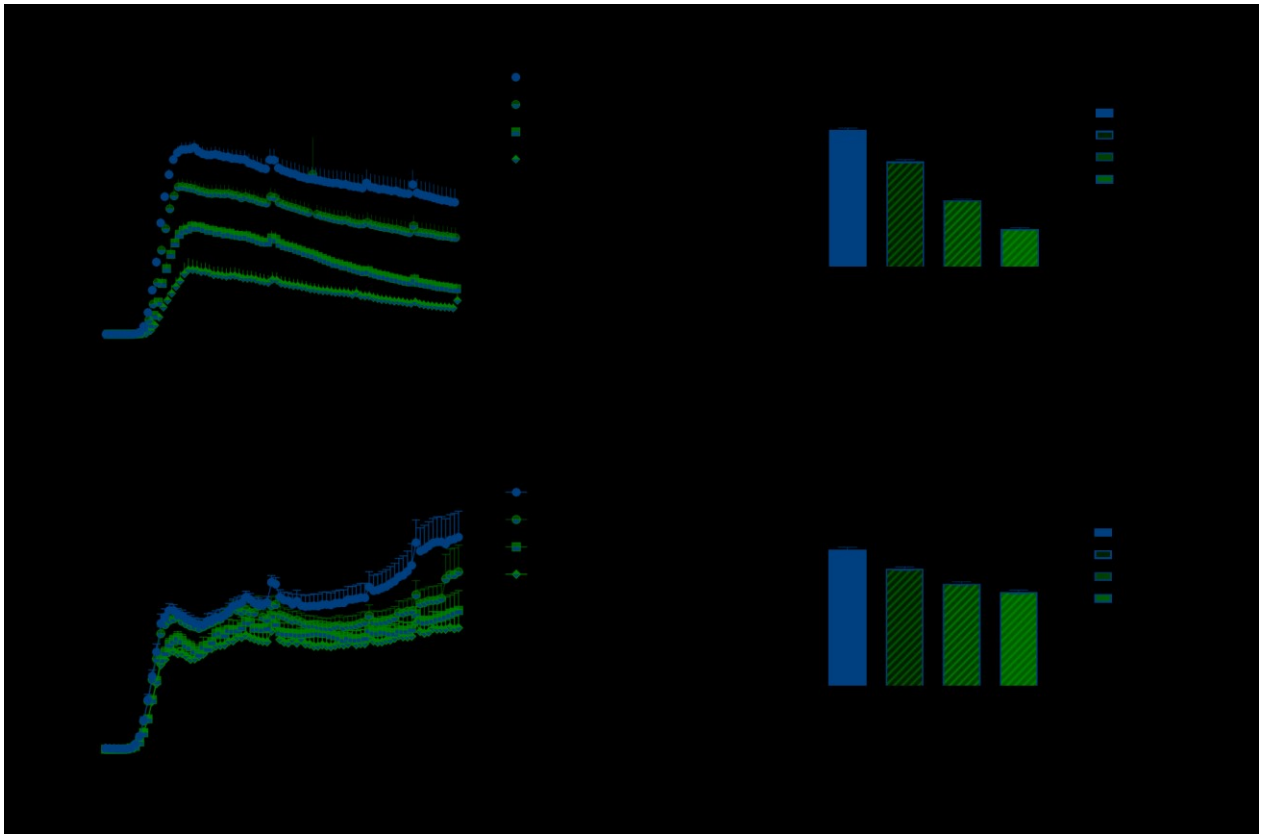

Figure 4-14: MeV transgene expression in dual virotherapy

I infected cells with PV at the indicated MOIs and infected with MeV at an MOI of 1 24 h thereafter. I place the plates in an IncuCyte and measured phase and eGFP area over the course of 7 days. I normalized eGFP expression to phase area and plotted it over time. For statistical analysis, I calculated the AUC and compared between treatment groups by One-way ANOVA with Tukey's multiple comparison test. * - p-value < 0.000028; AUC - Area under the curve; PV - Parvovirus; MeV - Measles virus; MOI - multiplicity of infection

Taken together, the effects of dual virotherapy in the two cell lines were complex. Cytotoxicity was limited and strongly influenced by the variable sensitivity of each cell line to one of the viruses. Synergistic interactions were only transient, with little biological relevance. Although PV reduced IFN signaling in combination treatments, this did not enhance MeV replication; instead, PV negatively affected MeV transgene expression.

However, these results may in part reflect limitations of a 2D monolayer system. The two viruses have distinct requirements for efficient replication: PV replicates S-phase dependently and thus benefits from low seeding density, allowing for multiple division cycles before a high confluence is reached. MeV, on the

other hand, relies on cell-to-cell contact and syncytia formation, which is optimized by ~70% confluence at the time point of infection. These opposing requirements complicate assessment of dual virotherapy in monolayer cultures and may lead to over- or underestimation of treatment efficacy. To overcome this, I employed a 3D heterotypic PDAC spheroid model for a final evaluation of the dual virotherapy approach.

4.3.4. Dual virotherapy in 3D PDAC model

The spheroids, composed of PDAC cells, endothelial cells and fibroblasts, better resemble a patient's tumor and its microenvironment and allow for heterogeneous cell cycle distribution in outer rim versus spheroid core. In the spheroid model, I assessed cytotoxicity, synergy, INF induction and MeV-transgene expression under dual virotherapy.

I assessed cytotoxic effects with CellTiterGlo® 3D, measuring ATP content of lysed spheroids in a luciferase-based assay (**Figure 4-15 A** and extended dose range in). The spheroids were sensitive to treatment with both viruses and showed dose-dependent decrease in cell viability. At the higher MOI, the effect of monotherapy with MeV was higher than PV, resulting in a 75 % or 51 % reduction in cell viability, respectively. When the two viruses were combined, no additional cytotoxic effect was observed; cell viability remained similar to that of the most effective monotherapy. I also extended the PV dose range further (**Figure 7-9**). Still, MeV monotherapy elicited a stronger effect than PV-treatment. On the contrary, higher PV doses (MOI 16 and 64) reduced MeV-driven cytotoxicity. Using all dose-combinations as input for synergy analysis with SynergyFinderPlus, this also led to negative synergy scores for the dose combinations with high PV MOIs. This resulted in an overall ZIP score of -12-37, indicating a slightly antagonistic combined effect (**Figure 4-15 B**).

I also investigated the effect on transcript levels of *IFNB1* and the downstream effector CXCL10 on day 3 p.tr.. Similiar to the monolayer culture, PV treatment elicited no induction of either target. MeV, on the hand, dose-dependently increased transcript levels to a maximum of 163- or 15-fold for *IFNB1* and *CXCL10*, respectively. Interestingly, the previously observed (slight) reduction with the addition of PV was only observable in the combination of an intermediate MeV and high PV dose. This was the case for both targets tested. All other combinations elicited an even stronger induction compared to MeV monotherapy.

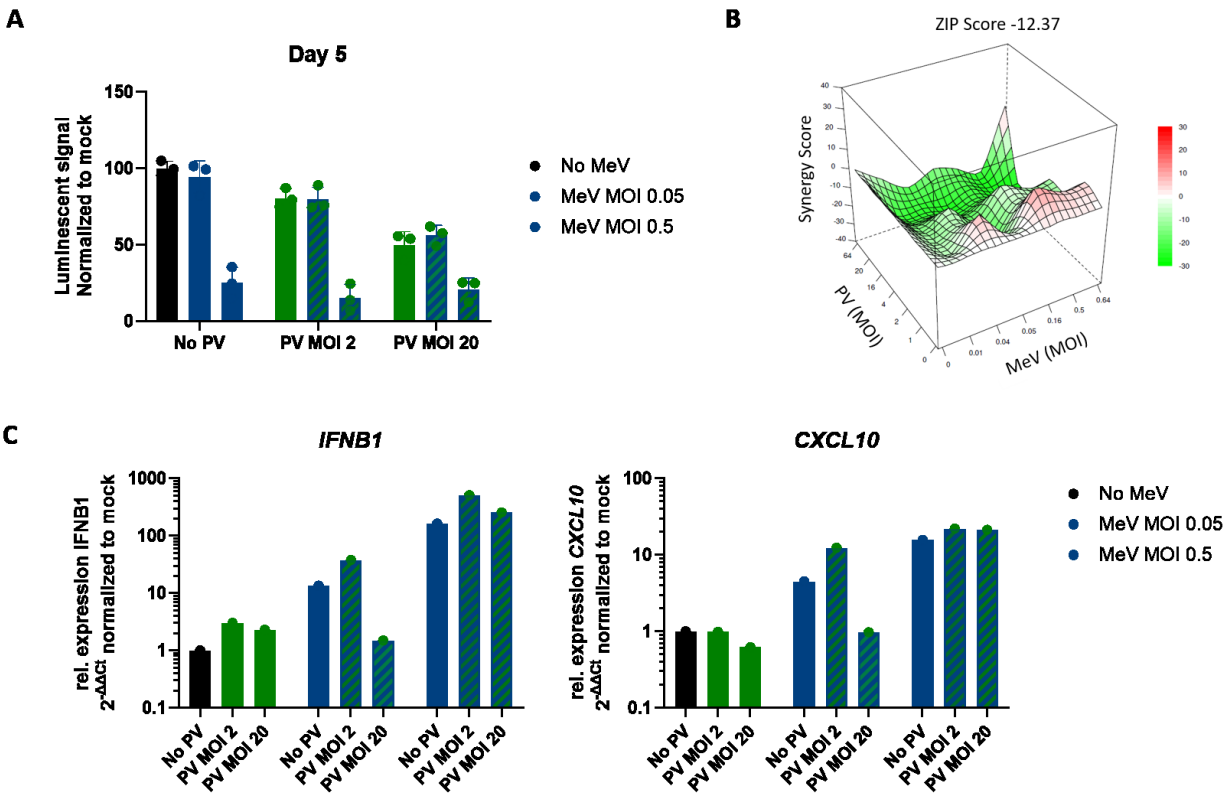

Figure 4-15: Dual virotherapy in heterotypic spheroid model

I treated PDAC spheroids, composed of PDAC cells (AsAnPaCa), endothelial cells (HUVEC) and fibroblasts (MRC-5) in a ratio of 1:2:3, with PV and MeV. (A) 5 days post treatment with the two viruses at the indicated MOIs, I performed the ATP-based cytotoxicity assay CellTiterGlo® 3D. Mean and standard deviation of three technical replicates is shown. (B) I performed synergy analysis with the SynergyFinderPlus web application using cytotoxicity data from CellTiterGlo® 3D assays of all tested dose-combinations in the spheroid model. I used the ZIP model for synergy calculation. ZIP scores around 0 (white) indicate an additive effect, negative values (green) antagonism and positive values (red) synergy. (C) 3 days p.tr., I harvested spheroids, pooled technical triplicates, isolated RNA and performed RT-qPCR on *IFNB1* and *CXCL10*. . $2^{-\Delta\Delta CT}$ values, normalized to *ACTB* and mock-treated controls, in response to the respective treatment are depicted.

In addition to cytotoxicity and analysis of IFN signaling, I also observed the spheroids microscopically after the treatment with the two viruses (**Figure 4-16**). Phase-contrast imaging revealed spheroid size and integrity as indicators of cytotoxic effects. In untreated spheroids and at early time points, the outer rim appeared sharp and well-defined, whereas higher viral MOIs reduced spheroid integrity. This effect was particularly pronounced in MeV-treated spheroids at 14 days post-treatment, which appeared less compact and were surrounded by single cells detached from the dense core. These morphological indicators of cytotoxicity were consistent with CellTiter-Glo® 3D assay results, which showed MeV monotherapy to be the most effective. Fluorescence microscopy further confirmed MeV infection through detection of MeV-encoded eGFP. At 2 days post-treatment, eGFP intensity correlated with MeV MOI, with the strongest signal observed at MOI 0.5. Interestingly, co-treatment with high-dose PV suppressed MeV transgene expression at this early time point. However, at later time points, eGFP dynamics changed: in

the presence of PV, eGFP signals was sustained longer or peaked later, suggesting a shifted expression pattern under combination treatment.

Interestingly, this is not in line with the observed transgene expression in the monolayer culture (**Figure 4-14**), where the kinetic was similar across combination-doses but the eGFP area was reduced dose-dependently. Possibly, this is because multiple rounds of infection may occur in the spheroid model when the virus penetrates deeper, still viable, cell layers of the spheroids.

All in all, the dual virotherapy approach with PV and MeV yielded only limited synergistic effects. In the monolayer culture, cytotoxic effects remained modest overall, with U251 cells showing higher sensitivity to PV and BxPC-3 cells to MeV. Synergy analysis revealed transient synergistic interactions at early time points, but these were not sustained and often shifted to additive or antagonistic effects later on. Mechanistically, PV partially dampened the MeV-driven IFN response, however this did not translate into enhanced MeV replication; instead, PV dose-dependently suppressed MeV transgene expression, possibly through PV-induced cellular stress and translational inhibition. In PDAC spheroids, similar to the PDAC cell line, MeV was more cytotoxic than PV, and combinations at higher PV doses even reduced MeV efficacy, resulting in antagonistic synergy scores. Imaging and eGFP expression dynamics suggested that PV alters the temporal pattern of MeV spread rather than amplifying it.

Overall, these findings indicate that while PV can modulate the IFN response, its combination with MeV in the dual virotherapy does not improve cytotoxic efficacy and may even counteract MeV transgene expression at higher doses. The cell-type–specific sensitivities observed nevertheless informed the dosing of the triple radiovirotherapy.

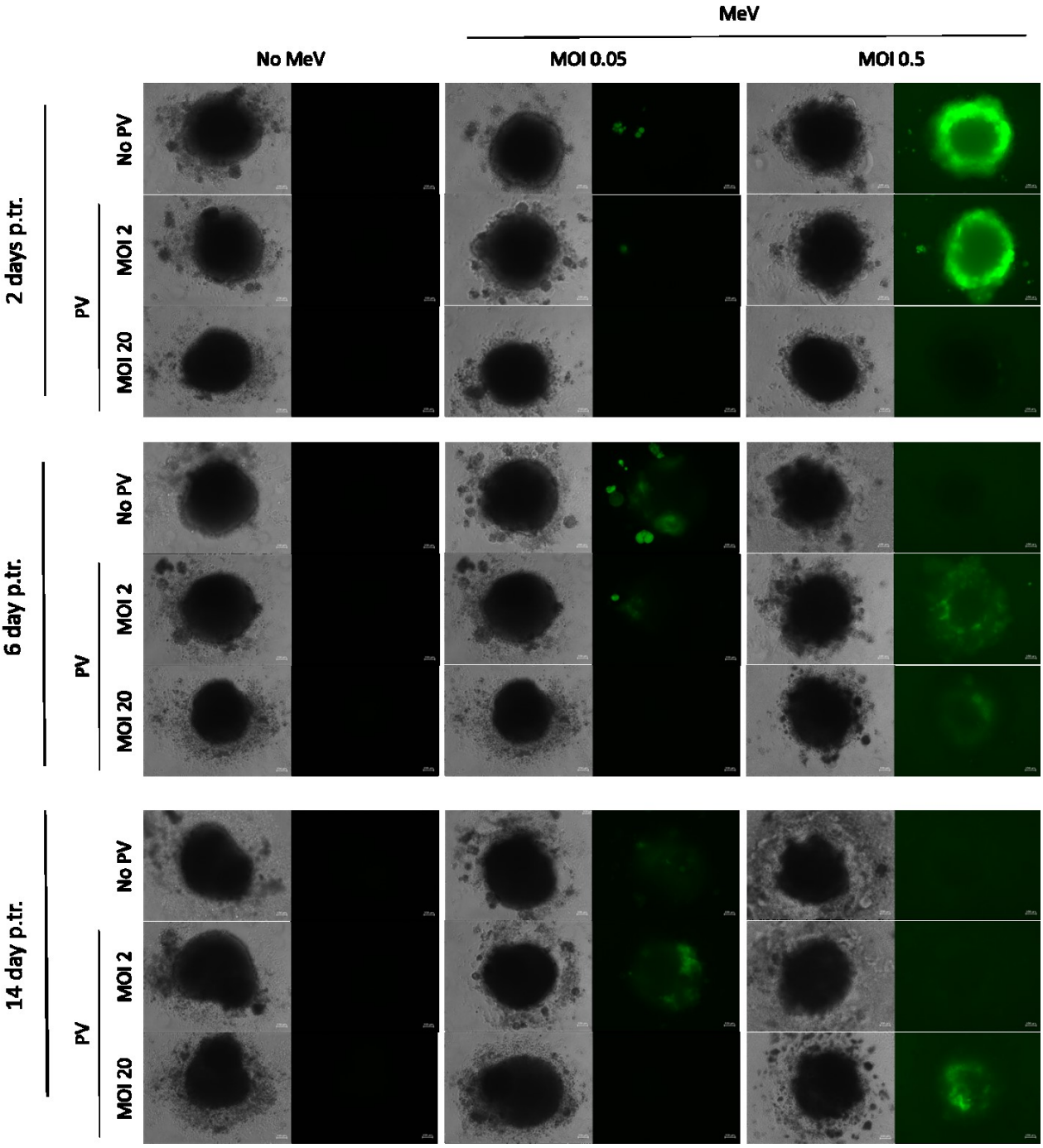

Figure 4-16: Microscopic observation of spheroids under dual virotherapy

I infected heterotypic PDAC spheroids with PV at MOI 2 and 20 and 24 h later with MeV at MOI 0.05 and 0.5. I took images 2, 6 and 14 days after treatment of phase contrast and fluorescent signal in the eGFP channel. 20x objective, scale bar indicates 100 µm

4.4. Triple radiovirotherapy: Analysis of cytotoxicity and underlying signaling

Previous work within the group and of collaboration partners around Laurent Daeffler at IPHC in Straßbourg found the combination of MeV or PV with ionizing radiation synergistic (Derani *et al,* manuscript in preparation; Daeffler *et al*, manuscript in preparation). The application schedule proofed relevant especially for the combination of PV and radiation: Only simultaneous application (i.e. PV infection immediately after irradiation) elicited enhanced and meaningful cytotoxicity and synergy. For the combination of MeV and radiotherapy, a synergistic effect was observable independent of the order of application.

Based on that data, I investigated the triple combination of PV, MeV and radiotherapy, despite the mixed results of dual virotherapy described here. For triple radiovirotherapy, I first irradiated cells, immediately followed by PV treatment and infected 24 h thereafter with MeV. This schedule is subsequently referred to as triple radiovirotherapy. I assessed cytotoxicity with XTT and crystal violet assays, analyzed synergy and performed experiments concerning the underlying mechanism, including the effect on IFN signaling, replication of the two viruses and immunogenic cell death (ICD).

4.4.1. Combined cytotoxic effects of radio- PV- and MeV-therapy

I initially assessed the cytotoxicity of the triple combination using XTT assays (**Figure 4-17**). To account for differences in cell line sensitivity, I slightly adjusted the viral doses, increasing the MOI of PV for BxPC-3 and the MOI of MeV for U251. Each virus alone induced cytotoxicity in both cell lines, and radiation at 5 Gy also reduced viability in BxPC-3 cells at both time points and in U251 cells at day 5. High-dose combinations produced a strong cytotoxic effect, reducing cell viability to nearly 0 % in both cell lines at both time points. In U251 cells, this effect was mainly driven by PV infection, which alone caused marked cytotoxicity at an MOI of 2. On day 5, cytotoxicity increased dose-dependently across all treatment modalities. By day 7, however, cells—particularly U251—showed partial recovery.

Since calculation of the ZIP score for synergy assessment requires three or more doses for each component, I could only calculate the less robust highest single agent (HSA) score for these XTT-based cytotoxicity datasets (HSA plots and scores for day 7 depicted in **Figure 7-10**). The HSA synergy analysis revealed scores of 36 or 22 for BxPC-3 and U251 cells, respectively, for the combination with 5 Gy radiation, indicating a highly synergistic combined effect of the triple combination. With these promising preliminary findings, I further extended the dose combinations tested to perform more robust synergy analysis.

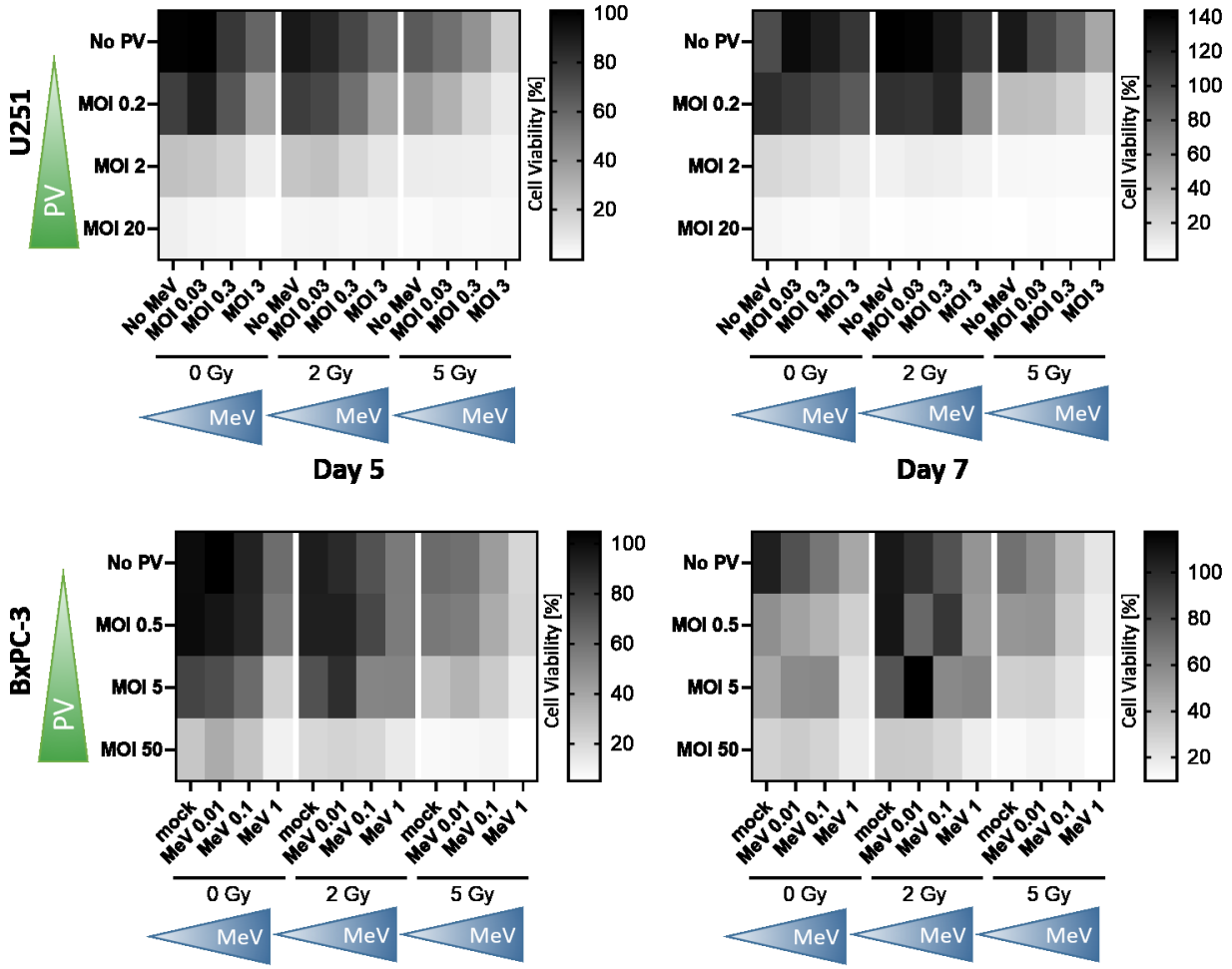

Figure 4-17: Initial assessment of triple radiovirotherapy by XTT

I assessed cytotoxic effects of the triple combination of radiation, PV and MeV by XTT assay. I irradiated cells, then immediately infected with PV and 24 h thereafter with MeV. MOIs of each virus and radiation dose are indicated: On day 5 and 7 p.tr., I analyzed the metabolic activity of the cells. Data is normalized to the average of the mock-treated samples for each time point and shown in heat maps. N=2 biological replicates.

To test extended dose combinations of five viral MOIs and 4 radiation doses, I performed crystal violet assays. Again, I seeded cells and irradiated 24 h later, immediately followed by PV infection. After another 24 h, I infected the cells with MeV. Five days after completion of the treatment, I stained the cells with crystal violet and quantified the signal by dissolving the stain in acetic acid and measuring the OD value. Heat maps and bar graphs show the resulting cell viability data, normalized to untreated cells (**Figure 4-18**).

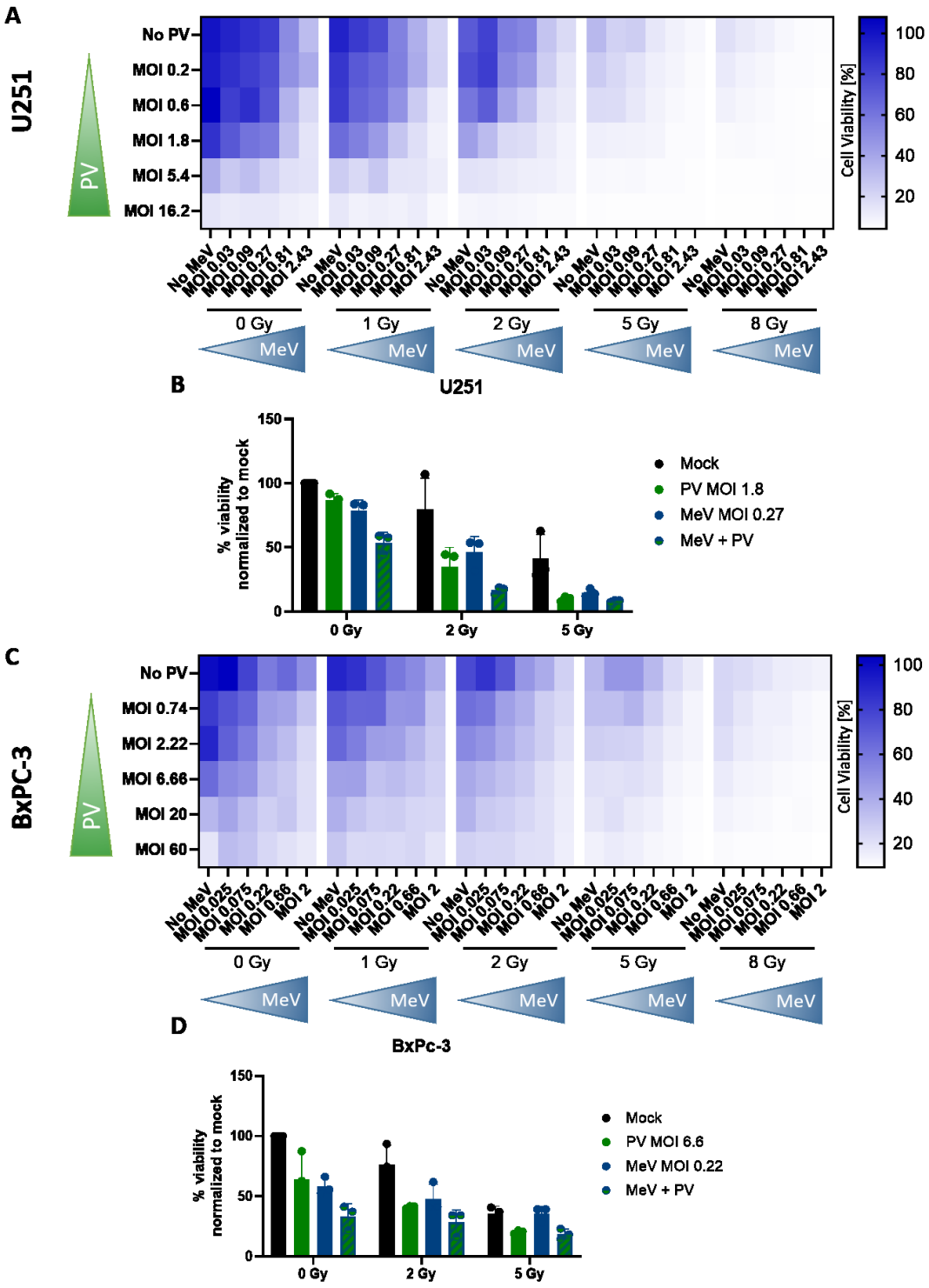

Figure 4-18: Cytotoxicity analysis of expanded dose combinations via crystal violet assays

I performed crystal violet assays to assess cytotoxicity of expanded dose combinations of the triple radiovirotherapy on U251- (A-B) and BxPC-3 (C-D) cells. I irradiated cells at 1, 2, 5 or 8 Gy and immediately infected cells with PV at the indicated MOI. 24 h later, I infected cells with MeV at the indicated MOI. 5 days after treatment, I stained the cells with crystal violet. I let the stain dry and dissolved it in acetic acid to quantify through measurement of the OD. OD values, normalized to non-irradiated, non-infected cells are depicted in heat maps (A, C). Selected dose combinations are shown in bar graphs for better visualization (B, D). N=3 biological replicates, mean (A-D) and standard deviation (B, D) is shown.

In BxPC-3 cells (**Figure 4 17 B**), a gradual decrease in cell viability was observed with increasing irradiation doses. This reduction was enhanced, when cells were also infected with PV. The addition of MeV at different MOIs further decreased viability. I detected a similar pattern in U251 cells (**Figure 4 17 A**), although the overall reduction in viability was less pronounced at lower radiation doses, compared to BxPC-3.

I selected dose combinations of intermediate viral MOIs for clearer visualization of these effects (**Figure 4 17 B, D**): Irradiation or viral infection alone led to a moderate decrease in viability, whereas combinations of irradiation with PV and MeV resulted in the lowest cell viability.

All in all, a combined cytotoxic effect of the triple combination was observable and dose combinations could be identified, where monotherapy was of limited toxicity, but combination resulted in markedly decreased cell viability.

4.4.2. Triple radiovirotherapy is synergistic in U251 cells

I then used the cell viability data gathered on the extended dose combinations to assess whether the observed combined cytotoxic effect was synergistic. To this end, I performed synergy analysis using the ZIP synergy model in SynergyFinder 3.0. I analyzed three replicates separately and depict the individual ZIP score values and their mean with standard deviation in **Figure 4-19**. For visualization of the individual dose-synergy relation, I additionally used averaged cytotoxicity data of three replicates as input and thereby calculated a single synergy score for the triple combination at each radiation dose (**Figure 7-11**)

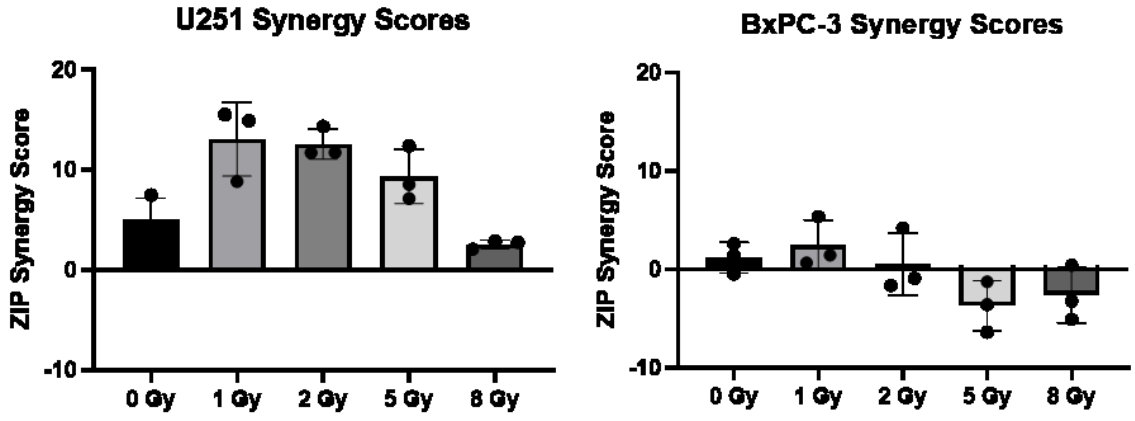

Figure 4-19: Synergy analysis of triple radiovirotherapy

I calculated synergy using the ZIP model in SynergyFinder 3.0. Using the replicates of the cytotoxicity analysis in crystal violet assays as individual inputs, I derived synergy scores of the two viruses at each radiation dose applied. Depicted are the individual synergy scores of the three replicates with mean and standard deviation for BxPC-3 and U251.

Synergy scores differed between the two cell lines tested: For BxPC-3, the triple combination did not yield synergy scores above 10, which would be considered robustly synergstic. On the contrary, synergy scores were around 0 for most combinations or even below 0 at higher radiation doses. Thus, the combined effect of the triple combination therapy in this cell line does not go beyond an additive one.

U251 cells, on the other hand, showed robust and reproducible synergy scores of 10 and above for the combination of the two viruses with 1 and 2 Gy and around 8 for the combination with 5 Gy. Thus, the three treatment modalities appear synergistic in this cell line at certain dose combinations.

Cytotoxicity and synergy analysis of triple virotherapy again revealed a variable pattern between cell lines: While I detected combined cytotoxic effects in both cell lines and triple therapy reproducibly resulted in the largest decrease of cell viability, the combination was synergistic in U251 cells only. I next assessed whether the underlying signaling and effect on viral replication would also reflect these observed patterns.

4.4.3. Mechanistic analysis of triple radiovirotherapy

4.4.3.1. Triple virotherapy and IFN signaling

For the combination of MeV and radiation, previous results within the group (Derani *et al*, manuscript in preparation) and the transcriptome analysis presented in this thesis (section **4.1**), suggested increased levels of (innate) immune signaling under combination treatment. In the dual virotherapy approach, I could detect a trend of PV-mediated dampening of *IFNB1* and downstream signaling. I thus analyzed transcript levels of *IFNB1* and *CXCL10* in the triple radiovirotherapy approach (**Figure 4-20**).

In line with the previous results, PV alone did not induce levels of *IFNB1* or *CXCL10* at any time point measured. Adding radiation, however, increased transcripts of both targets up to ca. 15-fold in presence and absence of PV. Infection with MeV drove the strongest induction of both *CXCL10* and *IFNB1* at all time –points, which was slightly enhanced when cells were also irradiated. As before, cells infected with both viruses showed elevated levels of the target transcripts, but slightly reduced compared to infection with MeV only. This was independent on the addition of radiotherapy.

However, these observations were only a trend. I observed significant increases or decreases only for limited combinations. Interestingly, only combinations of radiotherapy and MeV elicited a significant increase, (5 Gy for IFNB1 and 2 Gy for CXCL10). MeV infection without radiotherapy did not elicit a significant increase for any target, cell line or time point. Equally, only the triple combination at 5 Gy showed a significant decrease in CXCL10 levels, compared to radiation at 5 Gy with MeV infection. In terms

of kinetic, I observed the highest fold changes of target transcripts at 48 h p.tr. The described pattern of PV-mediated reduction of MeV-induced *IFNB1* and *CXLCL10* transcripts was present at all time points

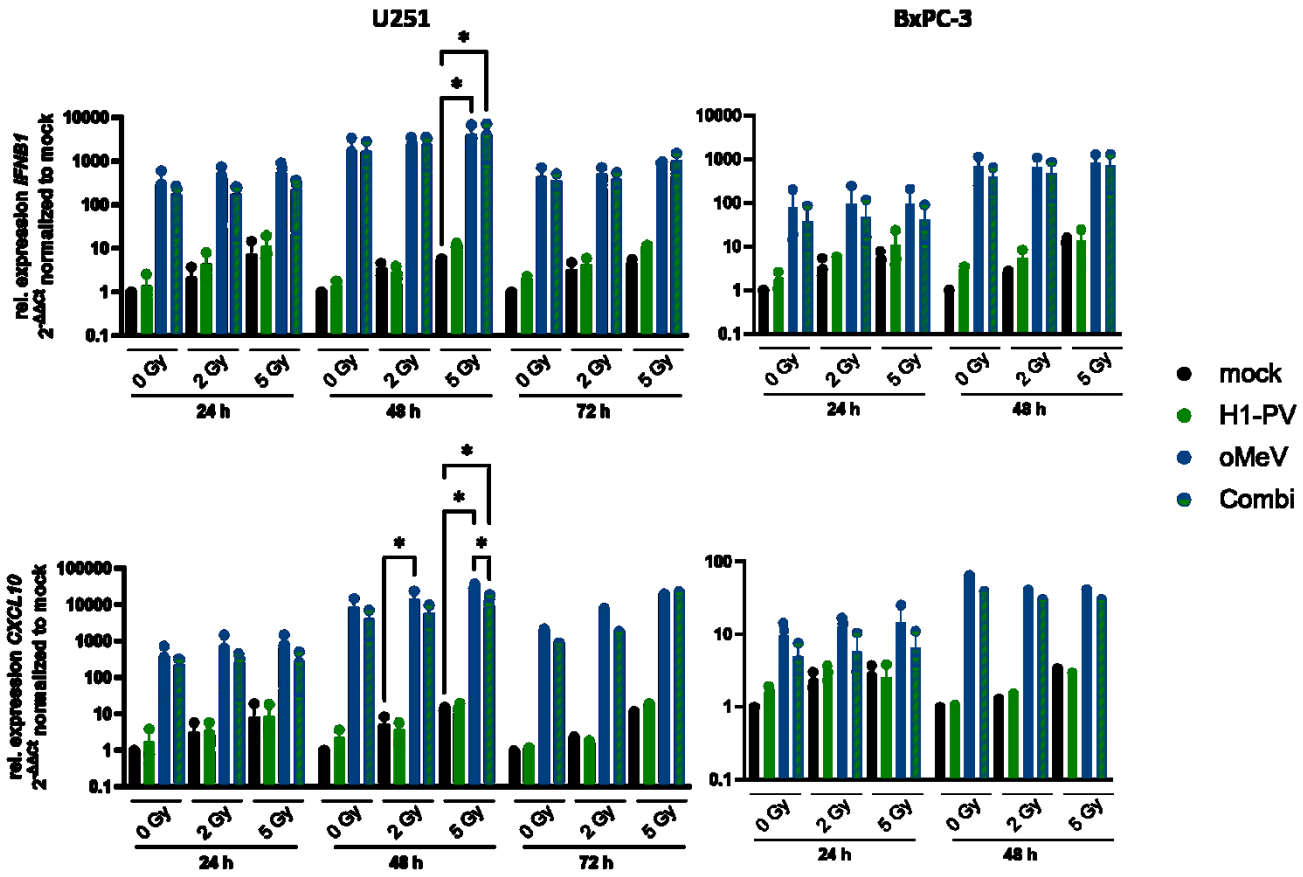

Figure 4-20: Assessment of IFNB1 and CXCL10 on transcript level under triple radiovirotherapy

I treated cells with 2 or 5 Gy of radiation, immediately followed by PV infection at MOI 2 (U251) or 5 (BxPC-3). 24 h later, I infected cells with MeV at MOI 0.1. I harvested cell pellets 24, 48 (BxPC-3 and U251) and 72 h p.tr.(U251 only) and isolated RNA. By RT-qPCR, I assessed *IFNB1* and *CXCL10* transcript levels. N=3 biological replicates for most time points; N=2 biological replicates for 48 h IFNB1 (BxPC-3) or CXCL10 (U251) and 72 h IFNB1 (U251); N=1 for CXCL10 at 48 h (BxPC-3) or 72 h (U251). * - p<0.05; only shown for comparisons of non-infected cells to the respective MeV or combi-infected treatment group and for MeV-infected cells with the respective combi-infected condition. Celine Bauer has performed several cDNA syntheses for the RT-qPCRs shown here.

In addition to the analysis of transcript levels of *IFNB1* and *CXCL10*, I also assessed the release of these cytokines under triple radiovirotherapy. To this end, I performed ELISAs on the supernatant of triple radiovirotherapy-treated cells (**Figure 4-21**).

Neither IFN-β nor CXCL10 was detectable in the supernatant of U251 cells treated with PV or radiotherapy alone or in combination. CXCL10 was present at levels close to the detection limit in BxPC-3 cells under these conditions. In line with the observations on the transcript level, MeV- infection resulted in the release of both cytokines. This was sustained in dual viro- and triple combination therapy. However, the

addition of PV, independent of radiotherapy, reduced the levels of secreted IFN-β and CXCL10 for both cell lines. Again, this effect was not statistically significant and replicates differed largely. The trend, however, remains observable and reproducible across assays on transcript and protein level.

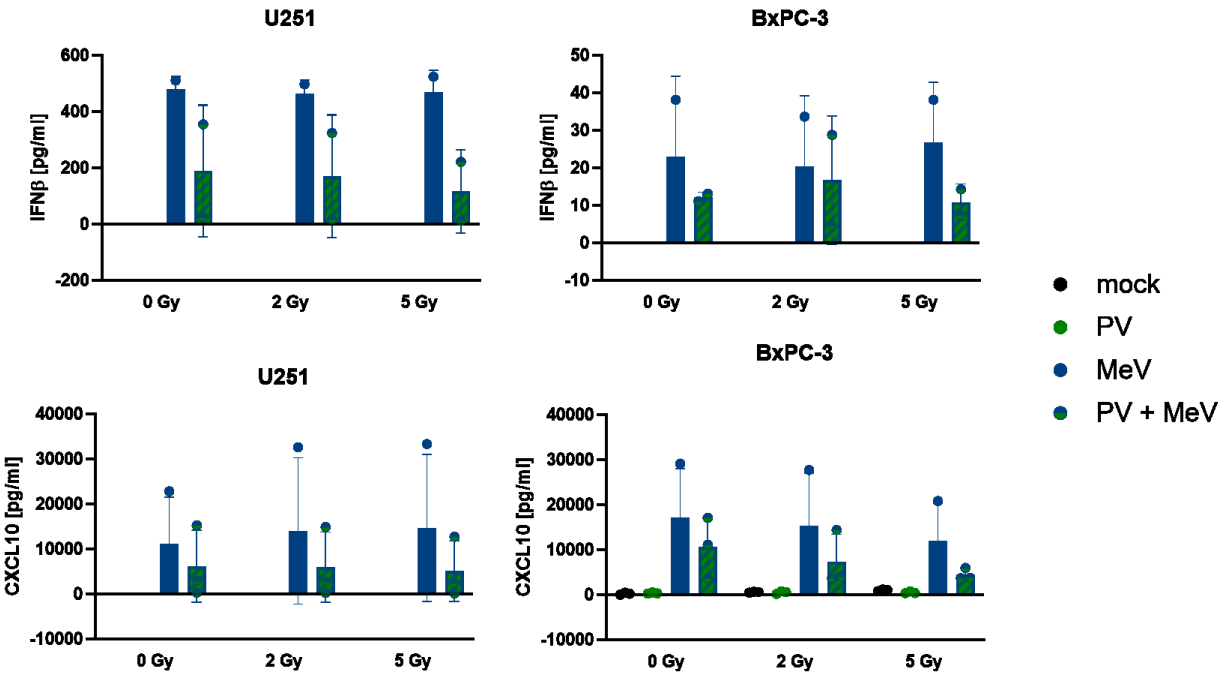

Figure 4-21: Release of CXCL10 and IFNβ- in triple radiovirotherapy

I measured the concentration of CXCL10 and IFN-β in the supernatant of BxPC-3 and U251 cells 48 h after completion of triple radiovirotherapy through ELISA. The graphs show mean and standard deviation of two or three biological replicates. PV - Parvovirus; MeV - Measles Virus; Stefanie Sawall performed one replicate of IFN-β and CXCL10 ELISAs.

To further investigate the contribution of interferon signaling to the efficacy of triple radiovirotherapy, the combination treatment was tested in cell lines with reduced ability to mount an interferon response. From the initial candidate screen, U87 (GBM) and T3M4 (PDAC) cells were selected, as both exhibited lower levels of intrinsic interferon signaling and showed less attenuation of MeV replication. In these models, I evaluated triple radiovirotherapy for its cytotoxic effects and the degree of treatment synergy (**Figure 4-22)**.

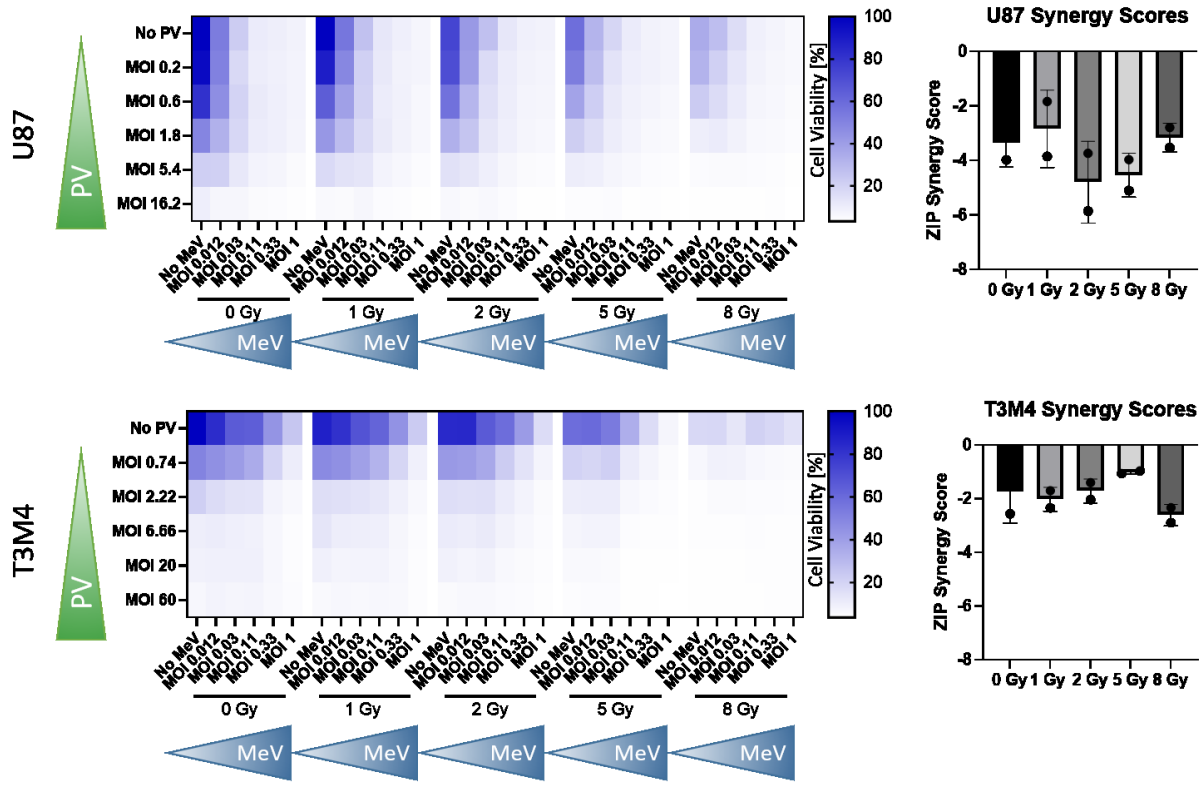

Figure 4-22: Cytotoxicicty and synergy of triple radiovirotherapy in cell lines with reduced IFN signaling

I treated U87 and T3M4 cells with the triple radiovirotherapy regimen. I applied 1- 8 Gy of radiation, PV doses ranging from MOI 0.2-16.2 (U87) or MOI 0.74-60 (T3M4) and MeV at MOIs 0.12-1. I measured cytotoxicity with crystal violet assay on day 5, quantifying the residual stain by dissolving in acetic acid and measuring the OD. Heat maps show the average of two independent replicates. Using the replicats as individual inputs for synergy analysis, I calculated ZIP synergy scores. In the bar graphs, the individual values, their mean and standart deviation are depicted. PV – Parvovirus; MeV – Measles virus; MOI – multiplicity of infection

I treated the cells in the triple combination regimen. On day 5, I fixed and stained remaining cells with crystal violet and quantified the dissolved stain through measurement of the OD. U87 cells showed high sensitivity to MeV infection, a MOI of 0.11 resulted in near-complete eradication of cells. PV-infection also reduced cell viability to nearly 0 % for the highest MOI of 16.2. T3M4 cells showed a reverse pattern here, highest cytotoxicity levels were reached at the intermediate PV MOI of 6.6, the highest MOI of 1 of MeV resulted in 25 % cell viability. Compared to U251 and BxPC-3 cells, U87 and T3M4 cells were more sensitive to treatment with the virus monotherapies. Radiation also showed a dose-dependent cytotoxic effect, which was similar for the two cell lines.

Strikingly, the cytotoxicity pattern of the combinations was uniform: combining the treatment modalities did not substantially enhance the effect beyond that observed with the most potent single treatment. Cell viability was therefore primarily determined by the strongest monotherapy in each setting, with limited additional reduction achieved through combination. This is also reflected in the synergy scores. The scores are very similar across radiation doses ranging from -2 to -6 for U87 and -1 to -3 for T3M4, suggesting a slight antagonistic effect of the treatment components.

Compared to the results obtained in U251 and BxPC-3 cells, the observed effects in U87 and T3M4 are strikingly different. The pairs resemble each other more in the supposed classification I undertook here based on their IFN signaling pattern than their entity. For the IFN-reduced cell lines, mainly the high sensitivity to one viral construct seemed to dictate the treatment efficacy and in a result, the synergy score.

4.4.3.2. Effect of triple radiovirotherapy on MeV and PV replication

I next assessed the effect of the triple combination regimen on the replication of the two viruses.

To quantify PV under triple radiovirotherapy, I performed western blots to detect the viral NS1 protein (**Figure 4-23**). I harvested cell lysates 48 h after completion of the treatment and performed SDS-PAGE followed by western blot, probing for the NS1 protein with a polyclonal antibody. On the membrane, a band at 80 kDa was visible only in PV-infected conditions, indicating expression of PV NS1 protein and specificity of the antibody to the PV protein (**Figure 4-23 A**). I quantified the band intensities and normalized the signal to β-Actin. Variance between replicates was high, I thus indicate samples of the same run by connecting them with a grey line (**Figure 4-23 B**). Overall NS1 expression was lower In BxPC-3 cells, which is in line with the generally reduced susceptibility of the cell line. The addition of MeV did not alter PV protein expression in U251 cells. In one of three replicates, radiation reduced NS1 expression to ca. 50 %. In BxPc-3 cells, a trend towards decreased NS1 expression in presence of MeV was observable. This effect did not reach statistical significance.

Overall, PV replication, as indicated by NS1 expression, was not affected by either radio- or MeV-therapy alone or in combination.

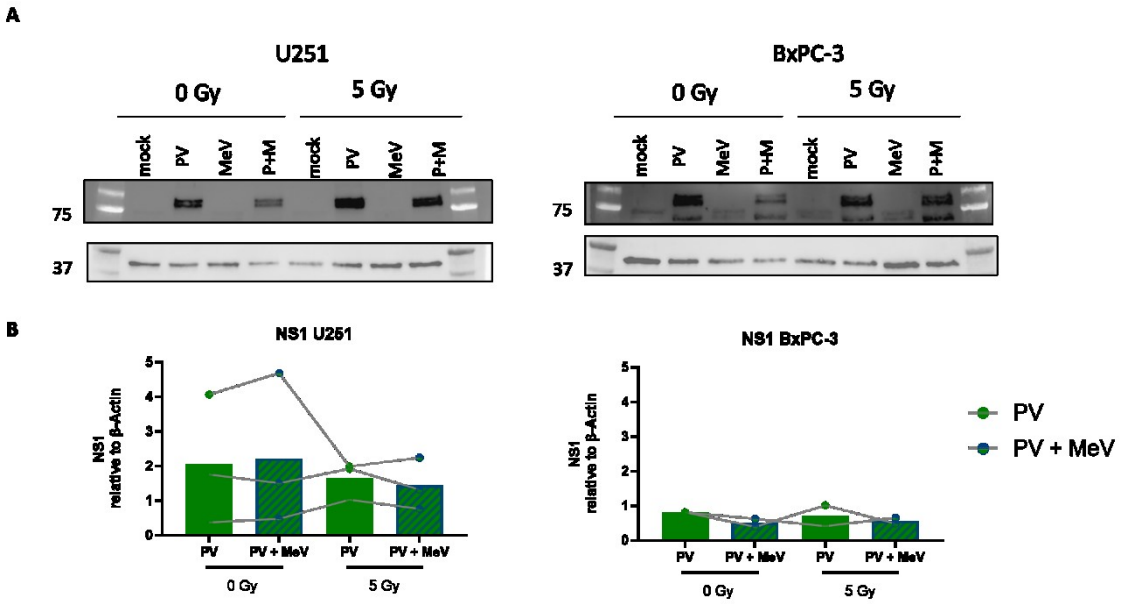

Figure 4-23: PV protein expression under triple radiovirotherapy

I treated irradiated cells with 5 Gy and immediately infected with PV at an MOI of 2. 24 h later, I infected cells with MeV at an MOI of 1. I harvested cell lysates 48 h p.tr. I performed SDS-PAGE and western blot to analyze expression of the PV NS1 protein (A). I quantified the band intensities in PV-infected conditions using FIJI software and normalized it to β-Actin. A grey line connects samples from one experiment (B). Mean of replicates is indicated by the bar N=3 for U251 and N=2 for BxPc-3. PV – Parvovirus; MeV – Measles virus; P+M – Parvo and measles virus; Katja Kerner and Stefanie Sawall performed SDS-PAGE and western blotting for 2 of the 3 replicates shown here.

To assess the effect of the triple combination on MeV replication, I quantified MeV progeny particles. Importantly, I applied radio- and PV-therapy at doses comparable to those for the other mechanistic assays, but reduced the MeV MOI to 0.03. The use of this low MOI permitted multiple rounds of replication and infection, thereby emphasizing the effect on MeV replication capacity rather than initial cell susceptibility. I finally determined MeV infectious particles by serial dilution titration assays (**Figure 4-24**).

MeV progeny particle production was largely unchanged by the addition of either PV or radiotherapy or its combination. For U251 cells, a non-significant trend towards decreased MeV replication was observable when cells were also irradiated with 5 Gy, irrespective of PV infection. On the contrary, MeV replication seemed slightly enhanced in BxPC-3 at the high PV doses with increasing irradiation dose. Again, this effect was not statistically significant. All in all, MeV replication was stable across all treatment conditions and no consistent differences between the cell lines were detectable.

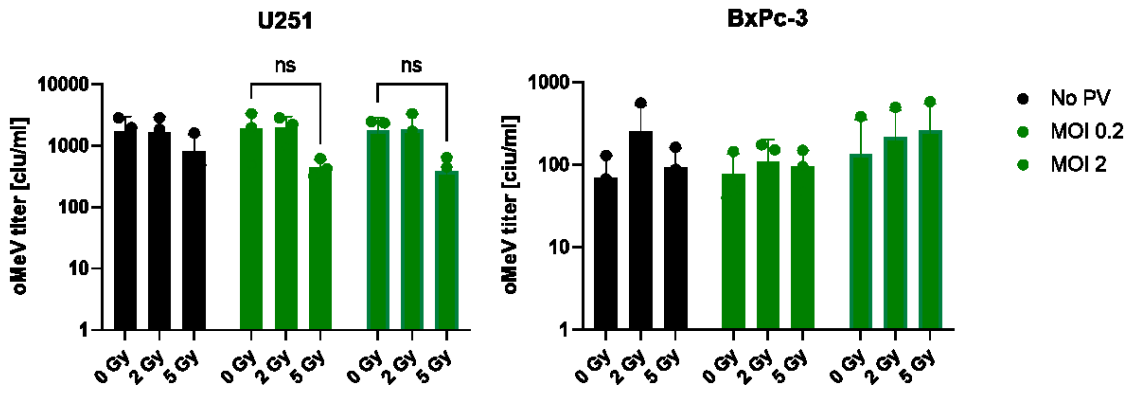

Figure 4-24: Effect of triple radiovirotherapy on MeV replication

I seeded cells in 6-well plates, and irradiated them with 2 or 5 Gy on the next day, immediately followed by PV infection at an MOI of 0.2 or 2. 24 h later, I infected cells with MeV at an MOI 0.03. 48 h afer completion of the treatment, I scraped cells and snap froze them to release viral particles. I then performed serial dilution titration assays to determine the concentration of infectious MeV particles in each condition. N=3 biological replicates; mean and standard deviation is depicted.

As a second measure of MeV replication, I assessed the signal of MeV-encoded eGFP using live-cell imaging with the IncuCyte. eGFP is expressed in MeV-infected cells and can thus indicate MeV spread. eGFP expression was normalized to cell confluence (phase area) to correct for cytotoxic effects, and the eGFP area/phase metric was monitored over 7 days following treatment (**Figure 4-25 A**).

The addition of PV reduced MeV eGFP expression in a dose-dependent manner in both cell lines. High PV doses (MOI 2 and 20 for U251; MOI 5 and 50 for BxPC-3) led to an almost complete loss of detectable eGFP signal. In U251 cells, eGFP kinetics differed between radiation doses: The increase in eGFP signal and spread occurred earlier and reached higher levels when cells had been irradiated, independent of the radiation dose. By contrast, eGFP kinetics in BxPC-3 cells were largely uniform in non-irradiated conditions and at 2 Gy, whereas irradiation with 5 Gy markedly reduced eGFP spread.

I assessed the cumulative eGFP area (AUC, **Figure 4-25 B**) to quantify these differences. The analysis confirmed the strong suppressive effect of PV. In addition, the radiation-associated increase in MeV spread in U251 cells was statistically significant, as was the reduction of eGFP expression in BxPC-3 cells at 5 Gy.

All in all, the effect of triple radiovirotherapy on MeV replication and spread was complex: I could not observe an effect on progeny particle production. On the contrary, eGFP signal as an indicator of MeV spread, was highly influenced by both radiation and PV: In U251 cells, radiation increased MeV spread, while high-dose radiation decreased viral spread in BxPC-3 cells. For both cell lines, however, additional infection with PV, especially at high doses, led to loss of eGFP signal. This strongly confirmed the findings in the dual virotherapy setting and led me to investigate the hypothesis of a PV-mediated integrated stress response (IRS) and translational shutdown.

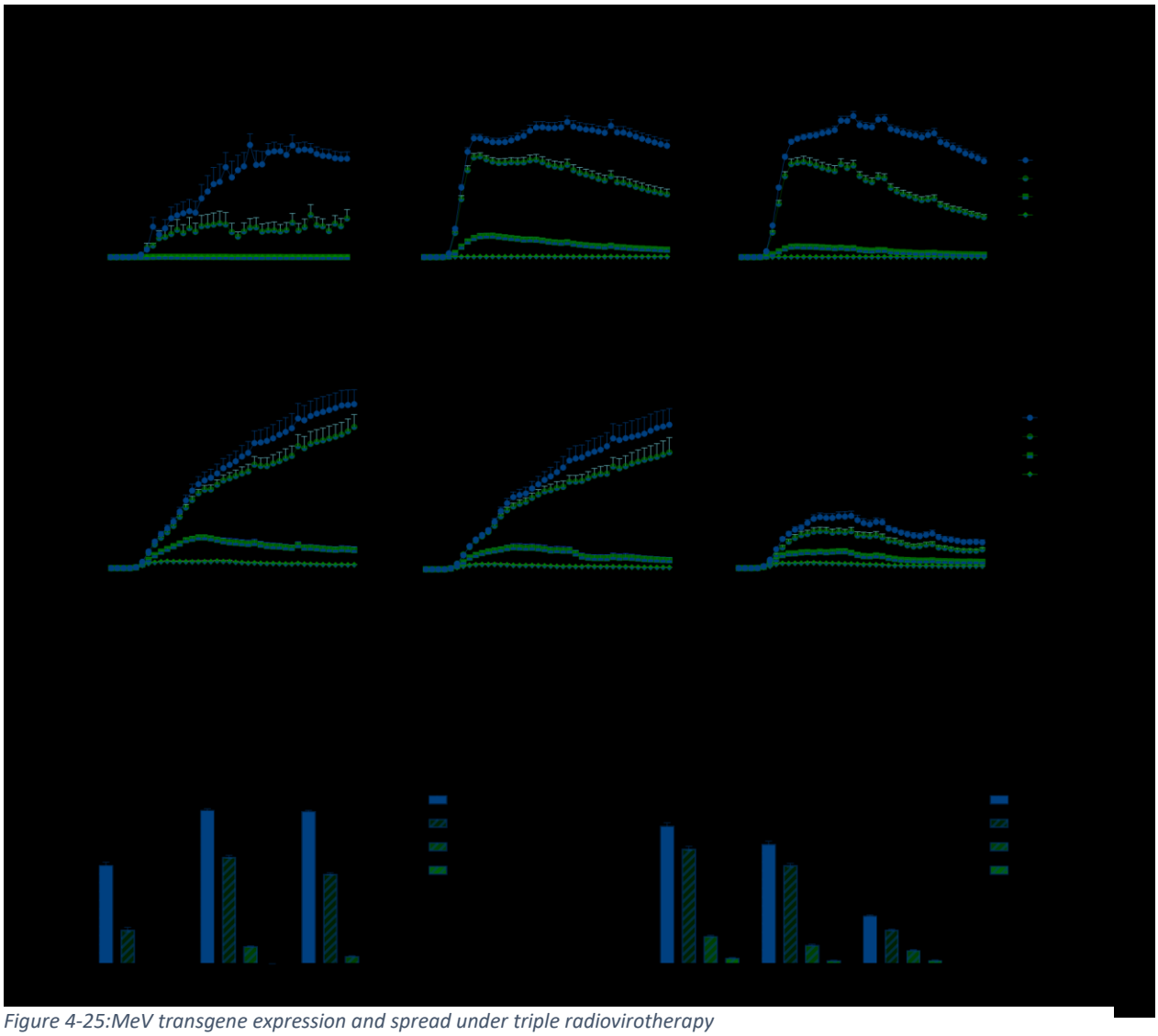

Figure 4-25:MeV transgene expression and spread under triple radiovirotherapy

I treated U251 and BxPC-3 with triple radiovirotherapy and placed the plates in an IncuCyte to image every 4 hours over the course of 7 days. I used the Incucyte Software to quantify phase and eGFP area. I plotted eGFP area normalized to phase area against the time p.tr. (A). For statistical analysis, I calculated the AUC and compared between treatment groups by two-way ANOVA with Tukey's multiple comparison test (B). * - selected significances; AUC - Area under the curve; PV - Parvovirus; MeV - Measles virus; MOI - multiplicity of infection

4.4.3.3. Translational Shutdown

A common marker for translational shutdown is phosphorylation of the α-subunit of the eukaryotic initiation factor 2 ((p)eIF2α). To investigate this in the context of dual viro- or triple radiovirotherapy, I performed western blot analysis of the most common phosphorylation site, a serine at position 51 of eIF2α. However, I did not observe any increase in pEIF2α (**Figure 7-12**). I did observe a band at 38 kDa, which reflects the correct size of the target protein. However, no increase in band intensity was observable with virus infection or under treatment with the positive control, tunicamycin, compared to untreated

cells. In general, the detection of pEIF2a by western blot was difficult. To generate the image of the depicted membrane and observe any signal at the expected height, I exposed it for 50 mins. Possibly, this extended exposure time resulted in detection of background binding to non-phosphorylated EIF2a. With these technical difficulties, I was not able to draw conclusions on whether increased pEIF2α was present and whether translational shutdown could be the cause of the observed PV-mediated decrease in MeV transgene expression.

In a second attempt, I aimed to assess the protein synthesis rate using the Surface sensing of translation (SUnSET)-assay. To this end, I treated cells with dual virotherapy and added puromycin 15 minutes prior to harvesting the cells. The aminonucleoside puromycin is incorporated into nascent proteins and can subsequently be detected through western blot analysis. The band intensity is then a direct marker of the current protein synthesis rate within the cells (**Figure 7-13**). For U251 cells, the band intensity of puromycilated proteins varied in no observable pattern related to the treatment: Certain samples showed no incorportation of puromycin. The strongest signal, indicating the highest synthesis rate, was observable with the combination of an MOI of 0.1 for MeV with an MOI of 20 for PV. The weakest band, on the contrary, was observable in the combination of an MOI of 1 for MeV and 0.2 for PV. In BxPC-3 cells, the signal was more uniform: All conditions showed incorporation of puromycin. In these cells, PV-monotherapy elicited an increased signal with all other conditions showing a similar band intensity. This was not in line with the observations of the eGFP signal decreasing in dual-virotherapy treated cells.

All in all, technical difficulties with both assays limited the interpretability of the results. Neither p-eIF2α detection nor the SUnSET assay provided consistent or conclusive evidence, and thus no firm conclusions could be drawn regarding translational shutdown as a mechanism for the PV-mediated reduction in MeV transgene expression.

4.4.3.4. *Immunogenic cell death*

A proposed mechanism for the synergy of MeV and radiotherapy was the induction of immunogenic cell death (ICD). Here, enhanced levels of extracellular calreticulin (CALR), a well-established marker of ICD, were detected in combination-treated cells. I thus also assessed extracellular CALR in the triple radiovirotherapy setting via immunofluorescence (IF) staining (**Figure 4-26**).

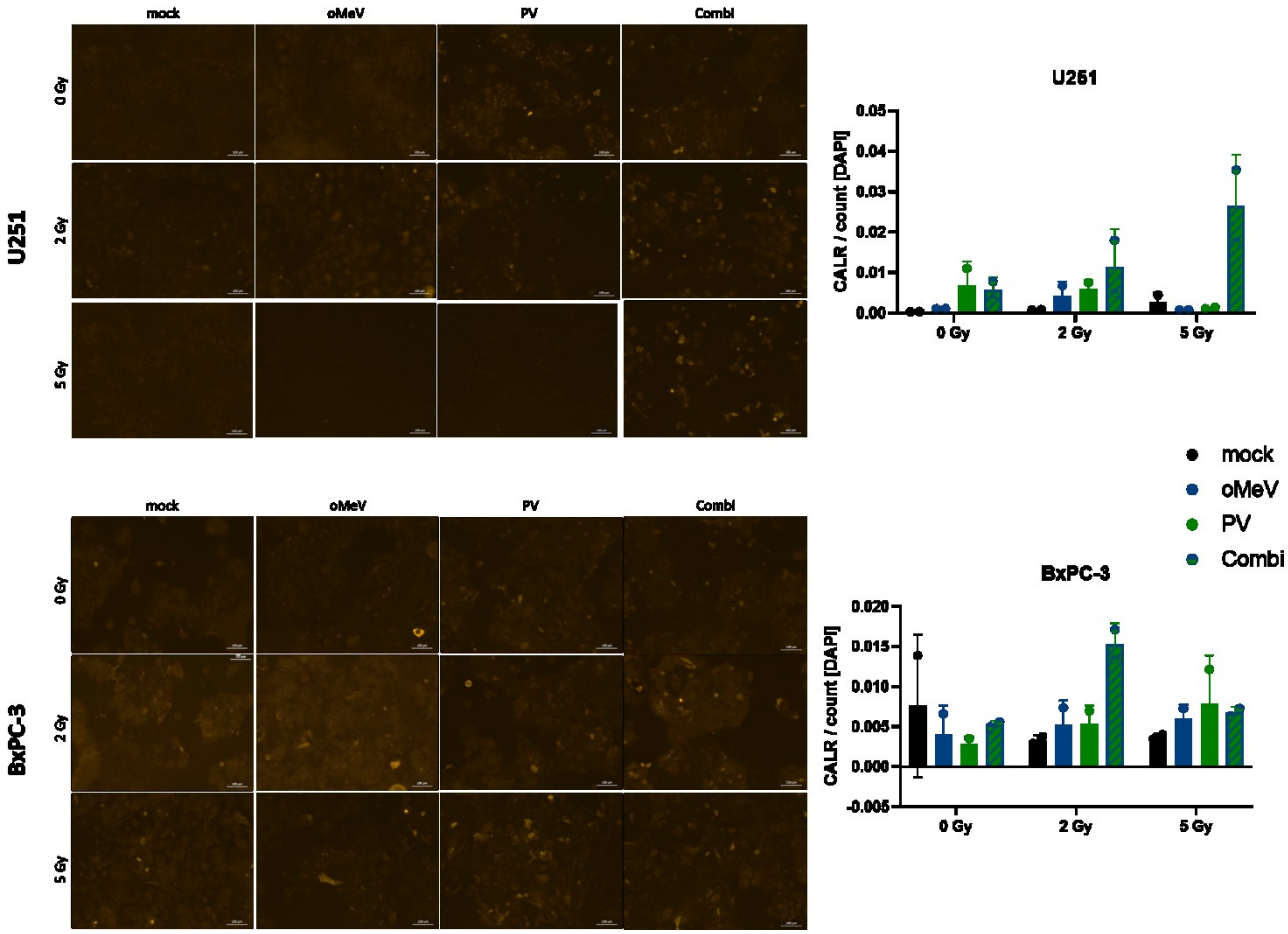

Figure 4-26: Immunofluorescent staining of extracellular calreticulin under triple radiovirotherapy

I stained cells 48 h p.tr. with triple radiovirotherapy with a CALR-specific antibody. I stained nuclei with Hoechst. I acquired images with a fluorescence microscope. Only CALR channel (detected by secondary antibody conjugated to Alexa Fluor 594) is depicted here. For quantification, I normalized the signal in CALR channel to cell number of the same image frame via the Hoechst stain. N= 2 independent experiments, mean and standard deviation is shown; scale bar = 100 µm. Images acquired with Zeiss Cell Observer with Colibri.2 module

I could detect extracellular CALR in both cell lines. However, the fluorescent signal was weak and I thus increased exposure time, which also resulted in a higher background signal. Nevertheless, foci of CALR signaling can be observed in the images. Especially in U251 cells, these foci are more pronounced in the samples infected with both viruses.

I quantified the signal using FIJI and grey-scale conversion of the single-channel images. I normalized the fluorescent intensity of the CALR channel to nuclei count. For U251 cells, the strongest CALR signal is detected in the combination of 5 Gy irradiation with both viruses. BxPC-3 cells show the strongest signal in the combination of the two viruses with 2 Gy irradiation.

While these results might indicate enhanced levels of ICD in the combination-treated samples, the high background and variance between replicates make a strong deduction on the mechanistic implication difficult.

4.4.4. Advanced models

For a final assessment of triple radiovirotherapy, I wanted to employ more advanced models to capture the complex interaction of a triple combination approach with the tumor microenvironment and host immune system. To this end, I used heterotypic PDAC spheroids to recapitulate the three-dimensional architecture and stromal–tumor interplay characteristic of PDAC more accurately. Additionally, I generated murine cell lines suitable for assessment of triple radiovirotherapy in syngeneic murine models.

4.4.4.1. Spheroids

The spheroid model previously employed in the dual virotherapy context was again provided by Assia Angelova and her team. I treated spheroids with the triple combination regimen, in accordance to the schedule described earlier. I measured cytotoxicity with the CellTiterGlo® 3D assay (**Figure 4-27**).

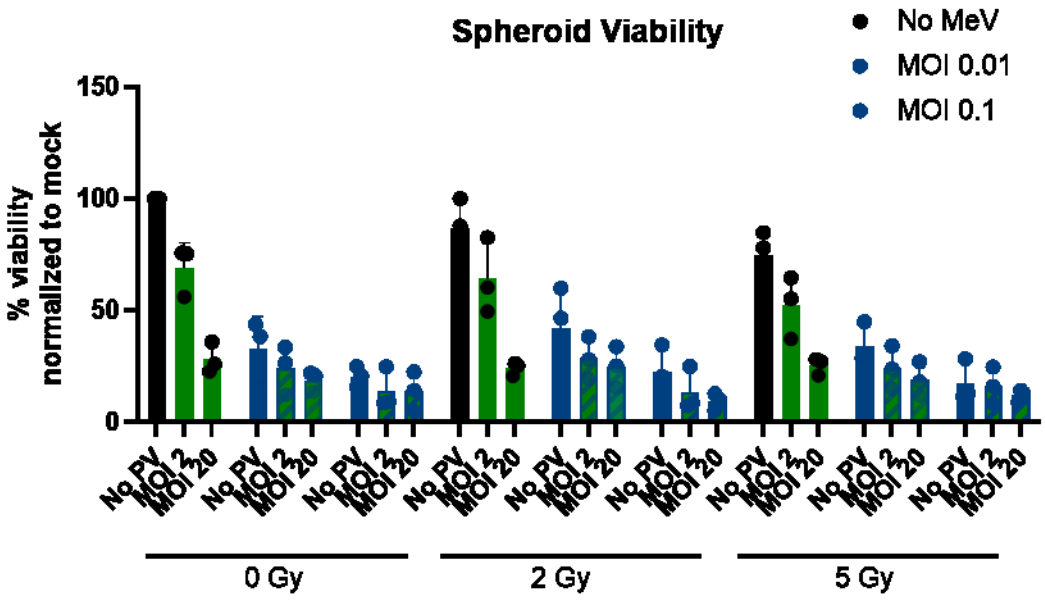

Figure 4-27: Heterotypic PDAC spheroids as 3D model to assess cytotoxic effects of triple radiovirotherapy

Heterotypic spheroids, comprised of PDAC cells, endothelial cells and fibroblasts, were provided by Assia Angelova and her team. I performed triple radiovirotherapy and measured cytotoxicity with the CellTiterGlo® 3D assay 5 days p.tr. N=3 biological replicates; mean and standard deviation is depicted. PV – Parvovirus; MeV – Measles virus; MO – Multiplicity of infection

All three monotherapies elicited a cytotoxic effect, showing cell viability of 26 %, 21 % and 75 % in response to the highest dose of PV, MeV and radiotherapy, respectively. Spheroids were especially sensitive to MeV infection, the MOI of 0.01 reduced cell viability to 33 %. At lower viral doses, toxicity was slighty enhanced by addition of the other virus. Radiation did not further enhance the cytotoxic effect. All in all, the triple combination did not yield significant improvements in regard to cytotoxicity.

For robust synergy calculation, I further extended the dose range, applying 5 viral doses and 4 radiation doses. Additionally, I extended the incubation time until cytotoxicity measurement to 15 days to allow for multiple rounds of infection for the low virus doses applied. I measured cytotoxicity with CellTiterGlo® 3D assay (**Figure 4-28 A**).

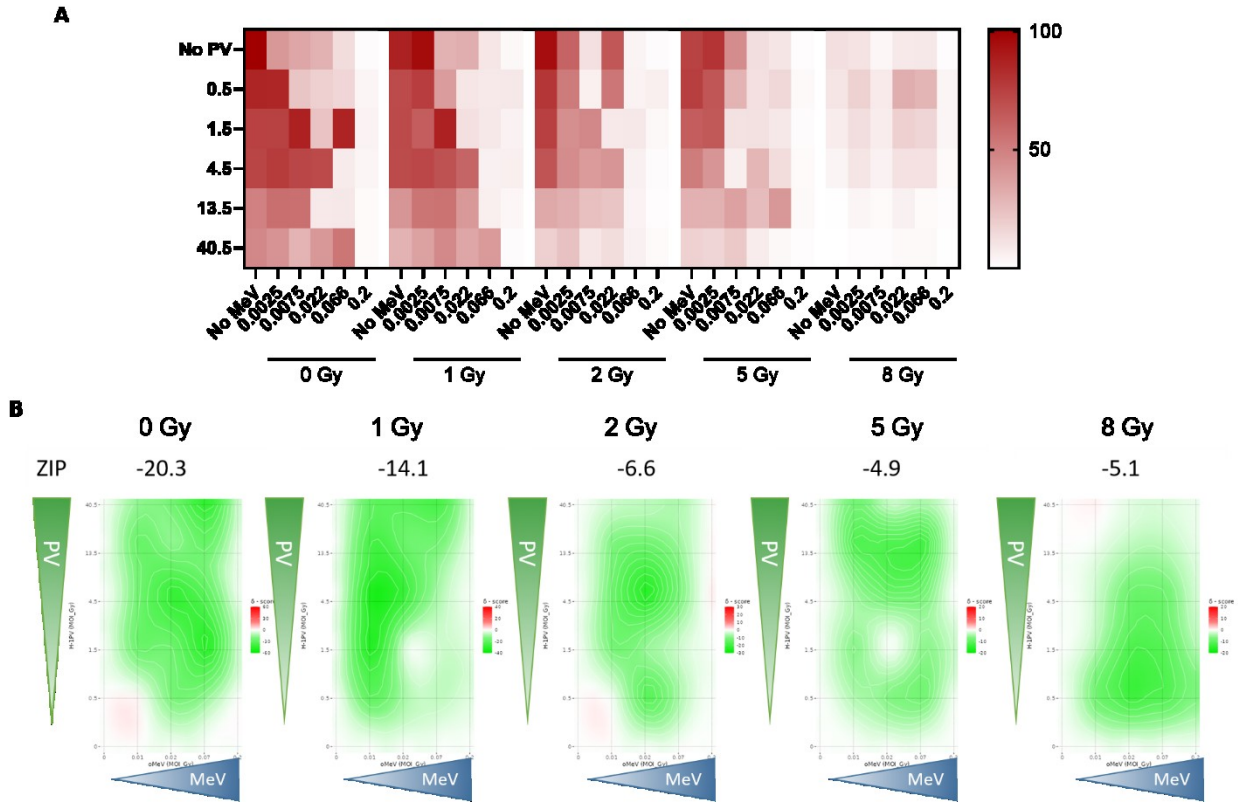

Figure 4-28: Extended dose range and synergy calculation for PDAC spheroids

I treated PDAC spheroids with triple radiovirotherapy with extended dose combinations, ranging from 1-8 Gy for radiotherapy, MOI 0.5 to 40.5 for PV and MOI 0.0025 to 0.2 for MeV. 15 days p.tr., I analyzed cytotoxicity with CellTiterGlo® 3D assay (A). Based on the cytotoxicity data, I calculated synergy using the ZIP model in SynergyFinder3.0. Negative values (green) indicate antagonism, values around 0 (white) indicate an additive effect, positive values (red) indicate synergy (B). N=3 technical replicates

MeV induced a pronounced cytotoxic effect in spheroids, reducing cell viability to approximately 40% even at the lowest MOI tested. Spheroids also displayed sensitivity to high-dose irradiation, with cell viability reduced by 90% at 8 Gy. PV treatment resulted in dose-dependent toxicity, although cell viability remained at about 45% at the highest PV dose. Interestingly, the combination of MeV and PV reduced the cytotoxic effect observed with MeV alone, and intermediate viral doses resulted in nearly 70% cell viability 15 days post-treatment. Only the highest MeV dose consistently eradicated cell viability. This observation appeared specific to combination of the two viruses, as the dose effect of the triple combination remained stable at the higher radiation doses.

In line with these observations, the synergy analysis with the ZIP model of synergy in SynergyFinder3.0 revealed highly antagonistic synergy scores for the two viruses with no or low radiation. Increasing irradiation doses slightly improved the scores, reaching values around –5; however, the interaction remained within the antagonistic range (**Figure 4-28 B**).

I also observed spheroid integrity in phase-contrast microscopy and MeV-encoded eGFP through fluorescent microscopy (selection of dose combinations in **Figure 7-14**). Similar to the observations in the monolayer setting, I saw inhibition of MeV transgene expression in presence of PV. On day 6, the eGFP expression was unchanged in irradiated spheroids. On day 12, only MeV monotherapy showed sustained eGFP signal. However, the cytotoxicity measured 2 days later showed only 12 % survival in the 5 Gy and MeV combination, compared to 30 % in the MeV monotherapy. Thus, the observed radiotherapy-mediated reduction in eGFP signal could also caused by increased cytotoxicity.

Overall, the analysis of extended dose combinations of triple radiovirotherapy in PDAC spheroids demonstrated a negative impact of adding PV to the radiovirotherapy regimen. The timing of cytotoxicity measurements appeared to strongly influence the outcome: at 5 days post-treatment, the combined cytotoxicity was modest, but limited additive effects were observable. Over time, however, spheroids appeared to recover from PV-mediated cytotoxicity, which in turn diminished the cytotoxic effect induced by MeV.

In addition to the cytotoxicity analysis, I analyzed *IFNB1* induction on the transcript level and release of CXCL10 in spheroids under triple radiovirotherapy. I performed these analyses on spheroids 72 h p.tr. (**Figure 4-29**)

On the transcript level, PV alone had no effect and radiation only slightly induced *IFNB1*. MeV, on the other hand, dose-dependently induced *IFNB1* up to 700-fold. The dual virus combination still elicited an increase, compared to mock or radio and PV monotherapy. Low-dose PV further elevated the IFNB1 fold change (not significantly, but reproducibly across MeV and radiation doses), while high-dose PV slightly dampened the *IFNB1* induction. The reduction was only significant in the comparison of low-to high dose PV at the highest radiation and MeV dose. All in all, the effects of triple radiovirotherapy on *IFNB1* signaling on transcript levels were comparable with the observations in dual virotherapy and the monolayer setting.

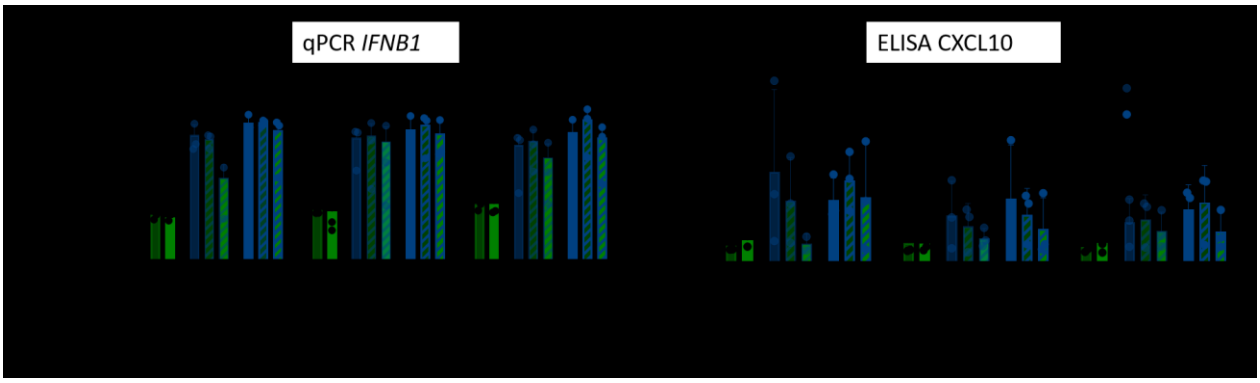

Figure 4-29: IFN signaling in 3D PDAC spheroids under triple radiovirotherapy

I harvested spheroids and their supernatants 72 h after triple radiovirotherapy. (A) I isolated RNA and performed RT-qPCR to analyze transcript levels of *IFNB1*. $2^{-\Delta\Delta Ct}$ values, normalized to *ACTB* is depicted. (B) I performed ELISA to measure CXCL10 in the supernatant of spheroids. N=3 biological replicates for both experiments. Mean and standard deviation is depicted. Stefanie Sawall performed one replicate of CXCL10 ELISAs.

I assessed CXCL10 release by the spheroids under triple radiovirotherapy by ELISA. Neither PV nor radiation led to an increase of CXCL10 in the medium, compared to untreated spheroids. On the contrary, MeV-mediated CXCL10 release was detectable. Interestingly, for the lower MeV dose, PV treatment reduced CXCL10 release dose-dependently. That effect was stronger with no or low-dose irradiation. For the higher MeV dose, the effect of PV addition was variable: No difference was observable in non-irradiated cells, a PV dose-dependent reduction was observable in cells irradiated with 2 Gy and only the high PV dose reduced CXCL10 release in cells irradiates at 5 Gy. However, none of these effects reached statistical significance and variance between replicates was high.

Taken together, IFN and downstream effector signaling was mainly MeV-driven, also in the spheroid context. The addition of PV modulated the response at certain dose combinations but only to a limited degree and mostly without reaching significance.

The synergy of triple radiovirotherapy that I observed in U251 cells was not present in the spheroid model. While combined cytotoxic effects of the three treatment modalities could be observed, this was restricted to a limited number of dose combinations and only observable at an early time point p.tr. Equally, the mechanistic analysis of *IFNB1* and CXCL10 did not reveal a strong and reproducible effect of the triple combination.

In the spheroid model, PDAC cells, endothelial cells and fibroblasts could contribute to the observed IFN signaling and CXL10 release and express eGFP through MeV infection. To shed light on what cell type within the spheroid is susceptible to MeV and elicits the IFN induction, I analyzed MeV infection and IFN signaling in the heterotypic triple spheroids and the respective mono-spheroids of AsAN-PaCa, HUVEC and MRC-5 cells (**Figure 7-15** and **Figure 7-16**).

I microscopically observed the eGFP signal in MeV-treated spheroids 72 h post infection (**Figure 7-15**). In triple and tumor spheroids, I observed eGFP signal. In tumor spheroids, the signal appeared stronger and more foci of eGFP signal were observable. In MRC-5 and HUVEC spheroids, on the other hand, no foci were present within the dark spheroid mass. Only background eGFP, likely from the viral stock solution the spheroids were treated with, can be seen.

In addition, I analyzed *ACTB* and *IFNB1* transcripts in triple and mono-spheroids (**Figure 7-16**). *ACBT* transcripts could be detected in all four spheroid types, resulting in exponential increase of signal in the amplification curves and a specific peak in the melt curve analysis. Analysis of *IFNB1,* on the contrary, only revealed a signal in triple spheroids and tumor cells. The exponential increase in MRC-5 and HUVEC samples in the amplification plot occurred after more than 30 cycles and the melt peak analysis showed off-target peaks. Two peaks appear around the temperature that would be specific for *IFNB1* transcript. These were likely carry-overs from other wells and only present in one of three technical replicates.

The analysis of monotypic spheroids strongly suggested that only the tumor cells are susceptible to MeV infection and contribute to the IFN response observable in the spheroid model.

4.4.4.2. Generation of murine tumor models

MeV is strongly host-restricted and requires the expression of certain entry receptors to infect a cell. In the context of oncolytic virotherapy with MeV, the most important entry receptor is hCD46, being overexpressed by a variety of human tumor entities. Mice are not a natural host of MeV and it is thus necessary to generate murine cells stably expressing hCD46 to test MeV in mouse models. To this end, I lentivirally transduced murine GBM and PDAC cell lines to allow for subsequent in vivo experiments of triple radiovirotherapy in immunocompetent mouse models of these entities.

I used murine cells with a C57Bl/6 background, namely GL261 (GMB), PDA30364 and m24192 (both PDAC). After lentiviral transduction, I performed single cell or bulk sorting on CD46-positive cells and expanded the derived clones. I then assessed hCD46 expression via flow cytometry and susceptibility to MeV infection, comparing the transduced clones to their parental counterparts (**Figure 4-30**).

Analyzing the transduced clones by flow cytometry after staining with a hCD46 antibody revealed that all cells expressed hCD46, while the parental counterparts did not. The degree of hCD46 expression differed markedly between clones: Some had a uniform and high expression, others clones had a more heterogeneous population. This pattern remained stable after 2-3 months in culture (data not shown).

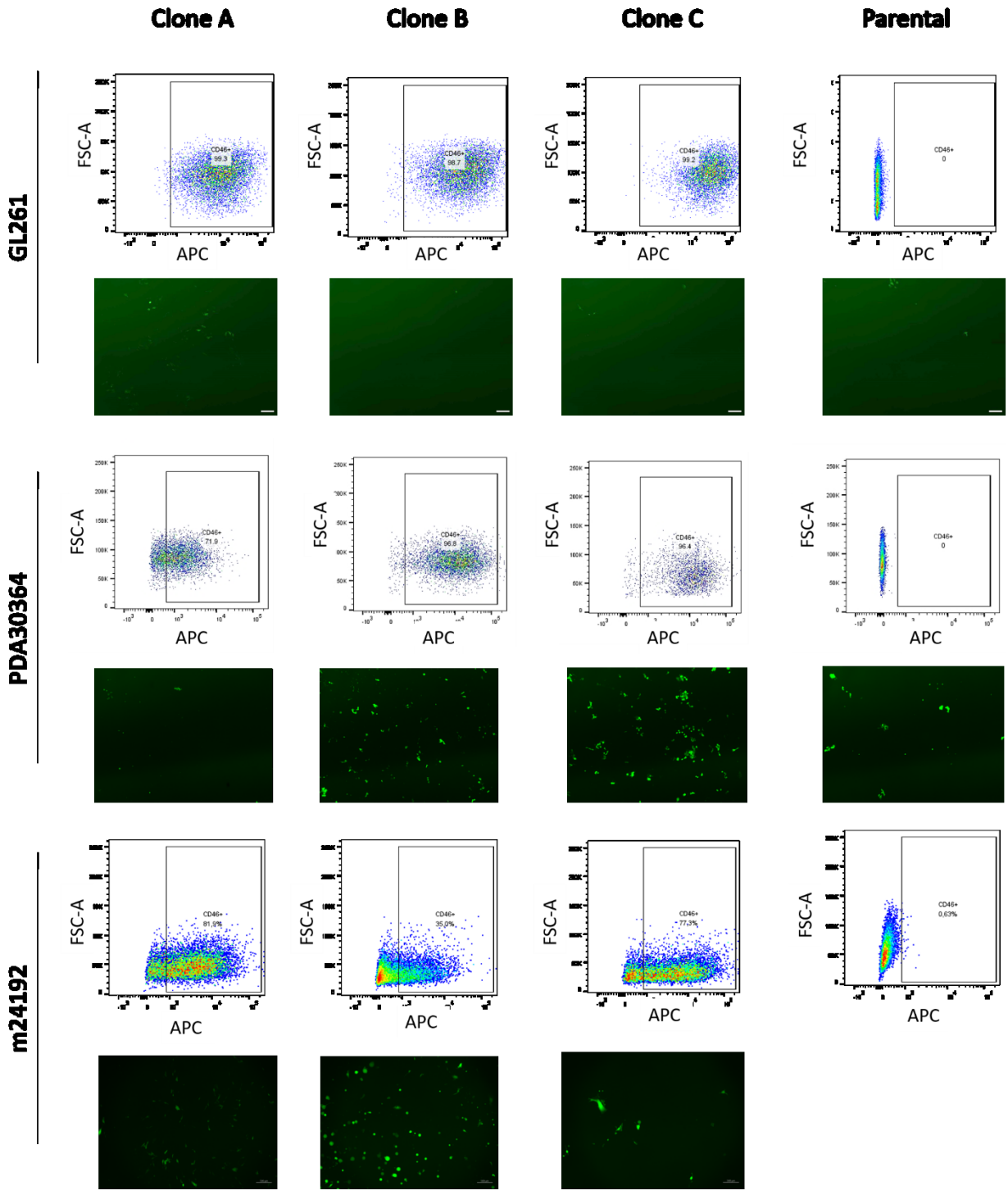

Figure 4-30: Generation of murine cell lines stably expressing hCD46

I lentivirally transduced the murine cell lines GL261, PDA30364 and m24192 to express MeV entry receptor hCD46. I single-cell and bulk sorted CD46-positive clones and characterized the expanded cell populations for presence of the transduced receptor by flow cytometry. Additionally, I observed susceptibility to MeV. I infected the clones with MeV encoding for eGFP and microscopically observed eGFP signal 72 h post infection. Parental, non-transduced cells were used as a control in both experiments.

To assess MeV susceptibility of the transduced clones, I infected them with MeV encoding for eGFP and observed eGFP expression by fluorescence microscopy 72 h post infection. eGFP expression differed between clones and cell lines. MeV infection in GL261 cells was very limited, neither the parental cells nor the hCD46-transduced clones showed high levels of infected (eGFP-expressing) cells. PDA30364 cells, on the other hand, were rather susceptible to MeV infection, even without hCD46-transduction. The parental cell line showed eGFP expression, which was further enhanced, at least in two of three clones, in transduced clones. m24192 cells also showed variable levels of MeV infection. While I did not asses the parental susceptibility to MeV in this cell line, the three tested transduced clones range from very limited (clone A) to high levels of infection (clone B).

Interestingly, the degree of hCD46 expression did not correlate with MeV susceptibility. Certain clones showed a population of high hCD46-expressing cells, but low or no MeV infection (all clones for GL261, clone A for m24192). This underlines that additional factors may contribute to the degree of MeV susceptibility.

In parallel to my establishment of hCD46 expressing murine cell lines, these cell lines were tested *in vitro.* For all experiments in preparation for animal experiments employing murine cell lines, the *rodent Protoparvovirus* minute virus of mice (MVM) was used, instead of the *rodent Protoparvovirus* H-1PV, which was used in all experiments involving human cell lines. MVM was evaluated in terms of susceptibility in PDAC cell lines, (work done primarily by Assia Angelova) and efficacy of combination with radiotherapy in the GBM cell line (work done by Laurent Daeffler). Neither PDAC cell line showed high sensitivity to treatment with MVM. While I saw expression of viral NS1 protein in m24192 cells after MVM infection (**Figure 7-17**), Assia Angelova observed very limited cytotoxicity of PV in PDA30364 and m24192, even in response to high MVM-doses (data not shown). GL261 cells, on the other hand, showed promising combined cytotoxic effects of radiotherapy and MVM (data not shown, work performed by Laurent Daeffler). It was thus decided to perform animal experiments with the GL261-hCD46 model. The animal experiments are currently ongoing in the lab of Laurent Daeffler and are not part of my thesis work.

5. Discussion

Notoriously refractory cancer entities such as PDAC and GBM require novel therapeutic approaches, especially in an aging society where cancer incidences in general and of these entities in particular, are rising.[153,154] In this thesis, I explored one such novel approach: The combination of radiotherapy and the oncolytic viruses parvovirus and measles virus.

There is preclinical evidence for the benefit of combining parvo- (PV) or measles virus (MeV) with radiotherapy, individually. Radiotherapy combined with PV elicited enhanced cytotoxicity in radioresistant glioma cells lines.[155] *In vitro*, the combination of MeV and radiotherapy elicited enhanced cytotoxicity in several cell line models [133-136] and was accompanied by enhanced levels of apoptosis, viral replication and (innate) immune induction. *In vivo*, the combination equally elicited benefits in xenograft[133] and immunocompetent[135] mouse models. Since innate immune activation restricts MeV replication, but was increased in the combination with radiotherapy, I hypothesized that a triple combination approach could further enhance therapeutic efficacy through PV-mediated transient IFN suppression. I comprehensively assessed this in the thesis presented here.

5.1. Laying the base: RNA sequencing and model selection

To generate a more complete picture of the transcriptomic alternations induced in the combination of MeV and radiotherapy, I performed RNA sequencing on U251 glioma cells, comparing mock-, mono and combination-treated conditions.

The transcriptional pattern induced was distinct between treatment groups. Interestingly, MeV infection did not induce the highest number of genes (**Figure 4-1B**,) but did so very reproducibly and robustly: The top 50 differentially expressed genes (DEGs), sorted by false-discovery-rate (FDR) were all MeV-induced (**Figure 7-1**), in contrast to just over half (33/50) in the top 50 DEG sorted by log2FC (**Figure 4-2**). This underlines the canonical, well-orchestrated gene induction that occurs upon viral infection.[156]

Among the top 50 DEGs only a single one was downregulated (**Figure 4-2**): RP11-496D24.2, a long non-coding RNA (lncRNA). Its differential expression has been reported in several cancer-related RNA sequencing datasets.[157,158] lncRNAs are important regulators of gene expression and may act on DNA, RNA and protein level with diverse functions and disease-associations.[159] Interestingly, RP11-496D24.2s differential expression had diverse functional interpretations: Yuan *et al.* found expression of the lncRNA associated with a favorable prognosis in tripe negative breast cancer.[158] On the contrary, Huang *et al* found high expression of this lncRNA associated with poor prognosis in papillary renal carcinoma.[157] Their data

suggest an interaction of the lncRNA with several common microRNAs (miRNAs) miRNA-145[160], miRNA-211[160], mir-216a[161] and miRNA-217[162]. Notably, all four miRNAs have been associated with tumor suppressor function in glioma cell lines or patient samples.[160-163] While the functional consequence or degree of interaction between RP11-496D24.2 and those miRNAs has not been investigated yet, the out layer role this transcript showed in my RNA sequencing dataset could make it an interesting target to investigate further.

The most common characteristic of the upregulated genes among the top 50 DEGs was their association with the immune response. This was not restricted to the virus-mediated upregulation, but also observable in the radiotherapy-induced genes. Conversely, the gene ontology (GO) and gene set enrichment analysis (GSEA) revealed mostly immune pathways as positive correlates (**Figure 4-3 A and B**, respectively). Surprisingly, no upregulation of DNA damage response or other radiotherapy-associated markers was observable. Possibly, the time-point of sample-collection conferred a bias towards virus-mediated effects: I collected RNA 48 h after completion of treatment, thus 72 h after irradiation. Typically, earlier time points up to 24 h post irradiation are analyzed and show the induction of DNA damage response[164,165], which is an early event after exposure to ionizing radiation.[166,167] In future experiments, sampling across multiple post-treatment time points could help disentangle the kinetic interplay between radiation- and virus-induced signaling.

Nevertheless, the high degree of immune activation I observed in the combination-treated condition supports the hypothesis to transiently dampen the IFN response to boost therapeutic efficacy of radiovirotherapy.

To address this hypothesis, I screened a panel of PDAC and GBM cell lines to identify those with strong intrinsic IFN responsiveness (**Figure 4-4, Figure 4-5, Figure 4-6, Figure 4-7**). U251 cells showed the most robust induction of IFN signaling across the cell line panel. BxPC-3 and T3M4 cells also showed a coherent induction on both transcript and protein level. U87 and U373, on the other hand, showed differences. U87 cells had induction levels comparable to those of the other cell lines in RT-qPCR experiments. However, neither induction of STAT1 nor ISG15 was visible in western blot analysis. U373, on the other hand, showed similar levels of the transcripts measured in response to both MeV and poly(IC), but protein induction only occurred in response to poly(IC), not MeV. Discrepancy between mRNA and protein levels are well-described and established.[168] The data presented here again underlines the need to take both into account when deducting information on cellular signaling patterns.

The final part of the screen was the analysis of susceptibility to MeV. As described in the literature, MeV replication is restricted in cells with high baseline levels of IFN signaling.[169] In line with this, U87 and U373 cells showed limited induction of STAT1 and ISG15 in response to MeV infection on the protein level and comparably high MeV permissiveness, even when pretreated with IFN-β. On the contrary, T3M4 cells showed consistent induction of IFN signaling on transcript and protein level in response to MeV, yet remained highly permissive and supported the fastest MeV replication among all tested lines. Prior reports testing the susceptibility of PDAC cell lines to vesicular stomatitis virus (VSV, a negative stranded ssRNA virus, such as MeV) showed that only constitutive high expression of certain, selected Interferon stimulated genes (ISG) predicted the resistance of certain cell lines to the virus, while IFN-α and IFN-β was detected across susceptible and resistant cell lines.[170] This underlines the complexity of the IFN response and the effector function it entails. Further analysis of additional ISGs and effector proteins is needed to clarify this relationship.

For U251 and BxPC-3 cells, again, the reduced replication capacity of MeV that was observable in the viral growth curve (**Figure 4-8**) aligned with the IFN-signaling induction capacity. Both cell lines also showed severely reduced levels of MeV genomes when pretreated with recombinant IFN-β (**Figure 4-9**) and were thus selected as the candidate cell lines for the subsequent analysis of dual and triple (radio)viroherapy.

5.2. Dual virotherapy

In the work presented here, I assessed the combination of two oncolytic viruses, parvovirus and measles virus to prepare for the triple combination approach with radiotherapy. The cytotoxic effect of the dual virus combination compared to the monotherapies was slightly enhanced for some dose combinations. I did not observe robust synergy, rather the combined effect remained in an additive range (**Figure 4-10**, **Figure 4-11**).

Several approaches have so far been taken to assess the combination of two oncolytic viruses (reviewed partly in [94] and [121]). The rationale is the expansion of susceptible tumor cells when applying viruses of different oncotropisms[171], prevention of treatment resistances[172] or modulation of the immune induction[173]. Alkassar *et al.* demonstrated that combining reovirus with newcastle disease virus (NDV) or parvovirus showed synergistic tumor cell killing in GBM models *in vitro* and in xenograft models *in vivo.*[174] On the contrary, they observed that the combination of PV and NDV (a member of the *Paramyxoviridae* family, which MeV also belongs to) was antagonistic. Notably, Alkassar *et al.* used U87 and U373 cells, both part of my initial cell line screening. In my analyses, these lines displayed minimal induction of virus-mediated interferon (IFN) signaling. Consequently, I focused on the highly IFN-competent U251 cells as a

more suitable model to test the hypothesized benefit of transient IFN suppression by PV (**Figure 4-6**). When I performed triple radiovirotherapy in U87 cells, the synergy scores were within the antagonistic range, consistent with the findings of Alkassar *et al.* (**Figure 4-22**). Since both NDV and MeV are IFN-sensitive viruses[74,175] these results align with my initially hypothesized mechanism and emphasize the importance of careful model selection for the specific biological hypothesis under investigation. Recently, most OV combination studies have focused on exploiting a vaccine effect in prime-boost settings. Taha *et al* showed that encoding a truncated tumor-associated antigen (TAA) with one oncolytic vector and subsequently targeting it with a second OV encoding a bispecific T cell engager (BiTE) yields significant therapeutic benefit in advanced *in vivo* models of disseminated disease.[176] Prime-boost approaches are also tested clinically (NCT02285816, NCT02879760) employing adenoviruses and oncolytic maraba viruses, but no results have been published so far.[177] Similar approaches including therapeutic transgene delivery is not feasible in the combination of MeV and PV, since the very condense genome organization of PV restricts its transgene capacity.[81]

5.2.1. Viral interference? PV-mediated MeV transgene suppression

I repeatedly observed the striking PV-mediated reduction of the MeV-encoded eGFP transgene in dual and triple combination approaches (**Figure 4-14**, **Figure 4-25**). It is well established that viral infections induce an integrated stress response (ISR) and subsequent translational shutdown through eIF2α phosphorylation.[178] This also been described for *Protoparvovirus* strains, used in this study.[179] To investigate whether this explains the observed MeV transgene reduction, I analyzed phosphorylated eIF2α levels and global protein turnover in PV- and MeV-treated cells (**Figure 7-12**, **Figure 7-13**), but found no supporting evidence for ISR-mediated translational inhibition as the underlying cause. Other explanations must therefore be considered. Coinfections with two viruses is a common natural occurrence and can have distinct interaction patterns: “Interference, synergy, noninterference, dependence assistance, and host-parasite relation” as summarized by Du *et al*.[180] Interference describes the suppression of the replication of one virus by another virus. Strikingly, I did not observe an effect on MeV titers and genome transcripts or PV protein expression (**Figure 4-13**, **Figure 4-23** and **Figure 4-24**). The effect I observed was thus restricted to the MeV-encoded eGFP. One plausible reason could be enhanced competition for cellular resources when two viruses coinfect a cell. Viruses, intrinsically dependent on the cellular translation machinery, have co-evolved to maximize viral protein expression even during active ISR.[181] For example, viral codon usage is distinct from the host mRNA’s and altered tRNA pools during viral infection are suggested to play a role in differential translation of viral and host proteins when an antiviral state is induced.[182] Thus, suboptimal codon usage (not optimized to cellular antiviral states) of the eGFP transgene

could contribute to its reduced expression in coinfected cells. This hypothesis could be tested by quantifying eGFP and viral mRNA compared to their respective protein levels under dual infection. Furthermore, assessing other MeV-encoded transgenes could clarify whether this suppression is specific to eGFP or reflects a broader inhibition of transgene expression in MeV–PV coinfection. Notably, simultaneous transgene expression during coinfection has been reported for other viral systems. In a study using herpes simplex virus type-1 (HSV-1) backbones encoding interleukin-12, firefly luciferase, and eGFP, no differences in transgene expression were observed when the viruses were applied concurrently.[183] This suggests that the inhibition observed in the combination approach described here is not a universal feature of viral coinfection and could be optimized when therapeutic transgenes are tested in dual or triple combination approach. Lastly, technical assay-specific artifacts could cause similar observations. However, I observed the described effect reproducibly across assays and replicates. I thus believe that the observations have a biological cause and should be investigated as such.

In summary, while ISR-mediated translational shutdown could not be confirmed in my thesis as a cause, the PV-induced suppression of MeV-encoded eGFP likely arises from virus-specific interactions that alter translational efficiency or transgene compatibility. This underscores the complexity of designing therapeutic approaches combining multiple viral vectors.

5.3. Triple radiovirotherapy *in vitro*

The ultimate aim of my thesis was to investigate the triple combination of radiotherapy with oncolytic parvo- and measles virus. The rationale was to employ PV to transiently dampen IFN signaling, which is upregulated in the combination of MeV and radiotherapy. I hypothesized that this would enhance MeV replication, ultimately resulting in a favorable immune induction pattern. I did observe a therapeutic benefit, especially in the GBM cell line U251 (**Figure 4-18**, **Figure 4-19)**. This was accompanied by PV-mediated reduction of immune induction, especially on the level of secreted cytokines. While no effect on MeV or PV replication was observable in the triple combination approach (**Figure 4-23**, **Figure 4-24**), the extracellular expression of ICD marker calreticulin was enhanced. The latter effect was more consistent in U251 than BxPC-3 cells (**Figure 4-26**).

While a triple combination has, to my knowledge, never been tested before, several previous studied have analyzed the combination of MeV, PV or other OVs with radiotherapy. The rationale for combined radiovirotherapy is manifold and includes enhanced immune induction through anti-viral IFN signaling as well as ICD[134], enhanced viral replication[155], synergistic induction of DNA damage[155,184], as well as radiosensitizing properties of the virus[133,155] or transgenes encoded on the virus[185]. In case of MeV, a

common approach for radiovirotherapy is to virally encode a sodium iodide symporter (NIS). NIS-expression in infected tumor cells allows tumor-specific uptake of radioiodine isotopes. This offers two advantages: Viral spread can be imaged non-invasively *in vitro* as well as in animals or even patients *in vivo* when applying ^{123}I, and the combination with ^{131}I elicits therapeutic advantages including tumor regressions and local bystander effects.[185-187] While the use of radioactive iodides as radiation sources is one form of radiovirotherapy, my analyses here focused on external beam radiotherapy (EBRT) using X-rays as radiation source. Several studies have investigated MeV and EBRT in GBM models.[133,134] Rajamaran *et al* employed a triple combination approach of chemo-, viro- and radiotherapy. They observed synergistic cytotoxic effects and a potent MeV-induced type I IFN response. This is in line with the observations I made in the U251 cells (**Figure 4-19**). Notably, they analyzed the human leukocyte antigen (HLA)-ligandome and found a highly immunogenic MeV derived peptide highly enriched in the triple-combination treated cells.[134] This underlines the potential of MeV-derived radiovirotherapy for immunotherapeutic approaches. The combination of PV and radiotherapy has been tested less extensively. Geletneky *et al* showed improved cytotoxicity under radiovirotherapy, especially in radioresistant glioma culture.[155] They observed that the rate of S-Phase was higher in irradiated cells, which benefitted PV infection and resulted in higher PV protein (NS1) expression. Thus, the schedule they proposed was irradiation followed by PV infection 24 h later. The systematic analysis of combining PV and radiotherapy was not part of my thesis, but was carried out by collaboration partners in Straßbourg. They observed the contrary effect on cytotoxicity: Applying irradiation 24 h before PV infection elicited decreased cytotoxicity. Concomitant application (radiotherapy directly followed by PV infection) elicited enhanced cytotoxic effects and improved PV replication (Daeffler *et al*, manuscript in preparation). This is line with the common understanding of the effect of irradiation on the cell cycle, which is G2/M accumulation and subsequent G1 arrest.[44] Following this rationale, the application of PV 24 h after irradiation could be detrimental for the S-phase dependent virus. For the triple combination regimen described here, I therefore used the schedule proposed by Daeffler *et al* and applied PV directly after radiotherapy and infected with MeV 24 h thereafter. One possible explanation for the observed difference is the radiation dose applied: Geletneky et al irradiated the cells with single doses of 5-20 Gy. The experiments on PV and radiotherapy of Daeffler *et al* and my triple combination approach employed lower doses of 1 to 8 Gy, which is more in line with clinically applied, fractionated radiation doses. High-dose radiation induced more DNA damage, especially double-strand breaks (DSB)[188], which PV can exploit for its replication.[189] This could also have conferred the increase in PV replication Geletneky *et al* observed.

5.3.1. Mechanistic considerations: IFN signaling and beyond

In my thesis, I investigated several possible mechanisms of action for enhanced cytotoxicity of triple radiovirotherapy. Among them, enhanced or transiently suppressed IFN signaling, viral replication and the induction of immunogenic cell death (ICD).

The role of IFN signal is central to my hypothesis of adding PV to the radiovirotherapy regimen to enhance MeV efficacy. The causal link between the observed IFN modulation and the synergistic effect of triple radiovirotherapy in U251 cells therefore has to be addressed carefully. U251 showed the strongest induction of IFN signaling in response to MeV when I screened for candidate cell lines and conversely showed the strongest attenuation of MeV replication (**Figure 4-6** and **Figure 4-8**). IFNB1 and downstream signaling in dual- and triple virotherapy was significantly reduced only in U251 cells (**Figure 4-12** for IFNB1, **Figure 4-20** for CXCL10). Equally, the combined cytotoxic effect of triple radiovirotherapy was synergistic only for these cells (**Figure 4-19**.). Despite these associations, my data do not support the hypothesis that the transient IFN suppression induced by PV directly enhanced MeV replication; the magnitude of IFN attenuation appears insufficient to rescue or augment MeV spread. Aref *et al* employed "a stepwise model of cellular transformation" and showed that MeV susceptibility and cytotoxicity is highly dependent on the intrinsic IFN response of the infected cell.[190] However, even in highly transformed and IFN-deficient cells, low-dose pretreatment with IFN-β results in attenuation of MeV infection. Thus, although PV reduced IFN signaling in U251 cells and coincided with therapeutic synergy, the degree and timing of suppression were likely too modest to produce a measurable increase in MeV replication, suggesting that the observed benefit of the triple regimen arises from more complex mechanisms rather than only enhancement of viral propagation.

To further dissect the complex role of IFN signaling in triple radiovirotherapy, I applied the combination regimen to U87 and T3M4 cell, two lines characterized by low intrinsic IFN signaling capacity (**Figure 4-6**). In these models, the triple therapy resulted in an antagonistic interaction (**Figure 4-22**). While this might suggest that intact IFN signaling is important for the efficacy of triple radiovirotherapy, no causal relationship can be inferred from this correlation alone. Rather, syngeneic and stable *IFNAR* or *IFNB1* ko of U251 and BxPC-3 cells should be employed to assess the contribution of IFN signaling. Alternatively, pharmacological inhibition, for instance through JAK1 and JAK2 inhibitor ruxolinitinib, could be used for further functional analyses.

In contrast to the initial hypothesis, enhanced MeV replication could not be confirmed in the triple radiovirotherapy approach (**Figure 4-24**). Thus, the underlying mechanism of the observed therapeutic

efficacy especially in U251 cells remained unresolved. I did observe enhanced levels of extracellular calreticulin (CALR) more consistently in U251 than BxPC-3 cells (**Figure 4-26**). Extracellular exposure of CALR is defined as one hallmark of ICD, because it enhances the uptake of the (dying) cells it is expressed on by antigen presenting cells (APCs). Type-I IFNs and CXCL10 are immunostimulatory DAMPs and their release is equally linked to ICD.[191] I detected the release of these cytokines, which was mainly MeV-driven and not enhanced in triple radiovirotherapy (**Figure 4-21**). Direct cytotoxic and antiproliferative effects of IFN-β are well-described and can be studied in assays only employing cancer cells *in vitro* [192] Functional effects of enhanced ICD, on the other hand, cannot be investigated in a pure *in vitro* monoculture setting. The gold standard to confirm ICD on a functional level is a vaccination assay in immunocompetent mice: To this end, murine tumor cells would have to be treated with triple radiovirotherapy or control regimens and used as vaccines, applied *s.c.* in non-cancer bearing mice. The protective effect of the triple combination-treated "vaccine" versus the control regimens against subsequent tumor engraftment would then indicate whether the treatment indeed elicits ICD.[191] As an *in vitro* surrogate and model in the human system, dendritic-cell co-culture assays that quantify uptake of treated tumor cells and DC maturation could be employed.[191] Given that increased extracellular CALR on U251 cells following triple therapy cannot account for enhanced cytotoxicity in monoculture, the mechanistic basis for the apparent synergy of triple radiovirotherapy remains elusive in this thesis.

Several other mechanisms should be considered to elucidate molecular determinants of (synergistic) triple radiovirotherapy: My thesis focused on the role of type I IFNs, specifically IFN-β. Neither IFN-α nor type III IFNs (IFN-λs) were investigated. IFN-β is the best-described effector of antiviral signaling, especially in the context of MeV virotherapy. However, type III IFNs are increasingly investigated for their complementary role in eliciting immunomodulatory effects.[193] Type I IFNs signal trough the IFN-α/β receptor (IFNAR), ubiquitously expressed on nucleated cells. In contrast, the expression of a subunit of the cellular receptor for IFN-λ (IFNLR1) is restricted to epithelial cells. Consequently, IFN-λ effector functions are restricted to epithelial tissue.[194] Given that PDAC cells are capable of eliciting and responding to IFN-λs,[195] while GBM cells generally lack this signaling capacity, the contribution of IFN-λ could differ substantially between the U251 and BxPC-3 models examined here and should investigated further.

Beyond IFN signaling and the immunogenicity of the treatment, other mechanisms could play a pivotal role in mediating the effects of triple radiovirotherapy: The main cytotoxic effect of irradiation is the induction of DNA damage, particular DNA double-strand breaks (DSBs).[42] The investigation of DNA damage response pathways in the context of triple radiovirotherapy could reveal a mechanistic explanation for the observed therapeutic benefit. Key markers for DSBs such as phosphorylation of the histone H2AX

(γH2AX)[196] and recruitment of DNA repair mediators such as Ku70 and Ku80 can be quantified via western blot or immunofluorescence to assess the extent and kinetics of DNA repair.[197] Additionally, the accumulation of unrepaired DSBs results in apoptosis, which can be evaluated by detecting cleaved caspase-3 via western blotting, or dynamically monitored using fluorescent apoptosis dyes in live cell imaging approaches.[198] Together, these analyses could provide an in-depth understanding of the molecular mechanism underlying triple radiovirotherapy.

5.3.2. Enhancing radiovirotherapy

Together with, and in addition to, deciphering the mechanism of triple radiovirotherapy, several strategies can be envisioned to enhance therapeutic efficacy. The initial aim of my thesis was to achieve transient, tumor cell-specific dampening of the IFN response through PV infection, thereby enhancing MeV replication. While my experimental data demonstrate a modest reduction in IFN signaling, the magnitude of suppression was insufficient to boost MeV replication (see above).

Combination approaches employing systemic IFN suppressors, such as the JAK inhibitor ruxolitinib, could potentially enhance MeV replication and overall treatment efficacy. However, such strategies also carry the risk of increased treatment-related toxicity and reduced MeV oncotropism. Safety remains a central consideration for clinical translation, particularly when applying live, replicating viruses.[120] Alternative strategies could therefore be employed to achieve tumor-specific modulation of the IFN response.

Our group has recently shown that MeV can be engineered to express functional microRNAs from a universal mircoRNA expression cassette.[199] Building on this work, MeV could be modified to express microRNAs that specifically target key cellular components triggering the antiviral IFN response upon infection with RNA viruses.[200]

Beyond modulating the IFN pathway, the radiovirotherapy context opens additional opportunities for rational engineering. Kon *et al* showed that a shRNA targeting the catalytic subunit of the DNA-dependent protein kinase (DNA-PKcs), which has a central role in mediating DNA DSB repair, can be expressed from a replicating adenovirus and confer a radiosensitizing effect in vitro and in xenograft models *in vivo*.[201] Similarly, our microRNA expression cassette could be adapted to encode mircroRNAs targeting transcripts of the DNA repair machinery, such as DNA-PKcs[201], ataxia-telangiectasia mutated (ATM)[202] or Poly (ADP)-ribose polymerase-1 (PARP-1)[203].

In addition to microRNA approaches, MeV-mediated expression of radio-sensitizing proteins could be feasible: Liu *et al* recently reported an NDV engineered to express an anti-VEGFR2 single-chain variable

fragment. They observed reduced hypoxia levels in tumors and enhanced tumor cell killing in combination with radiotherapy in murine xenograft models [204] These approaches exemplify that rationale design of MeV could further enhance the therapeutic efficacy of radiovirotherapy.

Apart from engineering MeV, other triple combination approaches could provide benefits. The combination of OVs with ICIs has been tested extensively, preclinically and clinicially.[205,206] A recent clinical case report showed astonishing benefit of combining T-VEC and ICI with radiotherapy in a patient with metastatic cutaneous squamous-cell carcinoma. The patient, who has progressed under previous therapy, experienced regression in treated lesions as well as pulmonary metastases and was progression free for reported 44 months.[207] This encouraging observation highlights the potential of triple combination regimens, which could be further evaluated using MeV or PV as the oncolytic component.

All in all, these approaches underscore the potential of radiovirotherapy and should be investigated in the context of MeV- or PV radiovirotherapy.

5.4. Combinations therapies in cancer management

Combination therapies are a mainstay in clinical oncology and may reduce treatment resistances, addressing intratumoral and patient-to-patient heterogeneity. For decades, combining chemotherapeutic drugs or treatment modalities has shown clinical benefit.[208] In PDAC, combination chemotherapy regimens such as FOLFIRINOX and gemcitabine-based combinations enhances survival compared to monotherapies.[209,210] Equally, standard-of-care in GBM is a multimodal approach combining surgery, radiotherapy and chemotherapy in form of temzolomide[211]

To find novel, innovative combinations, that yield benefit to cancer patients, the typical translational cycle comprises thorough preclinical in *vitro*, followed by *in vivo* assessment and finally clinical trials. In preclinical stages, the question of synergy is often raised.

5.4.1. Synergy models and their implications for (triple) radiovirotherapy

Depending on the synergy model, different assumptions are made concerning the mechanistic interaction of the drugs combined. The main model I applied to analyze synergy throughout this thesis was the Zero interaction potency (ZIP) synergy model[212] integrated into the web applications SynergyFinder 3.0[213] and SynergyFinderPlus[214] (**Figure 4-11**, Figure 4-15, **Figure 4-19**, **Figure 4-22** and **Figure 4-28**).

The ZIP model was developed to address shortcomings of widely used models, namely the Highest Single Agent (HSA), Bliss Independence and Loewe additivity models. Especially the Loewe additivity model, the base for the Chou-Talalay median effect method[215], has routinely been applied to test the benefit of drug

combinations. All models predict the combined drug effect based on input data of dose-response to the individual monotherapies. The combined drug effect may then be equal, exceed or be inferior to the predicted effect and thus be classified as additive, synergistic or antagonistic, respectively. The HSA model simply expects the combined effect to be at least equal to the highest effect of the single agent in a combination. It is thus especially applicable in drug combinations where one drug has no cytotoxic effect on its own but may contribute to an enhanced response when used with other agents. An advantage of the model is the limited number of dose combinations required to calculate an integrated synergy score. For that reason, I initially applied the HSA model to assess the potential benefit of the triple combination prior to expanding the dose combinations tested (**Figure 7-10**). The Loewe Additivity and Bliss Independence models employ more complex mathematical modeling. Here, all applied drugs influence the predicted combined effect. The Bliss Independence model calculates the probability of two drugs eliciting the observed effect independently in a stochastic process. The Loewe Additivity model extrapolates the predicted combined effect from the dose-response curves of the individual drugs, assuming a shared or comparable mechanism of action and thus a linear dose-response ratio between the two drugs. The ZIP model integrates both principles by comparing the experimentally observed combination dose–response curve to a predicted reference curve derived from individual dose–response data under the assumption of independence. Then, the deviation (ZIP score) of the observed dose-response curve from the predicted one can be plotted in an “interaction landscape” for each dose combination, providing a comprehensive overview of synergistic and antagonistic regions. This approach extends the applicability of synergy analysis to complex or high-throughput combination screens, where interaction dynamics may vary across the dose ranges.[212]

Since I combined fundamentally distinct treatment modalities in the triple radiovirotherapy, I cannot assume a linear relation between the dose-response curves (which the Loewe additivity model does). Nevertheless, I want to observe the combined effect across a range of concentrations employing a fitted dose-response (which Bliss Independence does not). I thus believe the ZIP model is the most appropriate model to assess synergy in this setting. According to the ZIP model, among all tested combinations and cell lines, robust synergy was observed only in U251 cells under triple combination treatment. Notably, combinations of 1 and 2 Gy irradiation with intermediate viral MOIs yielded the highest synergy scores (**Figure 7-11**). From a translational perspective, these findings are particularly encouraging, as they involve dose combinations that are feasible and safe to apply to cancer patients. These dose combinations should thus be prioritized in further preclinical investigations.

However, there are important limitations to the ZIP model and its application in the context of triple radiovirotherapy. The model relies on accurately fitted dose–response curves and thus requires high-quality, reproducible input data. Viruses are replicating agents, thus determination of their active concentration is inherently more challenging than it is for chemical compounds or irradiation. Moreover, MeV preparations are not purified after production, and variability between frozen virus aliquots or preparations may affect reproducibility between experiments, leading to potential false-positive or false-negative synergy calls. Another limitation arises from the model's assumption of independence between agents. While the viruses differ substantially in their replication cycles, both depend on and compete for cellular resources for efficient replication. It is therefore unlikely that their cytotoxic effects occur in complete independence, potentially affecting the accuracy of synergy modeling.

Machine learning approaches, such as BAITSAO[216], have recently been published and advance the modelling and prediction of synergy in multi-drug combinations. Such approaches have the potential to unify models and implement more unbiased methods. This could alter the narrow definition of synergy and broaden its applicability of models to more diverse, multimodal drug combinations.

Finally, the translational significance of synergy scores themselves remains an active area of debate.[217] While synergy is straightforward to interpret when it reflects principles of synthetic lethality in the combination of chemical compounds that target distinct molecular pathways, its meaning becomes less direct when broader therapeutic modalities, such as radiotherapy and immuno- or virotherapy, are involved. In such cases, patient- or tumor-specific heterogeneity may ultimately have a stronger impact on treatment outcome than the measured *in vitro* synergy score. Incorporating these biological and translational considerations into the design of future combination strategies by employing advanced models, such as patient-derived organoids, will be essential to enhance their clinical relevance and success.

5.5. Advanced preclinical models to investigate radiovirotherapy

To optimally assess (combination) therapies for clinical trials in terms of efficacy and safety, *in vitro* and *in vivo* models with high translational relevance are indispensable. Especially in the setting of employing replicating viral agents, where the interaction between virus, tumor, and microenvironment is complex and dynamic.[218] Various models can be employed for such investigations: Patient-derived cultures[219], 3-dimensional spheroids[220], tumor organoids[221] or slices[222], as well as xenograft or immunocompetent murine models.

In my thesis, I employed heterotypic PDAC spheroids comprising tumor cells as well as fibroblasts and endothelial cells to better mimic the desmoplastic and treatment-resistant TME that characterizes PDAC.

The spheroids model was established and provided by Assia Angelova and her team. In contrast to the effects observed in 2D cultures of BxPC-3 and U251 cells, I saw a reduced therapeutic efficacy of the triple radiovirotherapy in spheroids (**Figure 4-28**). Spheroids were very sensitive to MeV treatment, but showed resistance to both radio- and PV therapy. Possibly, the fusogenic property of MeV yielded an advantage in this model. Le Boeuf *et al* showed that arming a vesicular stomatitis virus with a fusogenic protein significantly enhanced viral spread and cytotoxicity in breast cancer tumor spheroids.[223] It is therefore conceivable that MeV alone efficiently penetrated the spheroid through syncytia formation and viral spread, but was inhibited by concomitant PV infection. Microscopic observation of the MeV-encoded eGFP in the triple combination regimen showed reduced transgene expression (**Figure 7-14**) in presence of PV, mirroring the observations in the 2D setting. If MeV fusion and hemagglutinin proteins are equally affected by PV infection, reduced syncytia formation and MeV penetration of the spheroid could explain the antagonistic effect.

While the spheroid model offers the advantage of incorporating multiple cell types and mimicking extracellular matrix-like structures through fibroblast inclusion, they still lack key physiological components. Especially in the context of viroimmunotherapies, the presence of immune cell populations would be vital to assess the effect of triple combination on immune induction. To address this, patient-derived tumor organoids could serve as a valuable next step. For this project, the next step is to employ biopsy-derived tumor organoids, that are generated from single cell suspensions. They preserve the heterogeneous cell population of the original tumor (including immune cells) and as well as the mutational and transcriptional profiles.[224] This allows the analysis of patient-to-patient variability and may help to identify subgroups that could derive the most benefit from radiovirotherapy.[225]

Nonetheless, even advanced *in vitro* or *ex vivo* approaches cannot substitute for the presence of a fully intact immune system, where immune cell priming, trafficking and memory formation can be studies. This still requires the use of animal, most commonly murine, models. Our group and others have demonstrated the feasibility of evaluating MeV in syngeneic murine tumor models.[77,226] In preparation for such studies, I generated and characterized several clones of three murine cell lines stably expressing the MeV entry receptor human CD46 via lentiviral transduction. (**Figure 4-30**). However, MeV susceptibility varied between the cell lines and clones and did not correlate with hCD46 expression levels. This is in line with reports that post-entry restriction factors limit MeV replication in murine cell lines.[227] MeV replication and spread can be enhanced by employing transgenic mice that lack the type-I IFN receptor IFNAR.[228,229] But the use of such murine models is unsuitable in the context of this project, where the underlying hypothesis involves intact IFN signaling.

In addition to constraints regarding MeV susceptibility, antigenicity of hCD46 presents a further challenge when studying MeV *in vivo*. Previous work in our group revealed delayed tumor growth and frequent loss of hCD46 expression in vivo, likely reflecting immune-mediated clearance of hCD46-expressing cells.[135] In preliminary *in vivo* experiments, the murine GBM tumor cell line I generated, GL261-hCD46, was implanted into C57BL/6 mice by Laurent Daeffler and his team. While parental tumors without CD46 showed the expected growth kinetic, no tumors grew in mice implanted with hCD46-expressing cells. Interestingly, implantation with other clones that showed lower CD46 expression (clone A and B, compared to clone C; **Figure 4-30**) was more successful and tumors grew in ca. 50 % of implanted mice (data not shown, animal experiments are performed by Laurent Daeffler in Straßbourg). These results underscore the importance of careful clone selection to balance receptor expression with immunogenic tolerance for successful in vivo establishment.

The evaluation of protoparvoviruses in murine models also presents distinct challenges. Mice or rats are the natural hosts of the rodent *Protoparvovirus* strains employed here (H-1PV, referred to as "PV" and minute virus of mice (MVM)).[73] Thus, no genetic modification is required to perform *in vivo* studies. Nevertheless, cell lines show variable susceptibility to PV or MVM infection. The murine PDAC cell lines employed here did not show cytotoxic effects at standard MVM doses (data not shown, experiments were performed by Assia Angelova and her team). PDAC is a highly heterogeneous disease and distinct subtypes can be classified based on phenotypic and transcriptional markers.[230] Vienne *et al* showed a strong tropism of MVM to PDAC cells of the basal-like subtype.[231] While we did not characterize the molecular subtype of the PDAC cell lines used here, this factor may explain the limited response and should be considered in future *in vivo* studies.

All in all, each experimental model offers distinct advantages and inherent limitations. Careful alignment of the chosen model with the underlying research hypothesis is essential, while maintaining awareness of its constraints. Ultimately, only clinical trials can determine which novel therapeutics elicit a benefit for cancer patients.

5.6. Clinical outlook and conclusion

The ultimate goal of translational cancer research is to establish therapies that bring benefit to cancer patients. In the field of oncolytic virotherapy, only one actively replicating virus has so far advanced to (routine) clinical practice in the United States and Europe. T-VEC (a HSV derived construct encoding for granulocyte-macrophage colony-stimulating factor (GM-CSF)) received FDA-approval for advanced melanoma in October 2015. Exactly one decade later, no additional OV has gained FDA- or EMA approval,

yet the field has progressed: A variety of viral vectors with and without transgenes and in combination or as monotherapies are tested preclinically and in clinical trials (recently comprehensively reviewed[120]). Among them are PV and MeV.

PV's first human application dates back to 1965, where it was applied to two osteosarcoma patients without the report of serious adverse events.[232] Two clinical trials have so far evaluated PV's safety and efficacy. A phase I/IIa trial in GBM enrolled 18 patients, who received escalating doses of PV intravenously (i.v.) or intratumoral (i.t.) followed by surgery and injection of PV into the wall of the resection cavity. No dose-limiting toxicities were observed. Notably, PV genomes and transcripts could be detected in resected tumors after i.v. application, proving that PV is able to cross the blood-brain barrier and home to the tumor. In addition, the trial confirmed recruitment of CD4+ and CD8+ tumor-infiltrating lymphocytes (TILs), virus-specific T cell responses in peripheral blood and prolonged survival compared to data from recent meta-analyses.[16] However, these encouraging results need to be interpreted with caution due to the low number of patients, the trial design (single-center, non-controlled dose-escalation trial with different routes of administration) and other potential confounders (such as the effect of repeated surgery). The second trial was a phase II trial in patients with metastatic PDAC and enrolled 7 patients. PV was applied at escalating doses i.v. and subsequently into hepatic metastasis. Again, viral genomes could be detected in most tumor samples and virus-specific T cell responses were observed in 9 out of 12 patients tested. Two patients had a partial response and showed prolonged survival of 326 and 555 days.[31] However, similar limitations in trial design and patient number as mentioned above apply. Nevertheless, the clinical evaluation of PV has thus far revealed an excellent safety profile with first encouraging results regarding immune induction and therapeutic efficacy.

MeV has been evaluated more extensively in clinical trials, the first one dating back more than two decades.[100,233] Clinical studies have investigated MeV in a several entities, including cutaneous T-cell lymphoma[233], multiple myeloma (MM)[234], ovarian cancer[235] and GBM[236]. Administration routes have varied by indication (i.v., i.t., intracranial, intraperitoneal), but MeV has generally been well tolerated with few dose-limiting toxicities.

A recent trial in GBM by Galanis *et al.* investigated the influence of IFN on MeV replication through trial-accompanying research. Employing a previously established predictive algorithm of 22 ISGs,[237] they showed that MeV replication within treated tumors inversely correlated with the baseline IFN response. Conversely, tumors that were more permissive to MeV replication also had increased levels of immune activation on transcriptomic level and a (non-significant) trend towards enhanced CD4+ and CD8+ T cell

infiltration. These favorable immune activation patterns, coupled with low IFN signaling at baseline, were observed in only 2 out of 13 patients. The authors suggest that this is mirrored by the usually observed response rate in OV trials of 9-13 %.[236] This finding underscores the importance of patient stratification (possibly based on baseline IFN signaling) to identify those most likely to benefit from OV therapy.

I want to highlight two very different, yet striking cases that underline the therapeutic efficacy MeV may elicit: One single administration of MeV i.v. elicited a complete response in an on-trial MM patient, accompanied by a pronounced anti-tumor immune response. The patient was confirmed to be in complete remission even 6 years after the MeV infusion.[98] The second interesting case report is a study by Beata Halassy *et al*. in which two viral vectors were administered: VSV and MeV, which the patient, a virologist, had produced under non-GMP standards in her own lab. The viruses were repeatedly administered i.t. into her recurrent triple negative breast cancer and resulted in the tumor mass becoming resectable. After two prior recurrences, the patient now remains in complete remission for at least 4 years.[99,238] Apart from such case reports, the clinical trials of MeV have not yet yielded breakthrough success. Accordingly, novel approaches including combination therapy, carrier cells or biomarker-selection of eligible patients are currently under investigation.[100,236]

To date, neither MeV nor PV have been combined with radiotherapy in clinical trials. Given the favorable safety profiles observed for both viruses and the routine clinical use of radiotherapy, such combinations appear feasible and promising. Notably, neither virus shows reduced replicative capacity following irradiation, even at high doses up to 50 Gy. This was shown for MeV by J.Derani[135] and for PV by Laurent Daeffler (manuscript in preparation). This resilience raises the practical possibility of repeated dosing in a radiovirotherapy regimen without inactivating the oncolytic agent.

In summary, the data presented in this thesis support the promise a triple radiovirotherapy approach can hold for selected patients: enhanced cytotoxicity, pronounced innate immune signaling and markers of immunogenic cell death were observed. Continued preclinical work will focus on certain aspects discussed above: Deciphering the mechanism of PV-mediated reduction of MeV transgene expression, enhancing the combination by rational MeV vector design (e.g. encoding beneficial therapeutic transgenes), assessing other promising combination partners, employing additional advanced pre-clinical models (incl. patient-derived organoids) and investigating triple radiovirotherapy *in vivo*. If successful, a swift translation into an early clinical trial could benefit the increasing number of GBM and PDAC patients with otherwise limited treatment options and poor prognosis.

6. Abbreviations

ABAM	Antibiotic antimycotic solution
ACT	Adoptive cell therapy
ACTB	β-Actin gene
ANOVA	Analysis of variance
ATM	Ataxia-telangiectasia mutated
AUC	Area under the curve
BCA	Bicinchoninic acid
BSL	Biosafety Level
CALR	Calreticulin
CAR	Chimeric antigen receptor
cDNA	Complementary DNA
cGAS	Cyclic GMP-AMP synthase
ciu	Cell infectious units
Ct	Cycle threshold
CT	Computed tomography
DAMP	Danger associated molecular pattern
DEG	Differentially expressed gene
DMEM	Dulbecco's Modified Eagle's Medium
DMSO	Dimethyl sulfoxide
DNA	Deoxyribonucleic acid
eGFP	Enhanced green fluorescent protein
EGFR	Epidermal growth factor receptor
ELISA	Enzyme-linked immunosorbent assay
FACS	Fluorescence-activated cell sorting
FCS	Fetal Calf Serum
FDA	Food and drug administration

GBM	Glioblastoma
GM-CSF	Granulocyte-macrophage colony-stimulating factor
GMP	Good manufacturing practice
H-1PV	H-1 parvovirus
HLA	Human leukocyte antigen
HSA	Highest single-agent
HSV-1	Herpes simplex virus type 1
i.v.	intravenously
ICI	Immune checkpoint inhibitor
IDH	Isocitrate dehydrogenase
IF	Immunofluorescence
IFITM	Interferon-induced transmembrane protein 1
IFN	Interferons
IFNB	Interferon-β gene
IMRT	Intensity-modulated radiotherapy
IRF	IFN regulatory factors
ISG	Interferon stimulated gene
ISGF3	Interferon-stimulated gene factor 3
JAK	Janus kinase
JAM-A	Junctional adhesion molecule A
ld	Leader [MeV genome]
LET	Linear energy transfer
lncRNA	Long non-coding RNA
MDA-5	Melanoma differentiation associated protein 5
MDS	Multidimensional Scaling
MeV	Measles Virus
mins	Minutes
MOI	Multiplicity of Infection

MVM	Minute virus of mice
NDV	Newcastle disease virus
NFκB	Nuclear factor kappa b
NGS	New generation sequencing
NIS	Sodium iodide symporter
NS	Non structrual protein [Parvovirus protein]
NSCLC	Non-small-cell lung cancer
ORF	Open reading frame
p.r.	Post radiation
p.tr.	Post treatment
PAMP	Pathogen associated molecular pattern
PCR	Polymerase Chain Reaction
PDAC	Pancreatic Ductal Adenocarcinoma
PFA	Paraformaldehyde
pfu	Plaque forming units
PKR	Protein Kinase R
PV	Refers to H-1PV (H-1 parvovirus)
PVDF	Polyvinylidene fluoride
qPCR	Quantitative PCR
RIG-I	Retinoicacid-inducile gene-1
RNA	Ribonucleic acid
ROS	Reactive oxygen species
RPMI	Roswell Park Memorial Institute 1640
RVTx	Radiovirotherapy
s.c.	Subcutaneously
SAT	Small alternatively translated
SDS-PAGE	Sodium dodecyl sulphate-polyacrylamide gel electrophoresis

STAT	Signal transducer and activator of transcription
TAA	Tumor associated antigen
TCR	T cell receptor
TERT	Telomerase reverse transcriptase
tr	Trailer [MeV genome]
T-VEC	Talminogene laherparepvec
TYK	Tyrosine kinase
VP	Structural protein [Parvovirus protein]
VSV	Vesicular stomatitis virus
ZIP	Zero interaction potency

7. Supplementary data

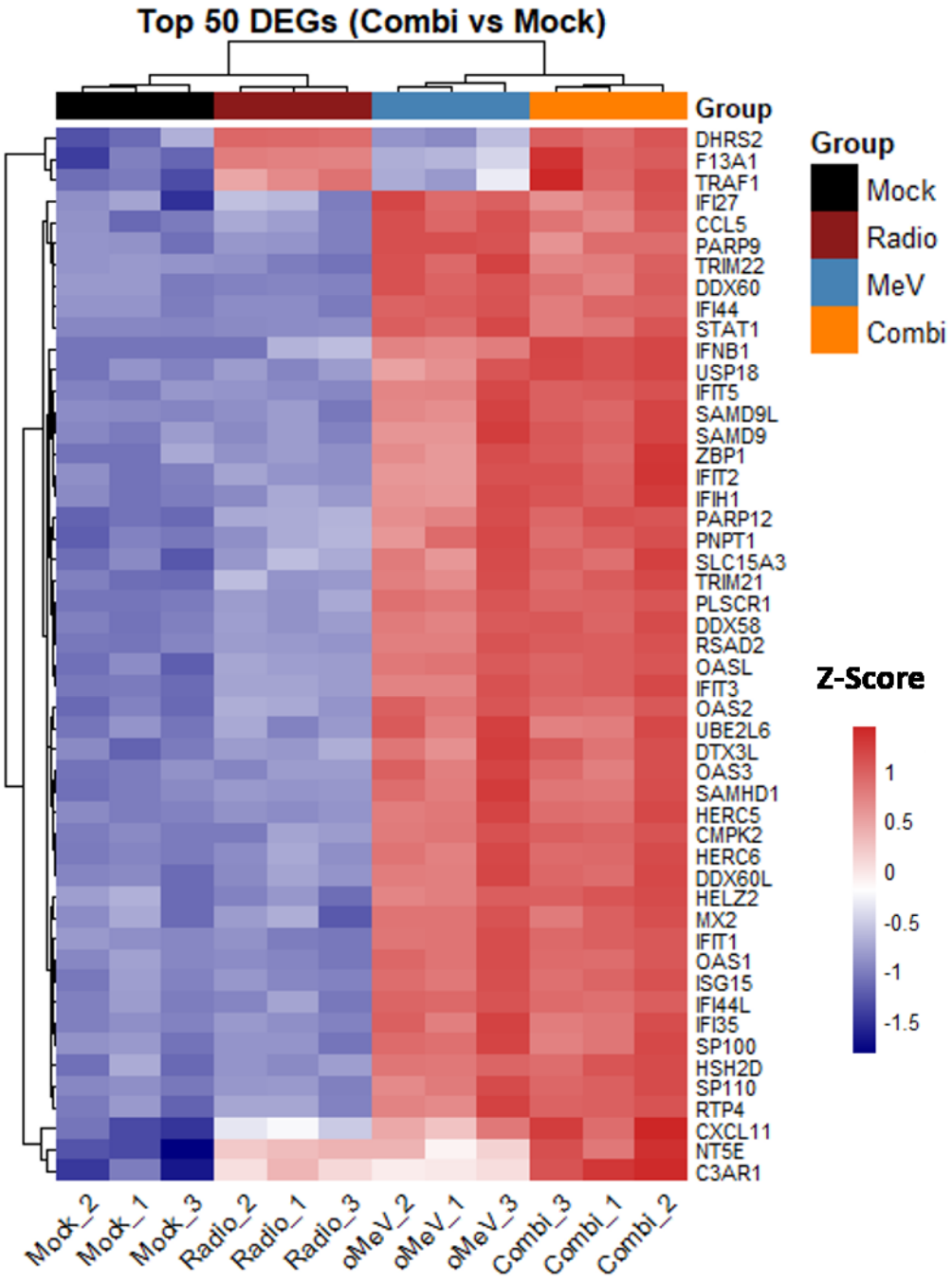

Figure 7-1: TOP 50 DEGs sorted by FDR in combination versus mock are mainly MeV-driven

I treated and prepared samples as described in the legend to Figure 4-1. The heatmap shows Z-Score normalized expression of the top 50 DEGs of the combination versus mock comparison for all samples. I selected the top 50 DEGs based on FDR among differentially expressed genes (|logFC| > 1). I applied Euclidian clustering across rows (genes) and columns (samples).

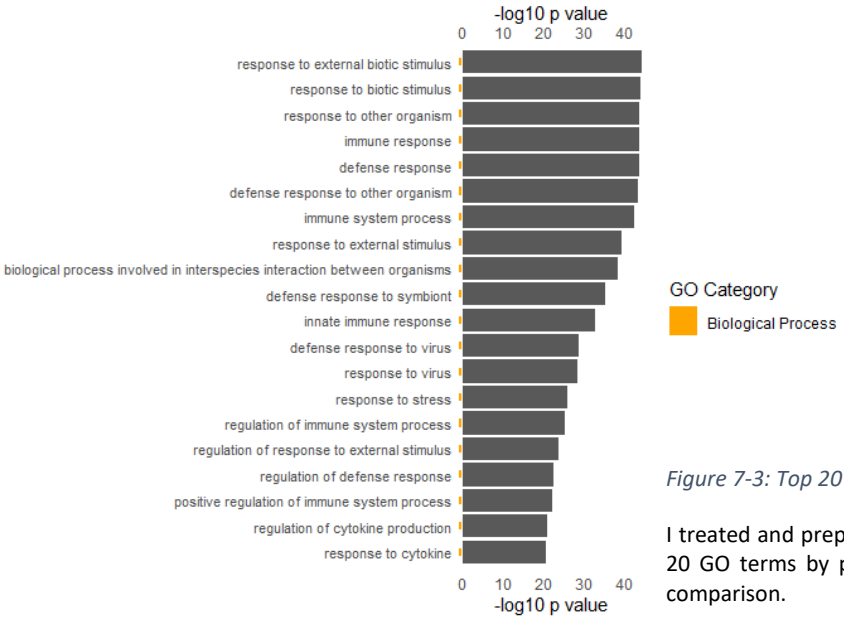

Figure 7-3: Top 20 GO terms in combination versus mock treatment

I treated and prepared samples as described in the legend to Figure 4-1. Top 20 GO terms by p value that are upregulated in combination versus mock comparison.

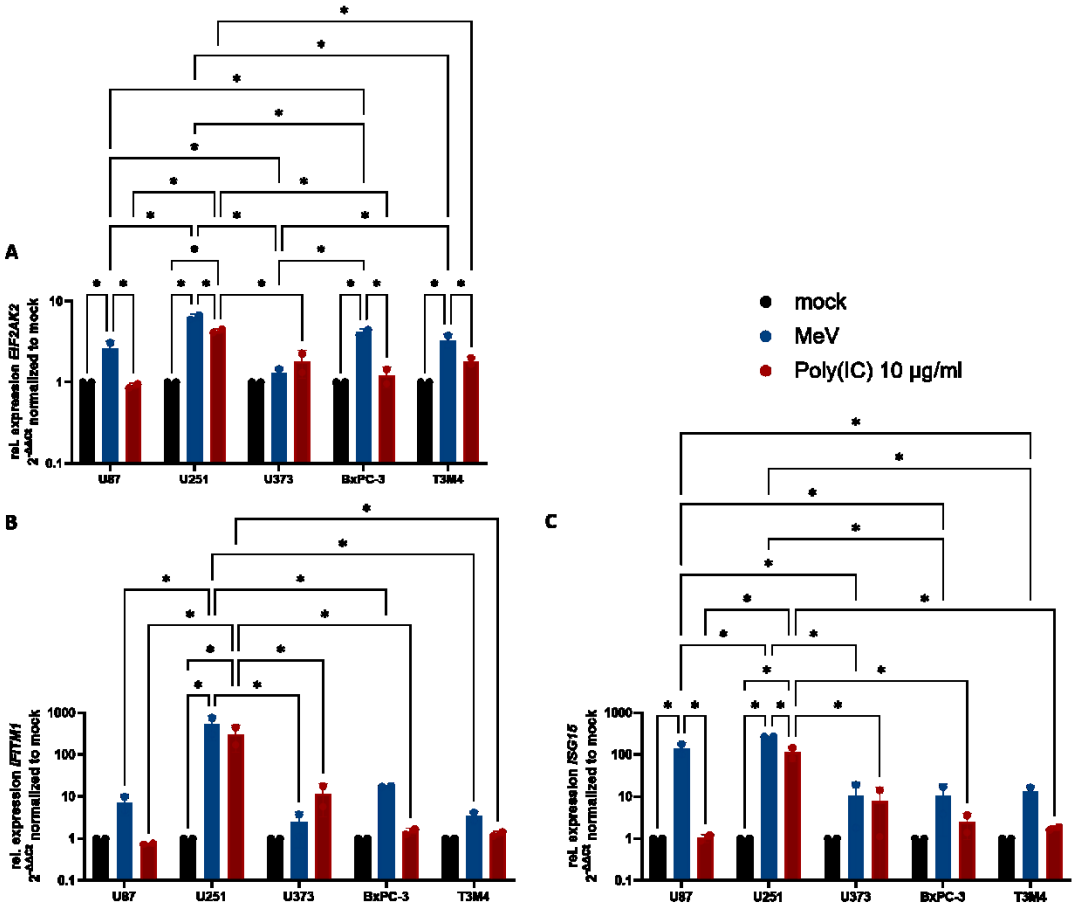

Figure 7-2: All significances depicted for Figure 4-5

I isolated RNA 48 h after treating cells with either 10 µg/ml Poly(IC) or MeV. Through RT-qPCR analysis, I compared levels of (A) EIFAK2*, (B)* ISG15 *and (C)* IFITM1 *transcripts. $2^{-\Delta\Delta CT}$ values, normalized to* ACTB *and mock-treated controls, in response to the respective treatment are depicted. Mean and standard deviation of two independent experiments is shown. * : p<0.05*

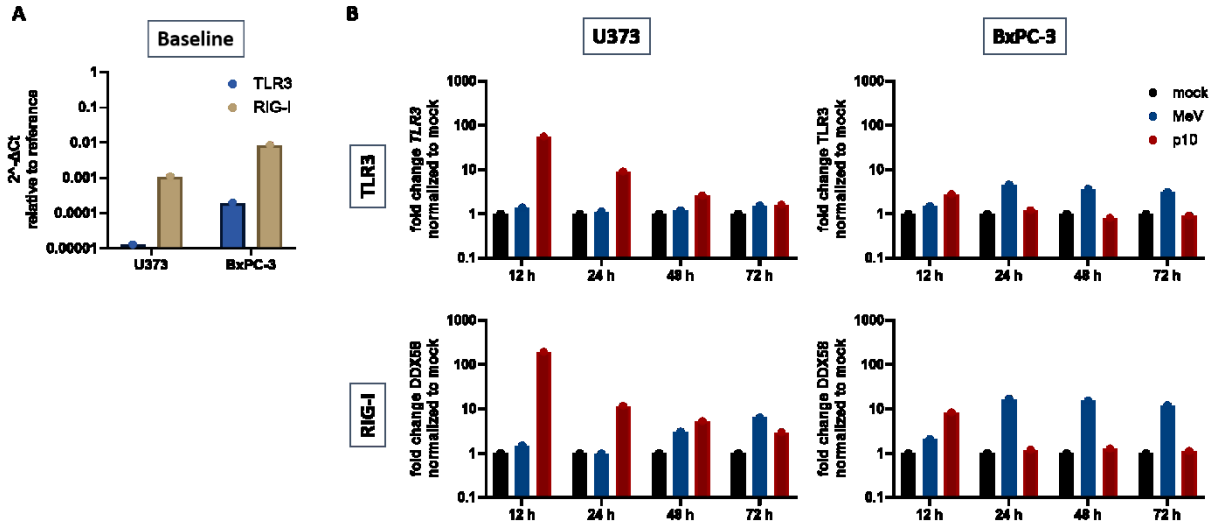

Figure 7-4 Comparing PRR levels between U373 and BxPC-3

I performed qPCR for *TLR3* and *DDX58* (RIG-I). (A) Baseline levels of TLR3 and *DDX58* In U373 and BxPC-3 36 h after seeding in untreated cells. $2^{-\Delta Ct}$, normalized to *ACTB* is shown. (B) I harvested RNA of U373 and BxPC-3 cells at several timepoints p.tr. with MeV at MOI 0.1 or poly(IC) at 10 µg/ml. $2^{-\Delta\Delta Ct}$, normalized to ACTB1 and mock-treated samples, is shown.

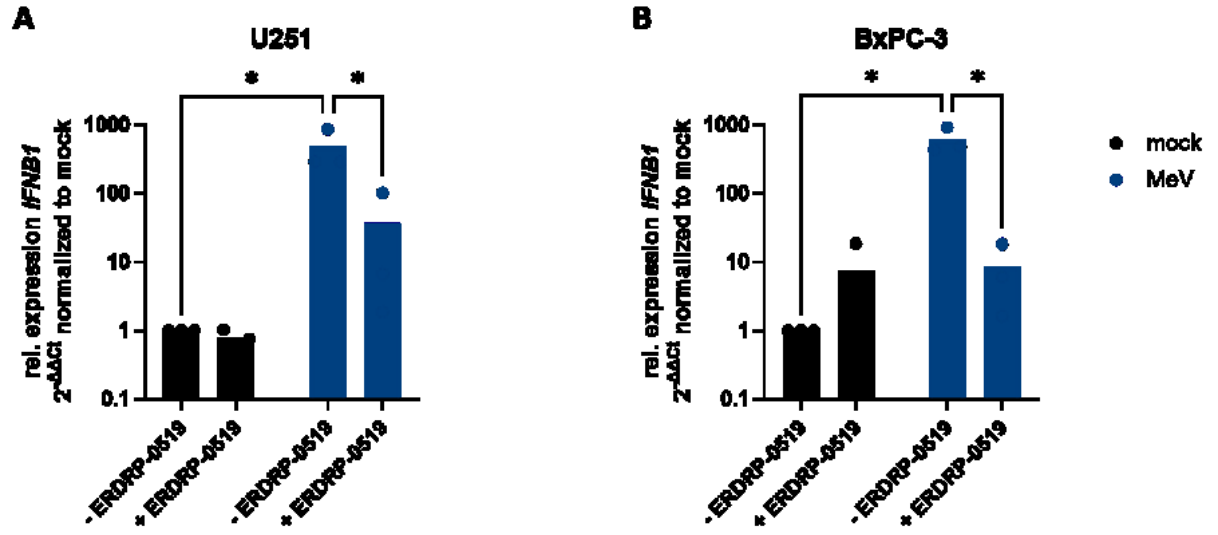

Figure 7-5: IFNB1 induction under MeV polymerase inhibition

I infected U251 (A) and BxPC-3 (B) cells with MeV 24 h after seeding. During incubation with infection inoculum and when media was changed after 2 hours, I added MeV polymerase inhibitor ERDRP-0519 to the medium at a concentration of 1 µM. I isolated RNA and performed RT-qPCR of *IFNB1.* Mean and individual $2^{-\Delta\Delta Ct}$ value are shown, normalized to *ACTB*. I performed two-way ANOVA with Tukey's multiple comparison test *: $p < 0.05$

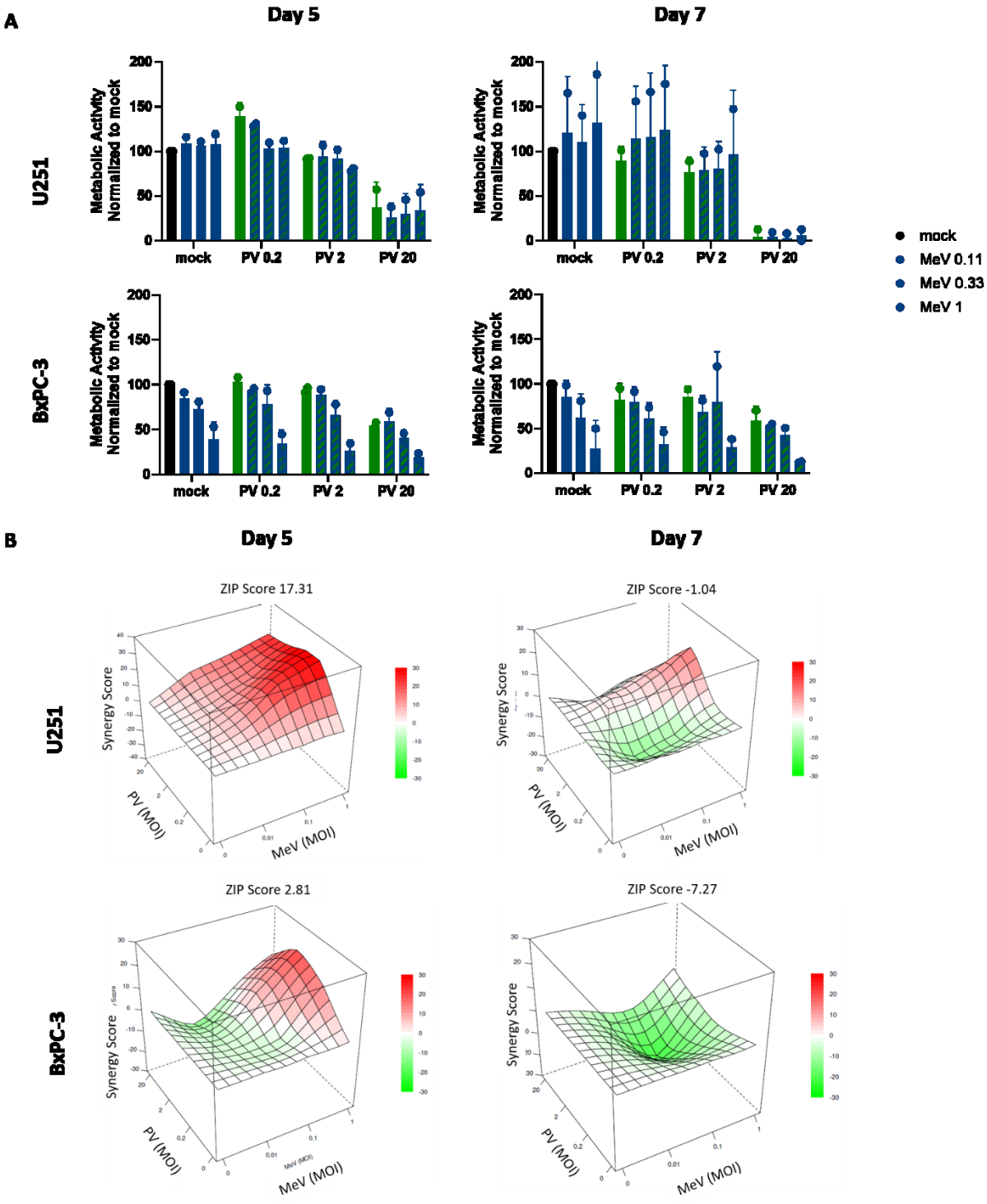

Figure 7-6: Cytotoxicity and Synergy of simultaneous OV application

I infected BxPC-3 and U251 cells with PV and MeV at different concentrations simultaneously 24 h after seeding. (A) On day 5 and day 7 p.tr. I measured metabolic activity of the cells by XTT assays. (B) I analyzed synergy using the SynergyFinderPlus Software and report the ZIP score. N=2 independent experiments

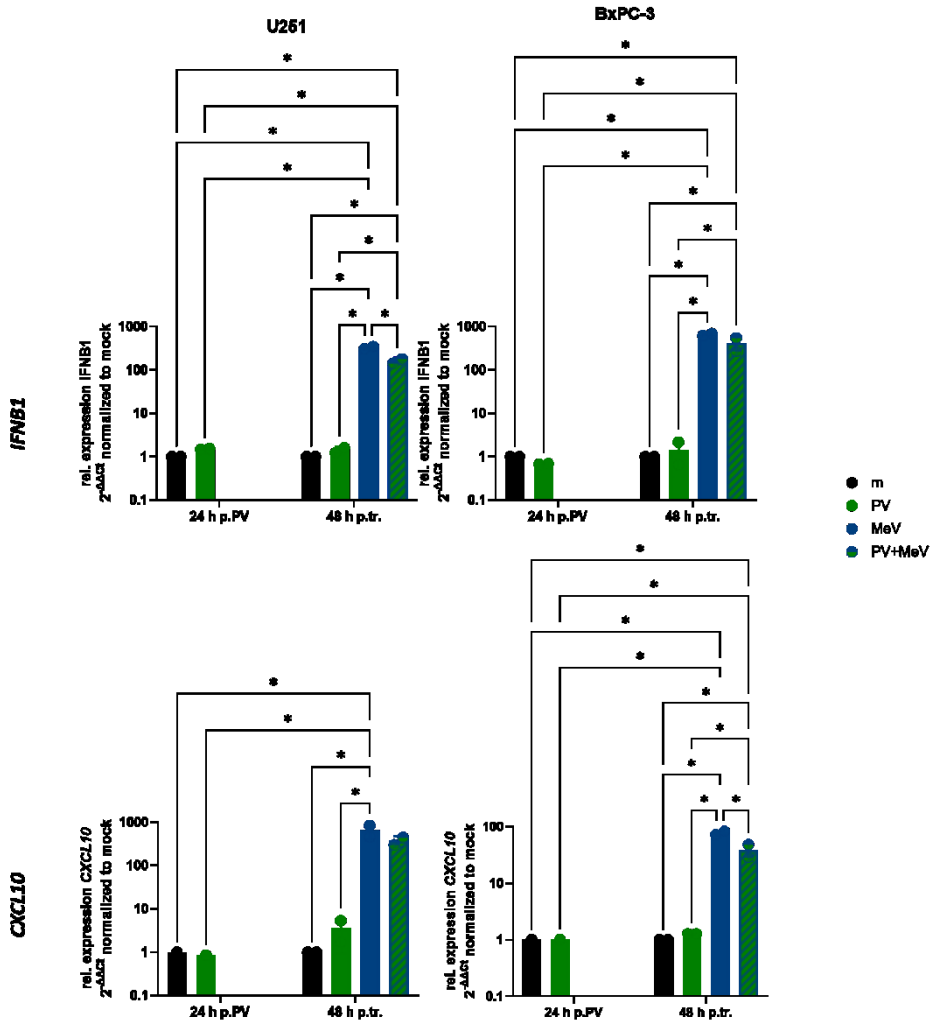

Figure 7-7: All significances depicted for Figure 4-12

I infected cells with PV at MOI 2 (U251) or MOI 5 (BxPC-3) and 24 h later with MeV at an MOI of 1 (both cell lines). I harvested RNA 24 h after PV infection (time point of MeV infection) and 48 h after completion of treatment. I analyzed transcript levels of *IFNB1* and *CXCL10* via RT-qPCR for BxPC-3 and U251 cells. Mean and standart deviation of two independent experiment is depicted. m -mock, PV - Parvovirus, MeV - Measles Virus, p.PV - post PV infection, p.tr. - post treatment; *: $p < 0.008$ in two-way ANOVA with Tukey's multiple comparisons test; all significant combinations are indicated

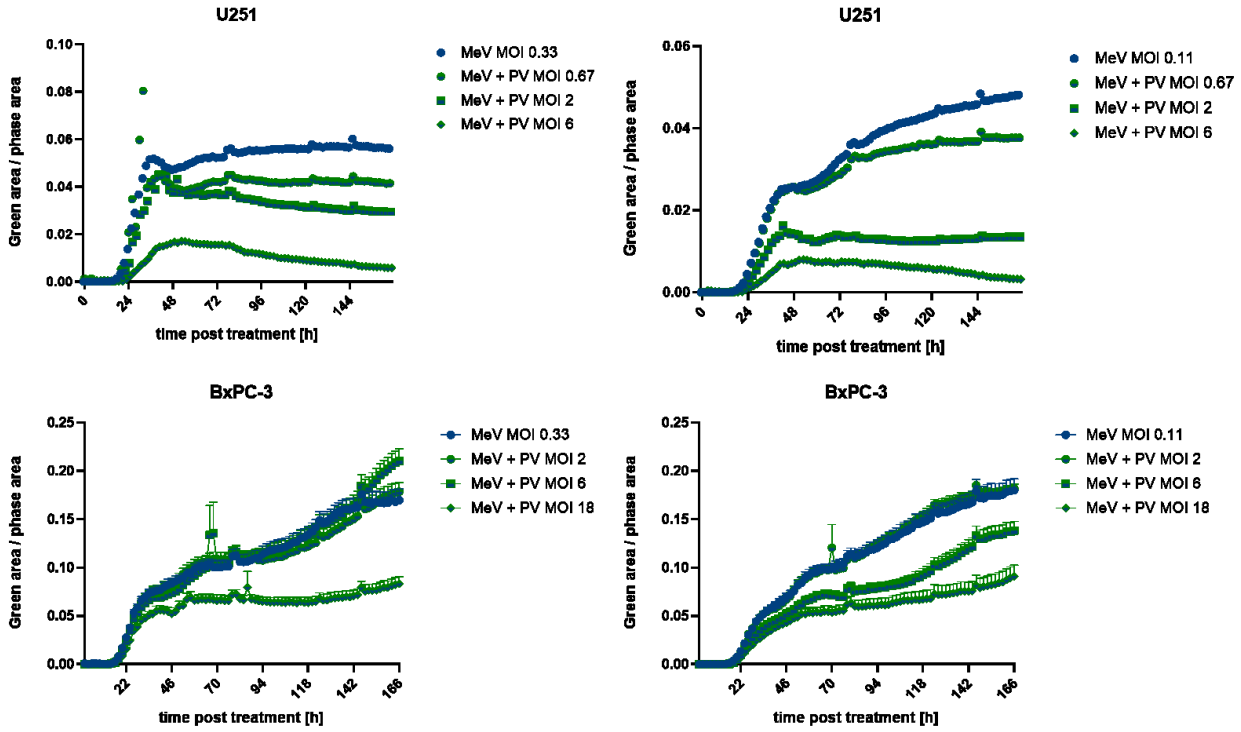

Figure 7-8: MeV transgene expression in dual virotherapy for infection with MeV MOI of 0.33 and 0.11

I infected cells with PV at the indicated MOIs and infected with MeV at an MOI of 0.11 or 0.33 24 h thereafter. I place the plates in an IncuCyte and measured phase area and eGFP expression over the course of 7 days. I normalized eGFP expression to phase area and plotted it over time. PV - Parvovirus; MeV - Measles virus; MOI - multiplicity of infection

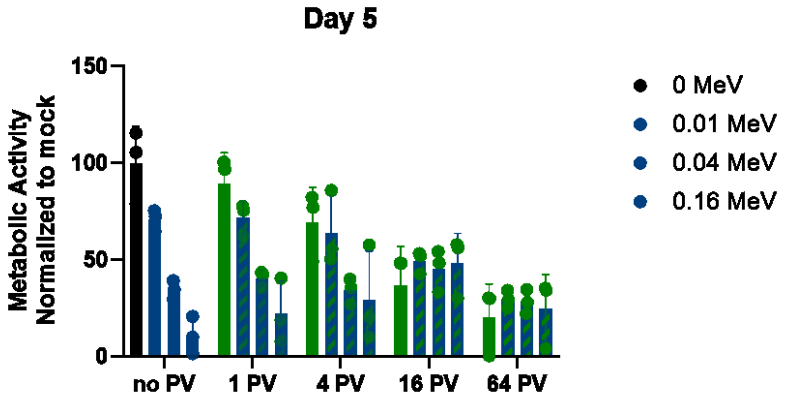

Figure 7-9: Extended dose combinations of dual virotherapy

I treated PDAC spheroids, comprised of PDAC cells (AsAnPaCa), endothelial cells (HUVEC) and fibroblasts (MRC-5) in a ratio of 1:2:3, with PV and MeV in an extended dose range from MOI 1 to 64 for PV and MOI 0.01 to 0.16 for MeV. On day 5, I performed I performed the ATP-based cytotoxicity assay CellTiterGlo® 3D. Mean and standard deviation of three technical replicates is shown.

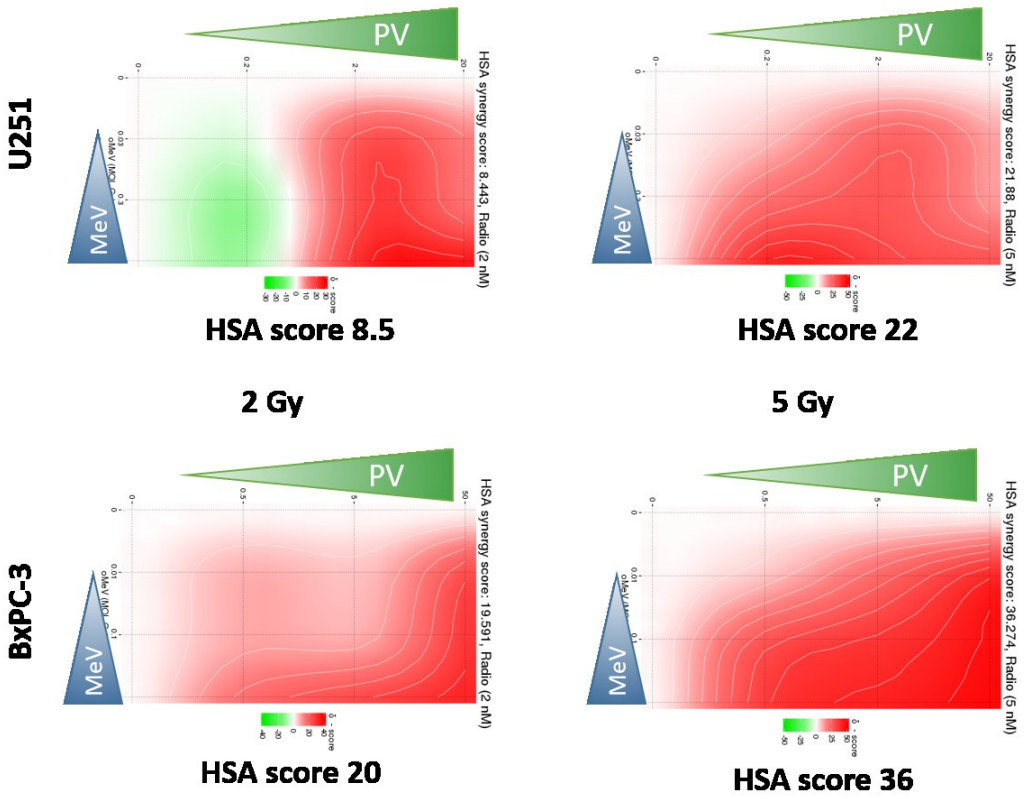

Figure 7-10: HSA synergy analysis for XTT-based cytotoxicity analysis of triple radiovirotherapy

I performed synergy calculations with the HSA model on the cytotoxicity data acquired by XTT assay (depicted in **Figure 4-17,** day 7). Calculations for the combination of dual virotherapy with 2 and 5 Gy radiation are reported. Negative scores (green) indicate antagonism, positive scores (red) synergy.

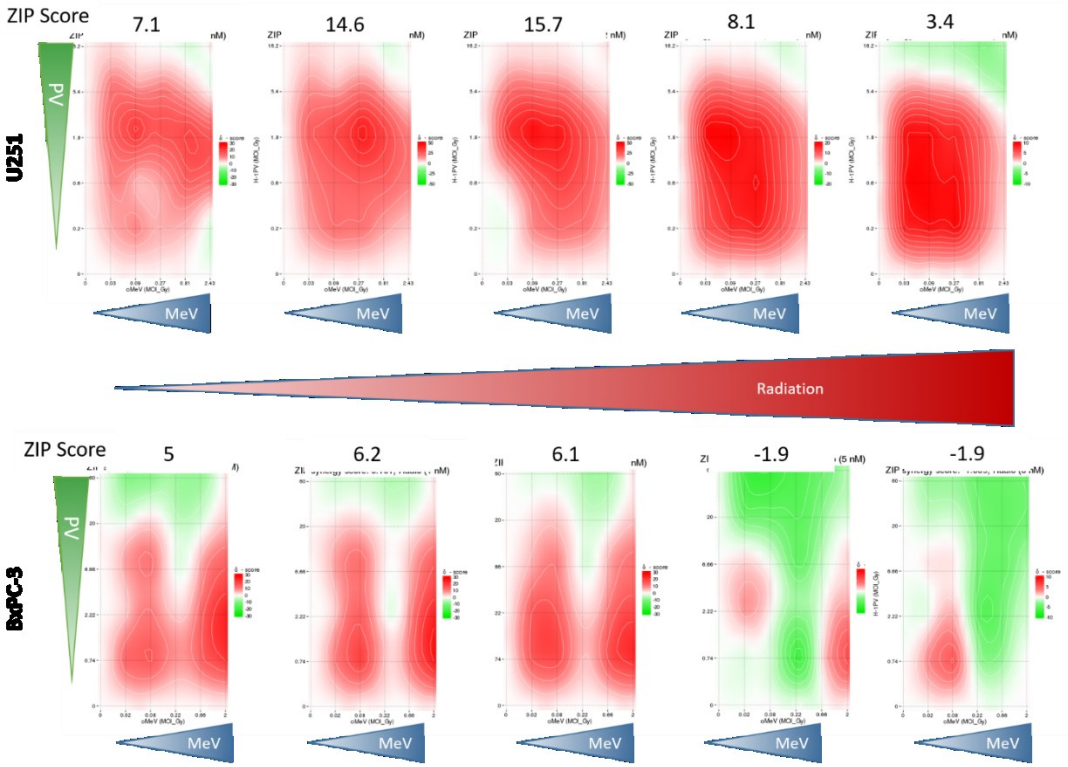

Figure 7-11: Synergy plots for all dose combinations

I calculated ZIP synergy scores with SynergyFinder3.0 using the averaged cytotoxicity data of the extended dose combinations assessed via crystal violet assays. Each graph depicts all ZIP scores for the individual PV and MeV dose combinations with one radiation dose. The overall ZIP score for the triple combination at that radiation dose is given numerically above the graph. PV dose increases within each graph from bottom to top, MeV dose increased within each graph from left to right. Radiation dose increases across graphs from left to right. ZIP scores around 0 (white) are considered additive, positive scores (red) synergistic and negative scores (green) antagonistic

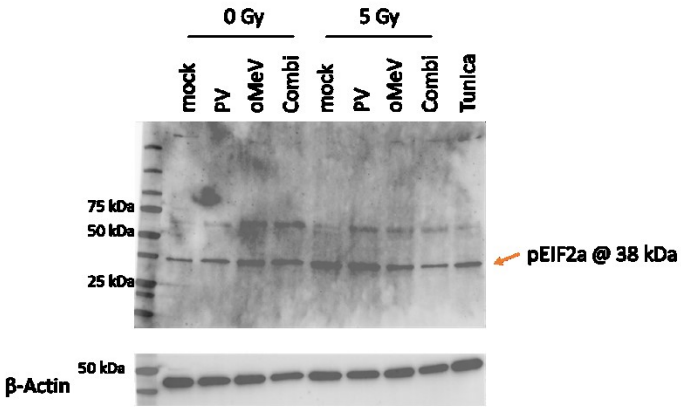

Figure 7-12: Western blot of pEIF2α under triple radiovirotherapy

I treated U251 cells with triple radiovirotherapy (5 Gy irradiation, PV MOI 2, MeV MOI 1) and harvested cells 48 h later. Cells treated with Tunicamycin at 5 µg/ml served as positive control. I performed SDS-PAGE and western blot. I probed for phosphorylated EIF2α on the membrane using a specific antibody. β-actin served as loading control. PV – Parvovirus; MeV – Measles virus; Tunica – Tunicamycin; chemiluminescent exposure time= 3000s

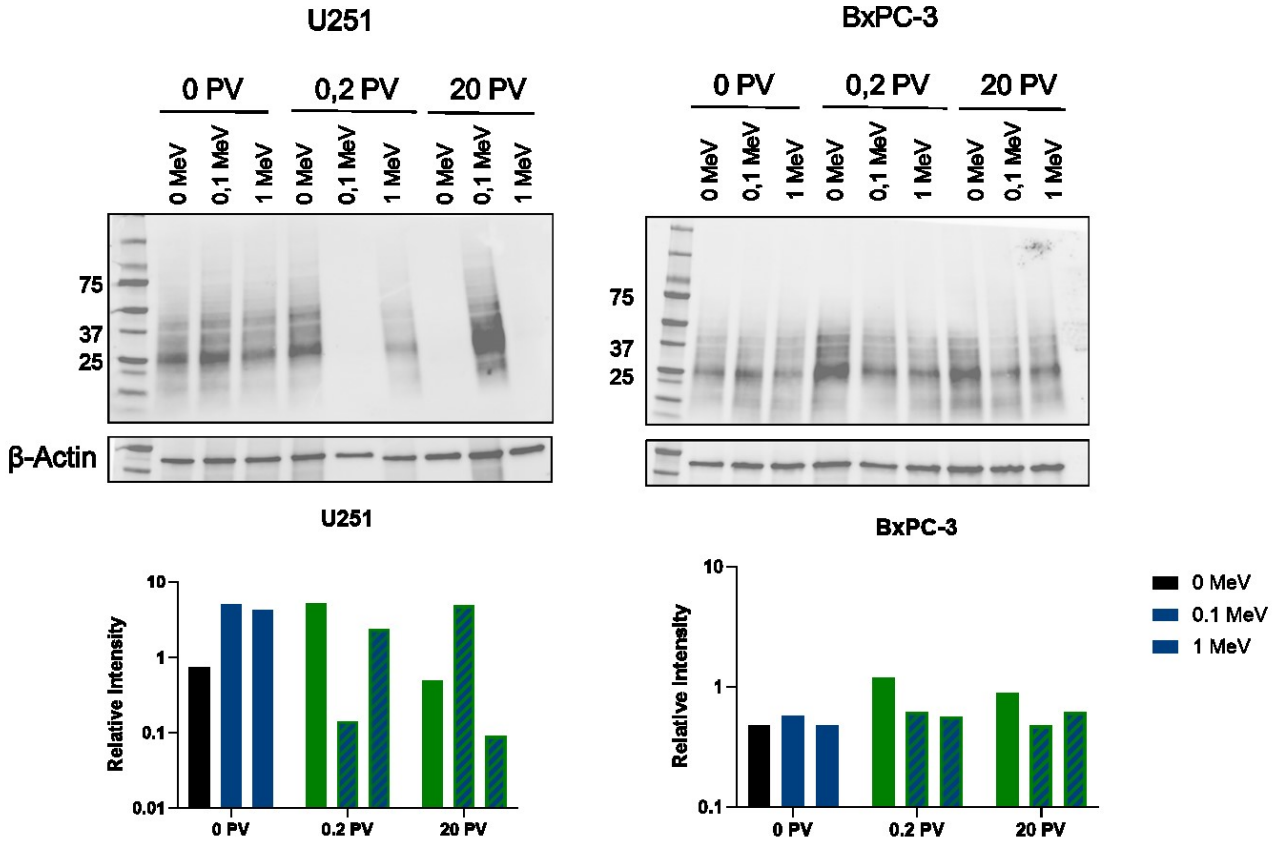

Figure 7-13: SUnSET assay of dual virotherapy to assess translational shutdown

I treated U251 and BxPC-3 with dual virotherapy. 48 h p.tr., I incubated cells with 5 µg/ml puromycin for 15 minutes prior to harvesting cell lysates in RIPA buffer. Katja Kerner performed SDS-PAGE followed by western blot on the cell lysates and detected puromycin on the membrane. She used β-actin as loading control I quantified the band intensities and normalized to β-actin. PV – Parvovirus; MeV – Measles virus

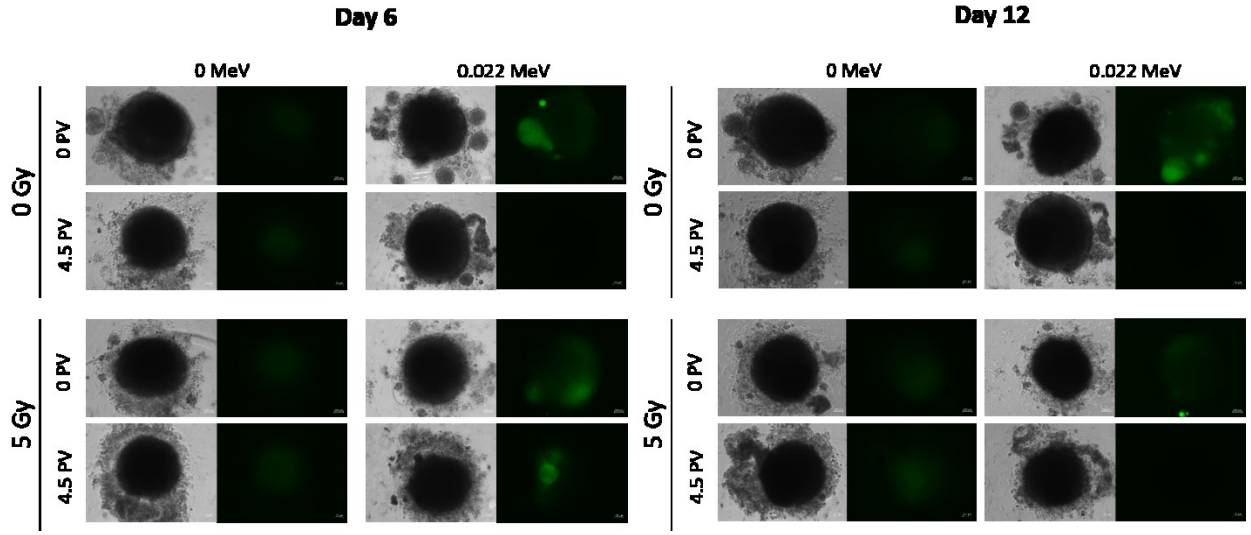

Figure 7-14: Microscopic observation of PDAC spheroids under triple radiovirotherapy

I treated heterotypic PDAC spheroids with extended dose combinations of radio-, PV and MeV-therapy. I took images 6 and 12 days after treatment of phase contrast and fluorescent signal in the eGFP channel. Depicted is the combination of 5 Gy, PV MOI 4.6 and MeV MOI 0.022 and their combination with untreated conditions. 20x objective, scale bar indicates 100 µm

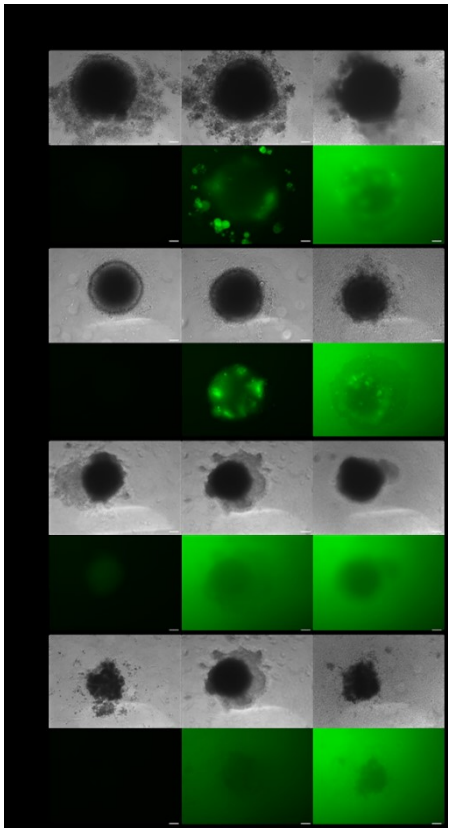

Figure 7-15: Microscopic observation of MeV-infected spheroids (triple- vs. mono spheroids)

I infected heterotypic PDAC spheroids and their mono-typic counterparts with MeV at MOI 0.3 and 3 and observed eGFP expression via fluorescent microscopy 72 h post infection.

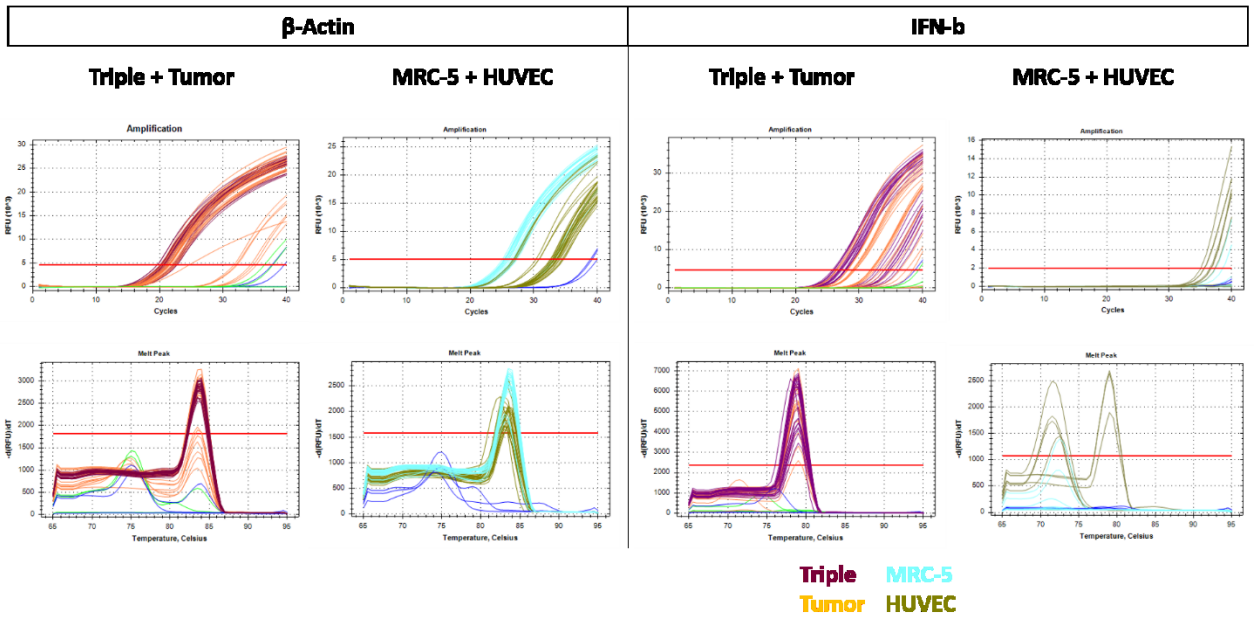

Figure 7-16: Amplification cuvres and melt peaks of qPCR analysis of ACTB and IFNB1 in triple- and mono-spheroids

I harvested triple heterotypic PDAC spheroids and their monotypic counterparts 72 h post infection, islated RNA and analyzed *ACBT* and *IFNB1* via RT-qPCR. Depicted are amplification curves and melt peak analysis for triple (purple) and tumor (orange) and MRC-5 (blue) and HUVEC (green) spheroids, respectively.

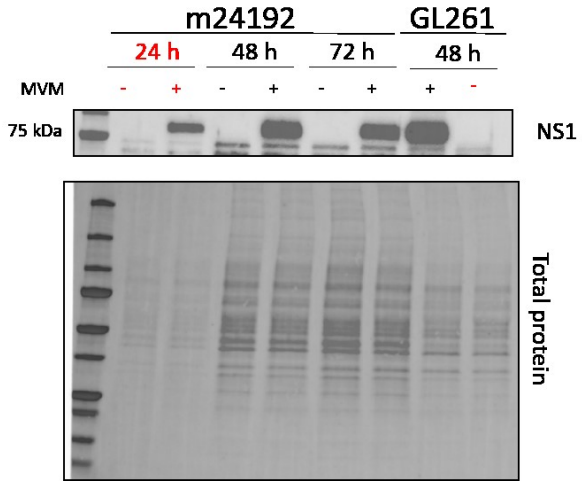

Figure 7-17: Parvovirus protein expression in murine cell lines

To analyze susceptibility of m24192 to parvovirus infection, I performed a SDS-PAGE and western blot analysis of viral NS1 protein in protoparvovirus-infected (viral strain MVM) cells 24 – 72 h post infection. GL261 infected with MVM served as positive control. Total protein depicted as loading control. 20 µg protein was loaded per lane, except for conditions marked in red, because protein concentration in cell lysate was not sufficient

8. Literature

1 Bray, F. *et al.* Global cancer statistics 2022: GLOBOCAN estimates of incidence and mortality worldwide for 36 cancers in 185 countries. *CA Cancer J Clin* **74**, 229-263 (2024). https://doi.org:10.3322/caac.21834

2 Murthy, S. S. *et al.* Premature mortality trends in 183 countries by cancer type, sex, WHO region, and World Bank income level in 2000-19: a retrospective, cross-sectional, population-based study. *Lancet Oncol* **25**, 969-978 (2024). https://doi.org:10.1016/S1470-2045(24)00274-2

3 Siegel, R. L., Kratzer, T. B., Giaquinto, A. N., Sung, H. & Jemal, A. Cancer statistics, 2025. *CA Cancer J Clin* **75**, 10-45 (2025). https://doi.org:10.3322/caac.21871

4 Ostrom, Q. T. *et al.* CBTRUS Statistical Report: Primary Brain and Other Central Nervous System Tumors Diagnosed in the United States in 2016-2020. *Neuro Oncol* **25**, iv1-iv99 (2023). https://doi.org:10.1093/neuonc/noad149

5 Louis, D. N. *et al.* The 2021 WHO Classification of Tumors of the Central Nervous System: a summary. *Neuro Oncol* **23**, 1231-1251 (2021). https://doi.org:10.1093/neuonc/noab106

6 Weller, M. *et al.* Glioma. *Nat Rev Dis Primers* **10**, 33 (2024). https://doi.org:10.1038/s41572-024-00516-y

7 Ostrom, Q. T. *et al.* Risk factors for childhood and adult primary brain tumors. *Neuro Oncol* **21**, 1357-1375 (2019). https://doi.org:10.1093/neuonc/noz123

8 Poon, M. T. C., Sudlow, C. L. M., Figueroa, J. D. & Brennan, P. M. Longer-term (>/= 2 years) survival in patients with glioblastoma in population-based studies pre- and post-2005: a systematic review and meta-analysis. *Sci Rep* **10**, 11622 (2020). https://doi.org:10.1038/s41598-020-68011-4

9 Eckert, T. *et al.* Immune Resistance in Glioblastoma: Understanding the Barriers to ICI and CAR-T Cell Therapy. *Cancers (Basel)* **17** (2025). https://doi.org:10.3390/cancers17030462

10 Stupp, R. *et al.* Radiotherapy plus concomitant and adjuvant temozolomide for glioblastoma. *N Engl J Med* **352**, 987-996 (2005). https://doi.org:10.1056/NEJMoa043330

11 Stupp, R. *et al.* Effects of radiotherapy with concomitant and adjuvant temozolomide versus radiotherapy alone on survival in glioblastoma in a randomised phase III study: 5-year analysis of the EORTC-NCIC trial. *Lancet Oncol* **10**, 459-466 (2009). https://doi.org:10.1016/S1470-2045(09)70025-7

12 Weller, M. *et al.* EANO guidelines on the diagnosis and treatment of diffuse gliomas of adulthood. *Nat Rev Clin Oncol* **18**, 170-186 (2021). https://doi.org:10.1038/s41571-020-00447-z

13 Gilbert, M. R. *et al.* A randomized trial of bevacizumab for newly diagnosed glioblastoma. *N Engl J Med* **370**, 699-708 (2014). https://doi.org:10.1056/NEJMoa1308573

14 Taphoorn, M. J. *et al.* Health-Related Quality of Life in a Randomized Phase III Study of Bevacizumab, Temozolomide, and Radiotherapy in Newly Diagnosed Glioblastoma. *J Clin Oncol* **33**, 2166-2175 (2015). https://doi.org:10.1200/JCO.2014.60.3217

15 Ling, A. L. *et al.* Clinical trial links oncolytic immunoactivation to survival in glioblastoma. *Nature* **623**, 157-166 (2023). https://doi.org:10.1038/s41586-023-06623-2

16 Geletneky, K. *et al.* Oncolytic H-1 Parvovirus Shows Safety and Signs of Immunogenic Activity in a First Phase I/IIa Glioblastoma Trial. *Mol Ther* **25**, 2620-2634 (2017). https://doi.org:10.1016/j.ymthe.2017.08.016

17 Desjardins, A. *et al.* Recurrent Glioblastoma Treated with Recombinant Poliovirus. *N Engl J Med* **379**, 150-161 (2018). https://doi.org:10.1056/NEJMoa1716435

18 Pishvaian, M. J. & Brody, J. R. Therapeutic Implications of Molecular Subtyping for Pancreatic Cancer. *Oncology (Williston Park)* **31**, 159-166, 168 (2017).

19 Wang, S. *et al.* Global, regional, and national lifetime risks of developing and dying from gastrointestinal cancers in 185 countries: a population-based systematic analysis of GLOBOCAN. *Lancet Gastroenterol Hepatol* **9**, 229-237 (2024). https://doi.org:10.1016/S2468-1253(23)00366-7

20 Rahib, L., Wehner, M. R., Matrisian, L. M. & Nead, K. T. Estimated Projection of US Cancer Incidence and Death to 2040. *JAMA Netw Open* **4**, e214708 (2021). https://doi.org:10.1001/jamanetworkopen.2021.4708

21 Hartupee, C. *et al.* Pancreatic cancer tumor microenvironment is a major therapeutic barrier and target. *Front Immunol* **15**, 1287459 (2024). https://doi.org:10.3389/fimmu.2024.1287459

22 Stoop, T. F. *et al.* Pancreatic cancer. *Lancet* **405**, 1182-1202 (2025). https://doi.org:10.1016/S0140-6736(25)00261-2

23 Tanaka, H. *et al.* Analyzing the high frequency of false-positive carcinoembryonic antigen elevations in postoperative pancreatic ductal adenocarcinoma. *Langenbecks Arch Surg* **410**, 6 (2024). https://doi.org:10.1007/s00423-024-03577-5

24 Force, U. S. P. S. T. *et al.* Screening for Pancreatic Cancer: US Preventive Services Task Force Reaffirmation Recommendation Statement. *JAMA* **322**, 438-444 (2019). https://doi.org:10.1001/jama.2019.10232

25 Park, W., Chawla, A. & O'Reilly, E. M. Pancreatic Cancer: A Review. *JAMA* **326**, 851-862 (2021). https://doi.org:10.1001/jama.2021.13027

26 Katz, M. H. G. *et al.* Efficacy of Preoperative mFOLFIRINOX vs mFOLFIRINOX Plus Hypofractionated Radiotherapy for Borderline Resectable Adenocarcinoma of the Pancreas: The A021501 Phase 2 Randomized Clinical Trial. *JAMA Oncol* **8**, 1263-1270 (2022). https://doi.org:10.1001/jamaoncol.2022.2319

27 Janssen, Q. P. *et al.* Added Value of Radiotherapy Following Neoadjuvant FOLFIRINOX for Resectable and Borderline Resectable Pancreatic Cancer: A Systematic Review and Meta-Analysis. *Ann Surg Oncol* **28**, 8297-8308 (2021). https://doi.org:10.1245/s10434-021-10276-8

28 Moore, A. R., Rosenberg, S. C., McCormick, F. & Malek, S. RAS-targeted therapies: is the undruggable drugged? *Nat Rev Drug Discov* **19**, 533-552 (2020). https://doi.org:10.1038/s41573-020-0068-6

29 Terrero, G. *et al.* Ipilimumab/Nivolumab Therapy in Patients With Metastatic Pancreatic or Biliary Cancer With Homologous Recombination Deficiency Pathogenic Germline Variants. *JAMA Oncol* **8**, 1-3 (2022). https://doi.org:10.1001/jamaoncol.2022.0611

30 Hu, Z. I. & O'Reilly, E. M. Therapeutic developments in pancreatic cancer. *Nat Rev Gastroenterol Hepatol* **21**, 7-24 (2024). https://doi.org:10.1038/s41575-023-00840-w

31 Hajda, J. *et al.* Phase 2 Trial of Oncolytic H-1 Parvovirus Therapy Shows Safety and Signs of Immune System Activation in Patients With Metastatic Pancreatic Ductal Adenocarcinoma. *Clin Cancer Res* **27**, 5546-5556 (2021). https://doi.org:10.1158/1078-0432.CCR-21-1020

32 Mahalingam, D. *et al.* Pembrolizumab in Combination with the Oncolytic Virus Pelareorep and Chemotherapy in Patients with Advanced Pancreatic Adenocarcinoma: A Phase Ib Study. *Clin Cancer Res* **26**, 71-81 (2020). https://doi.org:10.1158/1078-0432.CCR-19-2078

33 Inc, O. B. (2022).

34 Sullivan, R. *et al.* Global cancer surgery: delivering safe, affordable, and timely cancer surgery. *Lancet Oncol* **16**, 1193-1224 (2015). https://doi.org:10.1016/S1470-2045(15)00223-5

35 DeVita, V. T., Jr. & Chu, E. A history of cancer chemotherapy. *Cancer Res* **68**, 8643-8653 (2008). https://doi.org:10.1158/0008-5472.CAN-07-6611

36 Yin, Q., Shen, J., Zhang, Z., Yu, H. & Li, Y. Reversal of multidrug resistance by stimuli-responsive drug delivery systems for therapy of tumor. *Adv Drug Deliv Rev* **65**, 1699-1715 (2013). https://doi.org:10.1016/j.addr.2013.04.011

37 Davodabadi, F. *et al.* Cancer chemotherapy resistance: Mechanisms and recent breakthrough in targeted drug delivery. *Eur J Pharmacol* **958**, 176013 (2023). https://doi.org:10.1016/j.ejphar.2023.176013

38 Röntgen, W. C. Ueber eine neue Art von Strahlen. *Annalen der Physik* **300**, 1-11 (1898). https://doi.org:10.1002/andp.18983000102

39 Atun, R. *et al.* Expanding global access to radiotherapy. *Lancet Oncol* **16**, 1153-1186 (2015). https://doi.org:10.1016/S1470-2045(15)00222-3

40 Verginadis, II *et al.* Radiotherapy toxicities: mechanisms, management, and future directions. *Lancet* **405**, 338-352 (2025). https://doi.org:10.1016/S0140-6736(24)02319-5

41 Ibanez, B., Melero, A., Montoro, A., San Onofre, N. & Soriano, J. M. Molecular Insights into Radiation Effects and Protective Mechanisms: A Focus on Cellular Damage and Radioprotectors. *Curr Issues Mol Biol* **46**, 12718-12732 (2024). https://doi.org:10.3390/cimb46110755

42 Baskar, R., Dai, J., Wenlong, N., Yeo, R. & Yeoh, K. W. Biological response of cancer cells to radiation treatment. *Front Mol Biosci* **1**, 24 (2014). https://doi.org:10.3389/fmolb.2014.00024

43 Golden, E. B. & Apetoh, L. Radiotherapy and immunogenic cell death. *Semin Radiat Oncol* **25**, 11-17 (2015). https://doi.org:10.1016/j.semradonc.2014.07.005

44 Lonati, L., Barbieri, S., Guardamagna, I., Ottolenghi, A. & Baiocco, G. Radiation-induced cell cycle perturbations: a computational tool validated with flow-cytometry data. *Sci Rep* **11**, 925 (2021). https://doi.org:10.1038/s41598-020-79934-3

45 Craig, D. J. *et al.* The abscopal effect of radiation therapy. *Future Oncol* **17**, 1683-1694 (2021). https://doi.org:10.2217/fon-2020-0994

46 Vanpouille-Box, C. *et al.* DNA exonuclease Trex1 regulates radiotherapy-induced tumour immunogenicity. *Nat Commun* **8**, 15618 (2017). https://doi.org:10.1038/ncomms15618

47 Galluzzi, L., Buque, A., Kepp, O., Zitvogel, L. & Kroemer, G. Immunogenic cell death in cancer and infectious disease. *Nat Rev Immunol* **17**, 97-111 (2017). https://doi.org:10.1038/nri.2016.107

48 Pawlik, T. M. & Keyomarsi, K. Role of cell cycle in mediating sensitivity to radiotherapy. *Int J Radiat Oncol Biol Phys* **59**, 928-942 (2004). https://doi.org:10.1016/j.ijrobp.2004.03.005

49 Baumann, M. *et al.* Radiation oncology in the era of precision medicine. *Nat Rev Cancer* **16**, 234-249 (2016). https://doi.org:10.1038/nrc.2016.18

50 Jaffray, D. A., Knaul, F., Baumann, M. & Gospodarowicz, M. Harnessing progress in radiotherapy for global cancer control. *Nat Cancer* **4**, 1228-1238 (2023). https://doi.org:10.1038/s43018-023-00619-7

51 Nakamura, K. *et al.* Recent advances in radiation oncology: intensity-modulated radiotherapy, a clinical perspective. *Int J Clin Oncol* **19**, 564-569 (2014). https://doi.org:10.1007/s10147-014-0718-y

52 Tanderup, K. *et al.* Advancements in brachytherapy. *Adv Drug Deliv Rev* **109**, 15-25 (2017). https://doi.org:10.1016/j.addr.2016.09.002

53 Mohan, R. A Review of Proton Therapy - Current Status and Future Directions. *Precis Radiat Oncol* **6**, 164-176 (2022). https://doi.org:10.1002/pro6.1149

54 Dracham, C. B., Shankar, A. & Madan, R. Radiation induced secondary malignancies: a review article. *Radiat Oncol J* **36**, 85-94 (2018). https://doi.org:10.3857/roj.2018.00290

55 Shankaran, V. *et al.* IFNgamma and lymphocytes prevent primary tumour development and shape tumour immunogenicity. *Nature* **410**, 1107-1111 (2001). https://doi.org:10.1038/35074122

56 Hanahan, D. & Weinberg, R. A. Hallmarks of cancer: the next generation. *Cell* **144**, 646-674 (2011). https://doi.org:10.1016/j.cell.2011.02.013

57 Tufail, M., Jiang, C. H. & Li, N. Immune evasion in cancer: mechanisms and cutting-edge therapeutic approaches. *Signal Transduct Target Ther* **10**, 227 (2025). https://doi.org:10.1038/s41392-025-02280-1

58 Huang, P. W. & Chang, J. W. Immune checkpoint inhibitors win the 2018 Nobel Prize. *Biomed J* **42**, 299-306 (2019). https://doi.org:10.1016/j.bj.2019.09.002

59 Carlino, M. S., Larkin, J. & Long, G. V. Immune checkpoint inhibitors in melanoma. *Lancet* **398**, 1002-1014 (2021). https://doi.org:10.1016/S0140-6736(21)01206-X

60 Reck, M., Remon, J. & Hellmann, M. D. First-Line Immunotherapy for Non-Small-Cell Lung Cancer. *J Clin Oncol* **40**, 586-597 (2022). https://doi.org:10.1200/JCO.21.01497

61 Pinter, M., Scheiner, B. & Pinato, D. J. Immune checkpoint inhibitors in hepatocellular carcinoma: emerging challenges in clinical practice. *Lancet Gastroenterol Hepatol* **8**, 760-770 (2023). https://doi.org:10.1016/S2468-1253(23)00147-4

62 Dock, G. THE INFLUENCE OF COMPLICATING DISEASES UPON LEUKAEMIA. *THE AMERICAN JOURNAL OF THE MEDICAL SCIENCES* **127**, 565-591 (1904). https://doi.org:10.1097/00000441-190404000-00001

63 Kelly, E. & Russell, S. J. History of oncolytic viruses: genesis to genetic engineering. *Mol Ther* **15**, 651-659 (2007). https://doi.org:10.1038/sj.mt.6300108

64 Southam, C. M. & Moore, A. E. Clinical studies of viruses as antineoplastic agents with particular reference to Egypt 101 virus. *Cancer* **5**, 1025-1034 (1952). https://doi.org:10.1002/1097-0142(195209)5:5<1025::aid-cncr2820050518>3.0.co;2-q

65 Webb, H. E., Wetherley-Mein, G., Smith, C. E. & McMahon, D. Leukaemia and neoplastic processes treated with Langat and Kyasanur Forest disease viruses: a clinical and laboratory study of 28 patients. *Br Med J* **1**, 258-266 (1966). https://doi.org:10.1136/bmj.1.5482.258

66 Cattaneo, R., Miest, T., Shashkova, E. V. & Barry, M. A. Reprogrammed viruses as cancer therapeutics: targeted, armed and shielded. *Nat Rev Microbiol* **6**, 529-540 (2008). https://doi.org:10.1038/nrmicro1927

67 Andtbacka, R. H. *et al.* Talimogene Laherparepvec Improves Durable Response Rate in Patients With Advanced Melanoma. *J Clin Oncol* **33**, 2780-2788 (2015). https://doi.org:10.1200/JCO.2014.58.3377

68 Dittus, K. *et al.* Onkolytische Viren zur Behandlung von Krebserkrankungen. *BIOspektrum* **29**, 585-588 (2023). https://doi.org:10.1007/s12268-023-2030-8

69 Prestwich, R. J. *et al.* The case of oncolytic viruses versus the immune system: waiting on the judgment of Solomon. *Hum Gene Ther* **20**, 1119-1132 (2009). https://doi.org:10.1089/hum.2009.135

70 Lin, D., Shen, Y. & Liang, T. Oncolytic virotherapy: basic principles, recent advances and future directions. *Signal Transduct Target Ther* **8**, 156 (2023). https://doi.org:10.1038/s41392-023-01407-6

71 Zhao, C. *et al.* Dysregulation of JAM-A plays an important role in human tumor progression. *Int J Clin Exp Pathol* **7**, 7242-7248 (2014).

72 Antar, A. A. *et al.* Junctional adhesion molecule-A is required for hematogenous dissemination of reovirus. *Cell Host Microbe* **5**, 59-71 (2009). https://doi.org:10.1016/j.chom.2008.12.001

73 Hartley, A., Kavishwar, G., Salvato, I. & Marchini, A. A Roadmap for the Success of Oncolytic Parvovirus-Based Anticancer Therapies. *Annu Rev Virol* **7**, 537-557 (2020). https://doi.org:10.1146/annurev-virology-012220-023606

74 Krishnamurthy, S., Takimoto, T., Scroggs, R. A. & Portner, A. Differentially regulated interferon response determines the outcome of Newcastle disease virus infection in normal and tumor cell lines. *J Virol* **80**, 5145-5155 (2006). https://doi.org:10.1128/JVI.02618-05

75 Zhao, X., Chester, C., Rajasekaran, N., He, Z. & Kohrt, H. E. Strategic Combinations: The Future of Oncolytic Virotherapy with Reovirus. *Mol Cancer Ther* **15**, 767-773 (2016). https://doi.org:10.1158/1535-7163.MCT-15-0695

76 Kangas, C., Krawczyk, E. & He, B. Oncolytic HSV: Underpinnings of Tumor Susceptibility. *Viruses* **13** (2021). https://doi.org:10.3390/v13071408

77 Veinalde, R. *et al.* Oncolytic measles virus encoding interleukin-12 mediates potent antitumor effects through T cell activation. *Oncoimmunology* **6**, e1285992 (2017). https://doi.org:10.1080/2162402X.2017.1285992

78 Scott, E. M., Duffy, M. R., Freedman, J. D., Fisher, K. D. & Seymour, L. W. Solid Tumor Immunotherapy with T Cell Engager-Armed Oncolytic Viruses. *Macromol Biosci* **18** (2018). https://doi.org:10.1002/mabi.201700187

79 Xie, D. *et al.* Oncolytic adenoviruses expressing checkpoint inhibitors for cancer therapy. *Signal Transduct Target Ther* **8**, 436 (2023). https://doi.org:10.1038/s41392-023-01683-2

80 Bossow, S. *et al.* Armed and targeted measles virus for chemovirotherapy of pancreatic cancer. *Cancer Gene Ther* **18**, 598-608 (2011). https://doi.org:10.1038/cgt.2011.30

81 Marchini, A., Bonifati, S., Scott, E. M., Angelova, A. L. & Rommelaere, J. Oncolytic parvoviruses: from basic virology to clinical applications. *Virol J* **12**, 6 (2015). https://doi.org:10.1186/s12985-014-0223-y

82 Yun, C. O., Hong, J. & Yoon, A. R. Current clinical landscape of oncolytic viruses as novel cancer immunotherapeutic and recent preclinical advancements. *Front Immunol* **13**, 953410 (2022). https://doi.org:10.3389/fimmu.2022.953410

83 Bluming, A. & Ziegler, J. Regression of Burkitt's lymphoma in association with measles infection. *Lancet*, 105–106 (1971).

84 Minta, A. A. *et al.* Progress Toward Measles Elimination - Worldwide, 2000-2023. *MMWR Morb Mortal Wkly Rep* **73**, 1036-1042 (2024). https://doi.org:10.15585/mmwr.mm7345a4

85 Stoneman, E. K. Measles. *JAMA* (2025). https://doi.org:10.1001/jama.2025.14210

86 Günther, K. *Establishing methods to elucidate mechanisms of synergistic radiovirotherapy in refractory tumors*, Ruprecht-Karls-Universität Heidelberg, (2022).

87 Horikami, S. M. & Moyer, S. A. Structure, transcription, and replication of measles virus. *Curr Top Microbiol Immunol* **191**, 35-50 (1995). https://doi.org:10.1007/978-3-642-78621-1_3

88 Rima, B. K. & Duprex, W. P. The measles virus replication cycle. *Curr Top Microbiol Immunol* **329**, 77-102 (2009). https://doi.org:10.1007/978-3-540-70523-9_5

89 Rager, M., Vongpunsawad, S., Duprex, W. P. & Cattaneo, R. Polyploid measles virus with hexameric genome length. *EMBO J* **21**, 2364-2372 (2002). https://doi.org:10.1093/emboj/21.10.2364

90 Suryanarayana, K., Baczko, K., ter Meulen, V. & Wagner, R. R. Transcription inhibition and other properties of matrix proteins expressed by M genes cloned from measles viruses and diseased human brain tissue. *J Virol* **68**, 1532-1543 (1994). https://doi.org:10.1128/JVI.68.3.1532-1543.1994

91 Galanis, E. *et al.* Use of viral fusogenic membrane glycoproteins as novel therapeutic transgenes in gliomas. *Hum Gene Ther* **12**, 811-821 (2001). https://doi.org:10.1089/104303401750148766

92 Ayasoufi, K. & Pfaller, C. K. Seek and hide: the manipulating interplay of measles virus with the innate immune system. *Curr Opin Virol* **41**, 18-30 (2020). https://doi.org:10.1016/j.coviro.2020.03.001

93 Bankamp, B., Takeda, M., Zhang, Y., Xu, W. & Rota, P. A. Genetic characterization of measles vaccine strains. *J Infect Dis* **204 Suppl 1**, S533-548 (2011). https://doi.org:10.1093/infdis/jir097

94 Leber, M. F. *et al.* Engineering and combining oncolytic measles virus for cancer therapy. *Cytokine Growth Factor Rev* **56**, 39-48 (2020). https://doi.org:10.1016/j.cytogfr.2020.07.005

95 Anderson, B. D., Nakamura, T., Russell, S. J. & Peng, K. W. High CD46 receptor density determines preferential killing of tumor cells by oncolytic measles virus. *Cancer Res* **64**, 4919-4926 (2004). https://doi.org:10.1158/0008-5472.CAN-04-0884

96 Andres, F. G. M. *et al.* Measles vaccine attenuation comprises innate immune cell infection and interferon responses. *bioRxiv*, 2025.2006.2009.657851 (2025). https://doi.org:10.1101/2025.06.09.657851

97 Engeland, C. E. & Ungerechts, G. Measles Virus as an Oncolytic Immunotherapy. *Cancers (Basel)* **13** (2021). https://doi.org:10.3390/cancers13030544

98 Packiriswamy, N. *et al.* Oncolytic measles virus therapy enhances tumor antigen-specific T-cell responses in patients with multiple myeloma. *Leukemia* **34**, 3310-3322 (2020). https://doi.org:10.1038/s41375-020-0828-7

99 Forcic, D. *et al.* An Unconventional Case Study of Neoadjuvant Oncolytic Virotherapy for Recurrent Breast Cancer. *Vaccines (Basel)* **12** (2024). https://doi.org:10.3390/vaccines12090958

100 Msaouel, P. *et al.* Clinical Trials with Oncolytic Measles Virus: Current Status and Future Prospects. *Curr Cancer Drug Targets* **18**, 177-187 (2018). https://doi.org:10.2174/1568009617666170222125035

101 Toolan, H. W., Dalldore, G., Barclay, M., Chandra, S. & Moore, A. E. An Unidentified, Filtrable Agent Isolated from Transplanted Human Tumors. *Proc Natl Acad Sci U S A* **46**, 1256-1258 (1960). https://doi.org:10.1073/pnas.46.9.1256

102 Toolan, H. W. Lack of oncogenic effect of the H-viruses for hamsters. *Nature* **214**, 1036 (1967). https://doi.org:10.1038/2141036a0

103 de la Maza, L. M. & Carter, B. J. Inhibition of adenovirus oncogenicity in hamsters by adeno-associated virus DNA. *J Natl Cancer Inst* **67**, 1323-1326 (1981).

104 Rommelaere, J. *et al.* Oncolytic parvoviruses as cancer therapeutics. *Cytokine Growth Factor Rev* **21**, 185-195 (2010). https://doi.org:10.1016/j.cytogfr.2010.02.011

105 Li, L., Cotmore, S. F. & Tattersall, P. Parvoviral left-end hairpin ears are essential during infection for establishing a functional intranuclear transcription template and for efficient progeny genome encapsidation. *J Virol* **87**, 10501-10514 (2013). https://doi.org:10.1128/JVI.01393-13

106 Ferreira, T. *Characterisation of oncolytic H-1 parvovirus cell entry pathways*, Dissertation, Ruperto Carola University Heidelberg, 2021, (2021).

107 Lopez-Bueno, A. *et al.* Host-selected amino acid changes at the sialic acid binding pocket of the parvovirus capsid modulate cell binding affinity and determine virulence. *J Virol* **80**, 1563-1573 (2006). https://doi.org:10.1128/JVI.80.3.1563-1573.2006

108 Angelova, A. *et al.* Oncolytic Rodent Protoparvoviruses Evade a TLR- and RLR-Independent Antiviral Response in Transformed Cells. *Pathogens* **12** (2023). https://doi.org:10.3390/pathogens12040607

109 Alwithenani, A., Hengswat, P. & Chiocca, E. A. Oncolytic viruses as cancer therapeutics: From mechanistic insights to clinical translation. *Mol Ther* **33**, 2217-2228 (2025). https://doi.org:10.1016/j.ymthe.2025.03.035

110 Li, Q. *et al.* The gamble between oncolytic virus therapy and IFN. *Front Immunol* **13**, 971674 (2022). https://doi.org:10.3389/fimmu.2022.971674

111 Geoffroy, K. & Bourgeois-Daigneault, M. C. The pros and cons of interferons for oncolytic virotherapy. *Cytokine Growth Factor Rev* **56**, 49-58 (2020). https://doi.org:10.1016/j.cytogfr.2020.07.002

112 Carty, M., Guy, C. & Bowie, A. G. Detection of Viral Infections by Innate Immunity. *Biochem Pharmacol* **183**, 114316 (2021). https://doi.org:10.1016/j.bcp.2020.114316

113 Ivashkiv, L. B. & Donlin, L. T. Regulation of type I interferon responses. *Nat Rev Immunol* **14**, 36-49 (2014). https://doi.org:10.1038/nri3581

114 Schoggins, J. W. Interferon-Stimulated Genes: What Do They All Do? *Annu Rev Virol* **6**, 567-584 (2019). https://doi.org:10.1146/annurev-virology-092818-015756

115 Zamarin, D. *et al.* Enhancement of oncolytic properties of recombinant newcastle disease virus through antagonism of cellular innate immune responses. *Mol Ther* **17**, 697-706 (2009). https://doi.org:10.1038/mt.2008.286

116 Patel, M. R. *et al.* Vesicular stomatitis virus expressing interferon-beta is oncolytic and promotes antitumor immune responses in a syngeneic murine model of non-small cell lung cancer. *Oncotarget* **6**, 33165-33177 (2015). https://doi.org:10.18632/oncotarget.5320

117 Smith, K. E. R. *et al.* A phase I oncolytic virus trial with vesicular stomatitis virus expressing human interferon beta and tyrosinase related protein 1 administered intratumorally and intravenously in uveal melanoma: safety, efficacy, and T cell responses. *Front Immunol* **14**, 1279387 (2023). https://doi.org:10.3389/fimmu.2023.1279387

118 Maroun, J. *et al.* Designing and building oncolytic viruses. *Future Virol* **12**, 193-213 (2017). https://doi.org:10.2217/fvl-2016-0129

119 Russell, S. J. *et al.* Remission of disseminated cancer after systemic oncolytic virotherapy. *Mayo Clin Proc* **89**, 926-933 (2014). https://doi.org:10.1016/j.mayocp.2014.04.003

120 Appleton, E., Chiocca, E. A., Ungerechts, G., Melcher, A. & Vile, R. Oncolytic viruses as anticancer agents: clinical progress and remaining challenges. *Lancet* **406**, 1295-1312 (2025). https://doi.org:10.1016/S0140-6736(25)01206-1

121 Martin, N. T. & Bell, J. C. Oncolytic Virus Combination Therapy: Killing One Bird with Two Stones. *Mol Ther* **26**, 1414-1422 (2018). https://doi.org:10.1016/j.ymthe.2018.04.001

122 De Ruysscher, D. *et al.* Radiotherapy toxicity. *Nat Rev Dis Primers* **5**, 13 (2019). https://doi.org:10.1038/s41572-019-0064-5

123 Lawler, S. E., Speranza, M. C., Cho, C. F. & Chiocca, E. A. Oncolytic Viruses in Cancer Treatment: A Review. *JAMA Oncol* **3**, 841-849 (2017). https://doi.org:10.1001/jamaoncol.2016.2064

124 Touchefeu, Y., Vassaux, G. & Harrington, K. J. Oncolytic viruses in radiation oncology. *Radiother Oncol* **99**, 262-270 (2011). https://doi.org:10.1016/j.radonc.2011.05.078

125 O'Cathail, S. M. *et al.* Combining Oncolytic Adenovirus with Radiation-A Paradigm for the Future of Radiosensitization. *Front Oncol* **7**, 153 (2017). https://doi.org:10.3389/fonc.2017.00153

126 Kawabe, S. *et al.* Adenovirus-mediated wild-type p53 gene expression radiosensitizes non-small cell lung cancer cells but not normal lung fibroblasts. *Int J Radiat Biol* **77**, 185-194 (2001). https://doi.org:10.1080/09553000010008540

127 Geoerger, B. *et al.* Potentiation of radiation therapy by the oncolytic adenovirus dl1520 (ONYX-015) in human malignant glioma xenografts. *Br J Cancer* **89**, 577-584 (2003). https://doi.org:10.1038/sj.bjc.6601102

128 Dai, M. H. *et al.* Oncolytic vaccinia virus in combination with radiation shows synergistic antitumor efficacy in pancreatic cancer. *Cancer Lett* **344**, 282-290 (2014). https://doi.org:10.1016/j.canlet.2013.11.007

129 Monga, V. *et al.* Intratumoral talimogene laherparepvec injection with concurrent preoperative radiation in patients with locally advanced soft-tissue sarcoma of the trunk and extremities: phase IB/II trial. *J Immunother Cancer* **9** (2021). https://doi.org:10.1136/jitc-2021-003119

130 Markert, J. M. *et al.* A phase 1 trial of oncolytic HSV-1, G207, given in combination with radiation for recurrent GBM demonstrates safety and radiographic responses. *Mol Ther* **22**, 1048-1055 (2014). https://doi.org:10.1038/mt.2014.22

131 Toulmonde, M. *et al.* Randomized phase 2 trial of intravenous oncolytic virus JX-594 combined with low-dose cyclophosphamide in patients with advanced soft-tissue sarcoma. *J Hematol Oncol* **15**, 149 (2022). https://doi.org:10.1186/s13045-022-01370-9

132 Gallego Perez-Larraya, J. *et al.* Oncolytic DNX-2401 Virus for Pediatric Diffuse Intrinsic Pontine Glioma. *N Engl J Med* **386**, 2471-2481 (2022). https://doi.org:10.1056/NEJMoa2202028

133 Liu, C. *et al.* Combination of measles virus virotherapy and radiation therapy has synergistic activity in the treatment of glioblastoma multiforme. *Clin Cancer Res* **13**, 7155-7165 (2007). https://doi.org:10.1158/1078-0432.CCR-07-1306

134 Rajaraman, S. *et al.* Measles Virus-Based Treatments Trigger a Pro-inflammatory Cascade and a Distinctive Immunopeptidome in Glioblastoma. *Mol Ther Oncolytics* **12**, 147-161 (2019). https://doi.org:10.1016/j.omto.2018.12.010

135 Derani, J. *Combining radiation and oncolytic measles virus for the treatment of refractory tumors*, Dissertation, Ruprecht-Karls-University Heidelberg, 2023, (2023).

136 Liu, C., Hasegawa, K., Russell, S. J., Sadelain, M. & Peng, K. W. Prostate-specific membrane antigen retargeted measles virotherapy for the treatment of prostate cancer. *Prostate* **69**, 1128-1141 (2009). https://doi.org:10.1002/pros.20962

137 Baumann, D. *et al.* Proimmunogenic impact of MEK inhibition synergizes with agonist anti-CD40 immunostimulatory antibodies in tumor therapy. *Nat Commun* **11**, 2176 (2020). https://doi.org:10.1038/s41467-020-15979-2

138 Heller, A. *et al.* Establishment and Characterization of a Novel Cell Line, ASAN-PaCa, Derived From Human Adenocarcinoma Arising in Intraductal Papillary Mucinous Neoplasm of the Pancreas. *Pancreas* **45**, 1452-1460 (2016). https://doi.org:10.1097/MPA.0000000000000673

139 Castro, F. *et al.* High-throughput SNP-based authentication of human cell lines. *Int J Cancer* **132**, 308-314 (2013). https://doi.org:10.1002/ijc.27675

140 Schmitt, M. & Pawlita, M. High-throughput detection and multiplex identification of cell contaminations. *Nucleic Acids Res* **37**, e119 (2009). https://doi.org:10.1093/nar/gkp581

141 Roehm, N. W., Rodgers, G. H., Hatfield, S. M. & Glasebrook, A. L. An improved colorimetric assay for cell proliferation and viability utilizing the tetrazolium salt XTT. *J Immunol Methods* **142**, 257-265 (1991). https://doi.org:10.1016/0022-1759(91)90114-u

142 Ware, M. J. *et al.* Generation of Homogenous Three-Dimensional Pancreatic Cancer Cell Spheroids Using an Improved Hanging Drop Technique. *Tissue Eng Part C Methods* **22**, 312-321 (2016). https://doi.org:10.1089/ten.TEC.2015.0280

143 Piecyk, M., Fauvre, J., Duret, C., Chaveroux, C. & Ferraro-Peyret, C. SUrface SEnsing of Translation (SUnSET), a Method Based on Western Blot Assessing Protein Synthesis Rates in vitro. *Bio Protoc* **14**, e4933 (2024). https://doi.org:10.21769/BioProtoc.4933

144 Heidbuechel, J. P. W. & Engeland, C. E. Paramyxoviruses for Tumor-targeted Immunomodulation: Design and Evaluation Ex Vivo. *J Vis Exp* (2019). https://doi.org:10.3791/58651

145 Reisinger, E. *et al.* OTP: An automatized system for managing and processing NGS data. *J Biotechnol* **261**, 53-62 (2017). https://doi.org:10.1016/j.jbiotec.2017.08.006

146 Chen, Y., Chen, L., Lun, A. T. L., Baldoni, P. L. & Smyth, G. K. edgeR v4: powerful differential analysis of sequencing data with expanded functionality and improved support for small counts and larger datasets. *Nucleic Acids Res* **53** (2025). https://doi.org:10.1093/nar/gkaf018

147 Robinson, M. D., McCarthy, D. J. & Smyth, G. K. edgeR: a Bioconductor package for differential expression analysis of digital gene expression data. *Bioinformatics* **26**, 139-140 (2010). https://doi.org:10.1093/bioinformatics/btp616

148 Wickham, H. *Ggplot2: Elegant graphics for data analysis*. 2 edn, (Springer International Publishing, 2016).

149 Liberzon, A. *et al.* The Molecular Signatures Database (MSigDB) hallmark gene set collection. *Cell Syst* **1**, 417-425 (2015). https://doi.org:10.1016/j.cels.2015.12.004

150 Subramanian, A. *et al.* Gene set enrichment analysis: a knowledge-based approach for interpreting genome-wide expression profiles. *Proc Natl Acad Sci U S A* **102**, 15545-15550 (2005). https://doi.org:10.1073/pnas.0506580102

151 Matsumoto, M. & Seya, T. TLR3: interferon induction by double-stranded RNA including poly(I:C). *Adv Drug Deliv Rev* **60**, 805-812 (2008). https://doi.org:10.1016/j.addr.2007.11.005

152 Field, A. K., Tytell, A. A., Lampson, G. P. & Hilleman, M. R. Inducers of interferon and host resistance. II. Multistranded synthetic polynucleotide complexes. *Proc Natl Acad Sci U S A* **58**, 1004-1010 (1967). https://doi.org:10.1073/pnas.58.3.1004

153 Lei, S., Mao, Y., Yang, Q., Yan, H. & Wang, J. Trends in pancreatic cancer incidence, prevalence, and survival outcomes by histological subtypes: a retrospective cohort study. *Gastroenterol Rep (Oxf)* **13**, goaf030 (2025). https://doi.org:10.1093/gastro/goaf030

154 Davis, F. G. *et al.* Glioblastoma incidence rate trends in Canada and the United States compared with England, 1995-2015. *Neuro Oncol* **22**, 301-302 (2020). https://doi.org:10.1093/neuonc/noz203

155 Geletneky, K., Hartkopf, A. D., Krempien, R., Rommelaere, J. & Schlehofer, J. R. Improved killing of human high-grade glioma cells by combining ionizing radiation with oncolytic parvovirus H-1 infection. *J Biomed Biotechnol* **2010**, 350748 (2010). https://doi.org:10.1155/2010/350748

156 Bonhomme, D. & Poirier, E. Z. Early signaling pathways in virus-infected cells. *Curr Opin Virol* **66**, 101411 (2024). https://doi.org:10.1016/j.coviro.2024.101411

157 Huang, C. *et al.* An integrated analysis for long noncoding RNAs and microRNAs with the mediated competing endogenous RNA network in papillary renal cell carcinoma. *Onco Targets Ther* **10**, 4037-4050 (2017). https://doi.org:10.2147/OTT.S141951

158 Yuan, N. *et al.* Integrative analysis of lncRNAs and miRNAs with coding RNAs associated with ceRNA crosstalk network in triple negative breast cancer. *Onco Targets Ther* **10**, 5883-5897 (2017). https://doi.org:10.2147/OTT.S149308

159 Statello, L., Guo, C. J., Chen, L. L. & Huarte, M. Gene regulation by long non-coding RNAs and its biological functions. *Nat Rev Mol Cell Biol* **22**, 96-118 (2021). https://doi.org:10.1038/s41580-020-00315-9

160 Zhang, J. *et al.* MicroRNA-211 expression is down-regulated and associated with poor prognosis in human glioma. *J Neurooncol* **133**, 553-559 (2017). https://doi.org:10.1007/s11060-017-2464-2

161 Hamidi, A. A. *et al.* Molecular mechanisms of microRNA-216a during tumor progression. *Cancer Cell Int* **23**, 19 (2023). https://doi.org:10.1186/s12935-023-02865-2

162 Zhu, Y., Zhao, H., Feng, L. & Xu, S. MicroRNA-217 inhibits cell proliferation and invasion by targeting Runx2 in human glioma. *Am J Transl Res* **8**, 1482-1491 (2016).

163 Sachdeva, M. & Mo, Y. Y. MicroRNA-145 suppresses cell invasion and metastasis by directly targeting mucin 1. *Cancer Res* **70**, 378-387 (2010). https://doi.org:10.1158/0008-5472.CAN-09-2021

164 Kim, Y. J. *et al.* Time-sequential change in immune-related gene expression after irradiation in glioblastoma: next-generation sequencing analysis. *Anim Cells Syst (Seoul)* **25**, 245-254 (2021). https://doi.org:10.1080/19768354.2021.1954550

165 Chaturvedi, G. *et al.* Dose-Dependent Transcriptional Response to Ionizing Radiation Is Orchestrated with DNA Repair within the Nuclear Space. *Int J Mol Sci* **25** (2024). https://doi.org:10.3390/ijms25020970

166 Neumaier, T. *et al.* Evidence for formation of DNA repair centers and dose-response nonlinearity in human cells. *Proc Natl Acad Sci U S A* **109**, 443-448 (2012). https://doi.org:10.1073/pnas.1117849108

167 Huang, R. X. & Zhou, P. K. DNA damage response signaling pathways and targets for radiotherapy sensitization in cancer. *Signal Transduct Target Ther* **5**, 60 (2020). https://doi.org:10.1038/s41392-020-0150-x

168 Liu, Y., Beyer, A. & Aebersold, R. On the Dependency of Cellular Protein Levels on mRNA Abundance. *Cell* **165**, 535-550 (2016). https://doi.org:10.1016/j.cell.2016.03.014

169 Kurokawa, C. & Galanis, E. Interferon signaling predicts response to oncolytic virotherapy. *Oncotarget* **10**, 1544-1545 (2019). https://doi.org:10.18632/oncotarget.26679

170 Moerdyk-Schauwecker, M. *et al.* Resistance of pancreatic cancer cells to oncolytic vesicular stomatitis virus: role of type I interferon signaling. *Virology* **436**, 221-234 (2013). https://doi.org:10.1016/j.virol.2012.11.014

171 Zhang, L. F. *et al.* Combination of vaccine-strain measles and mumps virus synergistically kills a wide range of human hematological cancer cells: Special focus on acute myeloid leukemia. *Cancer Lett* **354**, 272-280 (2014). https://doi.org:10.1016/j.canlet.2014.08.034

172 Le Boeuf, F. *et al.* Synergistic interaction between oncolytic viruses augments tumor killing. *Mol Ther* **18**, 888-895 (2010). https://doi.org:10.1038/mt.2010.44

173 Tysome, J. R. *et al.* A novel therapeutic regimen to eradicate established solid tumors with an effective induction of tumor-specific immunity. *Clin Cancer Res* **18**, 6679-6689 (2012). https://doi.org:10.1158/1078-0432.CCR-12-0979

174 Alkassar, M. *et al.* The combined effects of oncolytic reovirus plus Newcastle disease virus and reovirus plus parvovirus on U87 and U373 cells in vitro and in vivo. *J Neurooncol* **104**, 715-727 (2011). https://doi.org:10.1007/s11060-011-0606-5

175 Ginting, T. E. *et al.* Antiviral interferons induced by Newcastle disease virus (NDV) drive a tumor-selective apoptosis. *Sci Rep* **9**, 15160 (2019). https://doi.org:10.1038/s41598-019-51465-6

176 Taha, Z. *et al.* Complementary dual-virus strategy drives synthetic target and cognate T-cell engager expression for endogenous-antigen agnostic immunotherapy. *Nat Commun* **15**, 7267 (2024). https://doi.org:10.1038/s41467-024-51498-0

177 Pol, J. G. *et al.* Preclinical evaluation of a MAGE-A3 vaccination utilizing the oncolytic Maraba virus currently in first-in-human trials. *Oncoimmunology* **8**, e1512329 (2019). https://doi.org:10.1080/2162402X.2018.1512329

178 Stern-Ginossar, N., Thompson, S. R., Mathews, M. B. & Mohr, I. Translational Control in Virus-Infected Cells. *Cold Spring Harb Perspect Biol* **11** (2019). https://doi.org:10.1101/cshperspect.a033001

179 Ventoso, I., Berlanga, J. J. & Almendral, J. M. Translation control by protein kinase R restricts minute virus of mice infection: role in parvovirus oncolysis. *J Virol* **84**, 5043-5051 (2010). https://doi.org:10.1128/JVI.02188-09

180 Du, Y., Wang, C. & Zhang, Y. Viral Coinfections. *Viruses* **14** (2022). https://doi.org:10.3390/v14122645

181 Rozman, B., Fisher, T. & Stern-Ginossar, N. Translation-A tug of war during viral infection. *Mol Cell* **83**, 481-495 (2023). https://doi.org:10.1016/j.molcel.2022.10.012

182 Hoang, H. D., Neault, S., Pelin, A. & Alain, T. Emerging translation strategies during virus-host interaction. *Wiley Interdiscip Rev RNA* **12**, e1619 (2021). https://doi.org:10.1002/wrna.1619

183 Vitiello, A. *et al.* Simultaneous Expression of Different Therapeutic Genes by Infection with Multiple Oncolytic HSV-1 Vectors. *Biomedicines* **12** (2024). https://doi.org:10.3390/biomedicines12071577

184 Zhou, P. K., Sun, Y. & An, J. Interaction between viral proteins and hosts and its disturbance in the cellular responses to ionising radiation. *Int J Radiat Biol* **85**, 587-597 (2009). https://doi.org:10.1080/09553000902954512

185 Touchefeu, Y. *et al.* Optimising measles virus-guided radiovirotherapy with external beam radiotherapy and specific checkpoint kinase 1 inhibition. *Radiother Oncol* **108**, 24-31 (2013). https://doi.org:10.1016/j.radonc.2013.05.036

186 Dingli, D. *et al.* Image-guided radiovirotherapy for multiple myeloma using a recombinant measles virus expressing the thyroidal sodium iodide symporter. *Blood* **103**, 1641-1646 (2004). https://doi.org:10.1182/blood-2003-07-2233

187 Li, H., Peng, K. W. & Russell, S. J. Oncolytic measles virus encoding thyroidal sodium iodide symporter for squamous cell cancer of the head and neck radiovirotherapy. *Hum Gene Ther* **23**, 295-301 (2012). https://doi.org:10.1089/hum.2011.128

188 Schipler, A. & Iliakis, G. DNA double-strand-break complexity levels and their possible contributions to the probability for error-prone processing and repair pathway choice. *Nucleic Acids Res* **41**, 7589-7605 (2013). https://doi.org:10.1093/nar/gkt556

189 Chen, S., Liu, F., Yang, A. & Shang, K. For better or worse: crosstalk of parvovirus and host DNA damage response. *Front Immunol* **15**, 1324531 (2024). https://doi.org:10.3389/fimmu.2024.1324531

190 Aref, S. *et al.* Type 1 Interferon Responses Underlie Tumor-Selective Replication of Oncolytic Measles Virus. *Mol Ther* **28**, 1043-1055 (2020). https://doi.org:10.1016/j.ymthe.2020.01.027

191 Galluzzi, L. *et al.* Consensus guidelines for the definition, detection and interpretation of immunogenic cell death. *J Immunother Cancer* **8** (2020). https://doi.org:10.1136/jitc-2019-000337

192 Villaverde, M. S., Gil-Cardeza, M. L., Glikin, G. C. & Finocchiaro, L. M. Interferon-beta lipofection II. Mechanisms involved in cell death and bystander effect induced by cationic lipid-mediated interferon-beta gene transfer to human tumor cells. *Cancer Gene Ther* **19**, 420-430 (2012). https://doi.org:10.1038/cgt.2012.19

193 Syedbasha, M. & Egli, A. Interferon Lambda: Modulating Immunity in Infectious Diseases. *Front Immunol* **8**, 119 (2017). https://doi.org:10.3389/fimmu.2017.00119

194 Sommereyns, C., Paul, S., Staeheli, P. & Michiels, T. IFN-lambda (IFN-lambda) is expressed in a tissue-dependent fashion and primarily acts on epithelial cells in vivo. *PLoS Pathog* **4**, e1000017 (2008). https://doi.org:10.1371/journal.ppat.1000017

195 Wang, F. *et al.* Activation of Toll-like receptor 7 regulates the expression of IFN-lambda1, p53, PTEN, VEGF, TIMP-1 and MMP-9 in pancreatic cancer cells. *Mol Med Rep* **13**, 1807-1812 (2016). https://doi.org:10.3892/mmr.2015.4730

196 Ivashkevich, A., Redon, C. E., Nakamura, A. J., Martin, R. F. & Martin, O. A. Use of the gamma-H2AX assay to monitor DNA damage and repair in translational cancer research. *Cancer Lett* **327**, 123-133 (2012). https://doi.org:10.1016/j.canlet.2011.12.025

197 Fell, V. L. & Schild-Poulter, C. The Ku heterodimer: function in DNA repair and beyond. *Mutat Res Rev Mutat Res* **763**, 15-29 (2015). https://doi.org:10.1016/j.mrrev.2014.06.002

198 McIlwain, D. R., Berger, T. & Mak, T. W. Caspase functions in cell death and disease. *Cold Spring Harb Perspect Biol* **5**, a008656 (2013). https://doi.org:10.1101/cshperspect.a008656

199 Anker, S. C. *et al.* Oncolytic Measles Virus Encoding MicroRNA for Targeted RNA Interference. *Viruses* **15** (2023). https://doi.org:10.3390/v15020308

200 Runge, S. *et al.* In vivo ligands of MDA5 and RIG-I in measles virus-infected cells. *PLoS Pathog* **10**, e1004081 (2014). https://doi.org:10.1371/journal.ppat.1004081

201 Kon, T. *et al.* Oncolytic virus-mediated tumor radiosensitization in mice through DNA-PKcs-specific shRNA. *Transl Cancer Res* **1**, 4-14 (2012). https://doi.org:10.3978/j.issn.2218-676X.2012.05.02

202 Rezaeian, A. H., Khanbabaei, H. & Calin, G. A. Therapeutic Potential of the miRNA-ATM Axis in the Management of Tumor Radioresistance. *Cancer Res* **80**, 139-150 (2020). https://doi.org:10.1158/0008-5472.CAN-19-1807

203 Dash, S., Dash, C. & Pandhare, J. Therapeutic Significance of microRNA-Mediated Regulation of PARP-1 in SARS-CoV-2 Infection. *Noncoding RNA* **7** (2021). https://doi.org:10.3390/ncrna7040060

204 Liu, L. *et al.* Recombinant oncolytic virus NDV-anti-VEGFR2 enhances radiotherapy sensitivity in NSCLC by targeting VEGF signaling and impairing DNA repair. *Gene Ther* **32**, 517-528 (2025). https://doi.org:10.1038/s41434-025-00540-x

205 Chiu, M. *et al.* Combination therapy with oncolytic viruses and immune checkpoint inhibitors. *Expert Opin Biol Ther* **20**, 635-652 (2020). https://doi.org:10.1080/14712598.2020.1729351

206 Wongariyapak, A., Roulstone, V., Melcher, A. A., Pedersen, M. & Harrington, K. J. Combination strategies incorporating oncolytic viruses and immune checkpoint inhibitors

for advanced melanoma: what is the evidence? *Ann Transl Med* **11**, 369 (2023). https://doi.org:10.21037/atm-2023-5

207 Jhawar, S. R. *et al.* Combination oncolytic virus, radiation therapy, and immune checkpoint inhibitor treatment in anti-PD-1-refractory cancer. *J Immunother Cancer* **11** (2023). https://doi.org:10.1136/jitc-2023-006780

208 Bayat Mokhtari, R. *et al.* Combination therapy in combating cancer. *Oncotarget* **8**, 38022-38043 (2017). https://doi.org:10.18632/oncotarget.16723

209 Conroy, T. *et al.* FOLFIRINOX versus gemcitabine for metastatic pancreatic cancer. *N Engl J Med* **364**, 1817-1825 (2011). https://doi.org:10.1056/NEJMoa1011923

210 Tempero, M. A. *et al.* Adjuvant nab-Paclitaxel + Gemcitabine in Resected Pancreatic Ductal Adenocarcinoma: Results From a Randomized, Open-Label, Phase III Trial. *J Clin Oncol* **41**, 2007-2019 (2023). https://doi.org:10.1200/JCO.22.01134

211 McAleavey, P. G., Walls, G. M. & Chalmers, A. J. Radiotherapy-drug combinations in the treatment of glioblastoma: a brief review. *CNS Oncol* **11**, CNS86 (2022). https://doi.org:10.2217/cns-2021-0015

212 Yadav, B., Wennerberg, K., Aittokallio, T. & Tang, J. Searching for Drug Synergy in Complex Dose-Response Landscapes Using an Interaction Potency Model. *Comput Struct Biotechnol J* **13**, 504-513 (2015). https://doi.org:10.1016/j.csbj.2015.09.001

213 Ianevski, A., Giri, A. K. & Aittokallio, T. SynergyFinder 3.0: an interactive analysis and consensus interpretation of multi-drug synergies across multiple samples. *Nucleic Acids Res* **50**, W739-W743 (2022). https://doi.org:10.1093/nar/gkac382

214 Zheng, S. *et al.* SynergyFinder Plus: Toward Better Interpretation and Annotation of Drug Combination Screening Datasets. *Genomics Proteomics Bioinformatics* **20**, 587-596 (2022). https://doi.org:10.1016/j.gpb.2022.01.004

215 Chou, T. C. & Talalay, P. Quantitative analysis of dose-effect relationships: the combined effects of multiple drugs or enzyme inhibitors. *Adv Enzyme Regul* **22**, 27-55 (1984). https://doi.org:10.1016/0065-2571(84)90007-4

216 Liu, T., Chu, T., Luo, X. & Zhao, H. Building a unified model for drug synergy analysis powered by large language models. *Nat Commun* **16**, 4537 (2025). https://doi.org:10.1038/s41467-025-59822-y

217 Palmer, A. C. & Sorger, P. K. Combination Cancer Therapy Can Confer Benefit via Patient-to-Patient Variability without Drug Additivity or Synergy. *Cell* **171**, 1678-1691 e1613 (2017). https://doi.org:10.1016/j.cell.2017.11.009

218 Kloker, L. D., Yurttas, C. & Lauer, U. M. Three-dimensional tumor cell cultures employed in virotherapy research. *Oncolytic Virother* **7**, 79-93 (2018). https://doi.org:10.2147/OV.S165479

219 Tsukamoto, Y. *et al.* Patient-Derived Ex Vivo Cultures and Endpoint Assays with Surrogate Biomarkers in Functional Testing for Prediction of Therapeutic Response. *Cancers (Basel)* **15** (2023). https://doi.org:10.3390/cancers15164104

220 Senrung, A. *et al.* 3D tumor spheroids: morphological alterations a yardstick to anti-cancer drug response. *In Vitro Model* **2**, 219-248 (2023). https://doi.org:10.1007/s44164-023-00059-8

221 Mao, Y. & Hu, H. Establishment of advanced tumor organoids with emerging innovative technologies. *Cancer Lett* **598**, 217122 (2024). https://doi.org:10.1016/j.canlet.2024.217122

222 Sivakumar, R. *et al.* Organotypic tumor slice cultures provide a versatile platform for immuno-oncology and drug discovery. *Oncoimmunology* **8**, e1670019 (2019). https://doi.org:10.1080/2162402X.2019.1670019

223 Le Boeuf, F. *et al.* Reovirus FAST Protein Enhances Vesicular Stomatitis Virus Oncolytic Virotherapy in Primary and Metastatic Tumor Models. *Mol Ther Oncolytics* **6**, 80-89 (2017). https://doi.org:10.1016/j.omto.2017.08.001

224 Wollner, A. *et al.* Use of Tissue Specimens from Stereotactic Biopsies for Patient-Derived GBM Organoid-Based Drug Testing. *Cells* **14** (2025). https://doi.org:10.3390/cells14100701

225 Stavrakaki, E. *et al.* An autologous ex vivo model for exploring patient-specific responses to viro-immunotherapy in glioblastoma. *Cell Rep Methods* **4**, 100716 (2024). https://doi.org:10.1016/j.crmeth.2024.100716

226 Lal, S. & Raffel, C. Protocols to Manufacture an Oncolytic Measles Virus-Sensitive Immunocompetent Mouse Model of Medulloblastoma. *Methods Mol Biol* **2423**, 165-177 (2022). https://doi.org:10.1007/978-1-0716-1952-0_16

227 Vincent, S. *et al.* Restriction of measles virus RNA synthesis by a mouse host cell line: trans-complementation by polymerase components or a human cellular factor(s). *J Virol* **76**, 6121-6130 (2002). https://doi.org:10.1128/jvi.76.12.6121-6130.2002

228 Mrkic, B. *et al.* Measles virus spread and pathogenesis in genetically modified mice. *J Virol* **72**, 7420-7427 (1998). https://doi.org:10.1128/JVI.72.9.7420-7427.1998

229 Mura, M. *et al.* hCD46 receptor is not required for measles vaccine Schwarz strain replication in vivo: Type-I IFN is the species barrier in mice. *Virology* **524**, 151-159 (2018). https://doi.org:10.1016/j.virol.2018.08.014

230 Moffitt, R. A. *et al.* Virtual microdissection identifies distinct tumor- and stroma-specific subtypes of pancreatic ductal adenocarcinoma. *Nat Genet* **47**, 1168-1178 (2015). https://doi.org:10.1038/ng.3398

231 Vienne, M. *et al.* Minute virus of mice shows oncolytic activity against pancreatic cancer cells exhibiting a mesenchymal phenotype. *Mol Ther Oncol* **32**, 200780 (2024). https://doi.org:10.1016/j.omton.2024.200780

232 Toolan, H. W., Saunders, E. L., Southam, C. M., Moore, A. E. & Levin, A. G. H-1 Virus Viremia in the Human. *Proc Soc Exp Biol Med* **119**, 711-715 (1965). https://doi.org:10.3181/00379727-119-30278

233 Heinzerling, L. *et al.* Oncolytic measles virus in cutaneous T-cell lymphomas mounts antitumor immune responses in vivo and targets interferon-resistant tumor cells. *Blood* **106**, 2287-2294 (2005). https://doi.org:10.1182/blood-2004-11-4558

234 Dispenzieri, A. *et al.* Phase I trial of systemic administration of Edmonston strain of measles virus genetically engineered to express the sodium iodide symporter in patients with recurrent or refractory multiple myeloma. *Leukemia* **31**, 2791-2798 (2017). https://doi.org:10.1038/leu.2017.120

235 Galanis, E. *et al.* Phase I trial of intraperitoneal administration of an oncolytic measles virus strain engineered to express carcinoembryonic antigen for recurrent ovarian cancer. *Cancer Res* **70**, 875-882 (2010). https://doi.org:10.1158/0008-5472.CAN-09-2762

236 Galanis, E. *et al.* Carcinoembryonic antigen-expressing oncolytic measles virus derivative in recurrent glioblastoma: a phase 1 trial. *Nat Commun* **15**, 493 (2024). https://doi.org:10.1038/s41467-023-43076-7

237 Kurokawa, C. *et al.* Constitutive Interferon Pathway Activation in Tumors as an Efficacy Determinant Following Oncolytic Virotherapy. *J Natl Cancer Inst* **110**, 1123-1132 (2018). https://doi.org:10.1093/jnci/djy033

238 Corbyn, Z. This scientist treated her own cancer with viruses she grew in the lab. *Nature* **635**, 529-530 (2024). https://doi.org:10.1038/d41586-024-03647-0

Scientific contributions

Publications

Anker, S. C., Szczeponik, M. G., Dessila, J., **Dittus, K.,** Engeland, C. E., Jäger, D., Ungerechts, G., & Leber, M. F. (2023). Oncolytic Measles Virus Encoding MicroRNA for Targeted RNA Interference. Viruses, 15(2), 308. https://doi.org/10.3390/v15020308

Dittus, K., Eilert, A. E., Szczeponik, M. G., Hastedt, J. K., Ungerechts, G., & Leber, M. F. (2023). Onkolytische Viren zur Behandlung von Krebserkrankungen. BIOspektrum, 29(6), 585-588. https://doi.org/10.1007/s12268-023-2030-8

Conference contributions

J.M. Förster, **K. Günther**, K. Zaoui, C. Ball, A. L. Angelova, H. Glimm, J. Debus, D. Jäger, A. Abdollahi, A. Nowrouzi, C. E. Engeland, M. F. Leber, and G. Ungerechts.
Combining radiation and oncolytic measles virus for treatment of refractory tumors.
Poster presentation. 13th International Oncolytic Virus Conference,
November 5–7, 2021, Sedona, AZ/USA.

K. Dittus, J.M. Derani, K. Plath, C. E. Engeland, L. Daeffler, G. Ungerechts and M. F. Leber
Immunoprofiling in the scope of radiovirotherapy
Poster presentation, 15th International Oncolytic Virus Conference,
November, 11-14, 2023, Banff, AB/Canada

K. Dittus, J.M. Derani, K. Plath, A. Angelova, C. E. Engeland, L. Daeffler, G. Ungerechts and M. F. Leber
Deciphering and modifying radiovirotherapy
Poster presentation, 16th International Oncolytic Virus Conference,
October, 27-30, 2024, Rotterdam, Netherlands

Acknowledgments

At last, there are many people who need to be acknowledged as part of my PhD journey.

First of all, I want to thank my thesis advisory committee, Stefan Wiemann, Guy Ungerechts, Mathias Leber und Laurent Daeffler, for valuable feedback and encouragement throughout the PhD. Also, I want to thank the members of my examination committee: Guy Ungerechts and Stefan Wiemann, also for reviewing this thesis, Benedikt Brors, also for being the chairperson of the committee, and Marco Binder.

Then, I owe major “thank yous”

To Guy Ungerechts. I am especially thankful for all the opportunities I was given throughout the last 5 years in the CCU. In addition to being able to perform my thesis work, going on conference trips and receiving scientific advice, I was able to grow as a person, foster ideas and participate in truly meaningful work for the benefit of cancer patients. The atmosphere is inspiring and your drive is contagious (pun intended).

To Mathias Leber I am deeply grateful. For taking time under very challenging conditions, for providing feedback when needed, for proofreading the thesis and for trusting me. I appreciate your honest and value-driven research and management approach and am very thankful for the atmosphere you foster. I am looking forward to continuing good communication and team work!

To Dirk Nettelbeck for valued scientific feedback, catching OV-enthusiasm and reminding us of the, arguably, second-best oncolytic virus.

To the PROTOVEC team: Assia Angelova, Jean Rommelaere, Estelle Santiago and Laurent Daeffler for valuable feedback, sharing PV knowledge, good discussions and keeping the hope up in light of not the greatest results. A special Thank you to Laurent and Estelle, for hosting me in Straßbourg and making me feel very welcome!

To Barbara Leuchs for providing the parvovirus stocks. To Ina Kurth, Mareike Roscher and Rosemarie Euler-Lange for enabling radiation with the MultiRad system. To the light micrsocopy facility, especially Manuala Brom, for providing great support. To the NGS and OD core facilities for enabling the RNA sequencing experiment.

To the whole AdMe Club for interesting journal clubs and lab meetings, for being supportive and helping each other out. Especially to you, Jonny, for your engaging presentations, thoughtful feedback and constant IFN advice; you are scientist role model!

To team NCT, past and present, Birgit, Hanno, Judith, Marie, Jan, Juliane, Silja, Marie K, Adrian, Pierre, Sergej, Jane, Laura, Daniel, Emily, Eva and Lilli. Working with each and every one of you was a true joy. Cherished scientific and non-scientific discussions, uncountable sly remarks and even more heartfelt laughs – with colleagues like you, Mondays really aren't bad! (and cake Tuesdays even less so). A special thank you to Marie, for RNAseqing together, being bread buddies and colleague-friends ;) To Juliane, for vice-versa therapy sessions and long tissue culture conversations. To Adrian for loving trains, for eating the scraps, for the joy and fascination in and for any subject. To Pierre, for shared dog-love, for soooo much support in the last two years and for never, truly never, being annoyed when someone's time management and hood booking doesn't quite pan out.

To Milena, Alex, Birgit, Steffi, Jesse, Katja and Celine: For all your help! Tons of spheroids, instant last-minute orders, 50-sample RNA isolations, cDNA synthesis and countless western blots and ELISAs. We would all drown without you. To Natalie for administrative support and generating at least 500 Doodles and Zoom meetings.

To Steffi, Jesse and Natalie for your friendship and support, for all those botanic lunches and Döners (I do miss them!). I really appreciate you. And Steffi – you will be so dearly missed.

To Judith for laying the base of this project, but also for so much more! Your friendship and mentorship, your encouraging words (and motivational parcels), your true-to-yourself personality. I am so very happy we crossed paths in the CCU.

To Beata Halassy and four brave cancer patients. Without the courage of those suffering from the disease we investigate, there would be no advance.

Then, and finally: The biggest Thank You I owe to my family. My parents, for unconditional support, and providing a safe base – for everything. To Lou, my home-office shadow and thesis emotional support dog, and Ewa, the absolute GOAT-Maus. To Dennis, my husband. There is not enough space here and I know that you know. Together, we can do anything.

Thesis declaration

I hereby declare that I have written the submitted dissertation myself and in this process I have used no other sources or materials than those specifically indicated. Experiments and data that others contributed to are specifically declared. I hereby declare that I have not applied to be examined at any other institution, nor have I used the dissertation in this or any other form at any other institution as an examination paper, nor submitted it to any other faculty as a dissertation.

Heidelberg, October 22nd 2025

Katia Dittus